BOREAS An international journal of Quaternary research

Refining the timing of Middle Pleistocene (MIS 12 to MIS 6) ice advances into northern central Europe: sedimentological analysis and single-grain luminescence dating of glaciotectonic complexes and tunnel-valley fills

NIKLAS VON SOEST, NEDA RAHIMZADEH, DEBRA COLAROSSI, FALKO MALIS, TOBIAS LAUER, WERA SANDER-BEUERMANN, YVONNE SPYCHALA, CHRISTIAN BRANDES, RUNA FÄLBER, SUMIKO TSUKAMOTO AND JUTTA WINSEMANN

BOREAS

von Soest, N., Rahimzadeh, N., Colarossi, D., Malis, F., Lauer, T., Sander-Beuermann, W., Spychala, Y., Brandes, C., Fälber, R., Tsukamoto, S. & Winsemann, J.: Refining the timing of Middle Pleistocene (MIS 12 to MIS 6) ice advances into northern central Europe: sedimentological analysis and single-grain luminescence dating of glaciotectonic complexes and tunnel-valley fills. *Boreas*. https://doi.org/10.1111/bor.70049. ISSN 0300-9483.

The timing of the Middle Pleistocene ice advances into northern central Europe is still disputed. In this study, we summarize the current state of knowledge on the age of the Middle Pleistocene Saalian and Elsterian ice advances into northern central Europe and provide new single-grain luminescence ages of related meltwater deposits. Twenty-five samples for luminescence dating were taken from five different Saalian ice-marginal positions and (upthrusted) Elsterian tunnel-valley fills in northern Germany. The sampled Elsterian deposits mainly comprise subaqueous fan and delta sediments, which were deposited in glacial lakes that formed in underfilled tunnel valleys and their marginal areas. The estimated luminescence ages range between >578 and 346±98 ka, probably correlating with Marine Isotope Stage (MIS) 12, although an older and/or younger age (MIS >14 to MIS 8) cannot be excluded. During MIS 6, four different ice advances are recorded from the study area. During the maximum extent of the first and second Saalian Drenthe ice advances, large ice-dammed lakes formed along the Fennoscandian ice sheets, which catastrophically drained during ice-margin retreat. Further north, glaciofluvial fans and/or larger glaciofluvial distributive systems formed along the ice sheets. The first Saalian Drenthe ice advance probably occurred during MIS 6e-d. However, the estimated luminescence ages range between 293±59 and 209±37 ka, and therefore, we cannot rule out an earlier Saalian pre-Drenthe ice advance into the north-eastern part of the study area. After a phase of ice-sheet retreat, fluvial erosion and soil formation, the second Saalian Drenthe ice advance probably occurred during late MIS 6c. The estimated luminescence ages range between 172±38 and 123±18 ka. Meltwater deposits that are related to the third Saalian Drenthe (Hondsrug ice stream) and/or Warthe ice advances have luminescence ages of 128±19 to 123±22 ka, correlating with MIS 6b-a. The glaciotectonic complexes partly have a multiphase development related to the different Saalian ice advances. Smaller composite ridge systems with shallow detachments (20–60 m deep) evolved in areas with tunnel-valley fills, probably controlled by the rheological contrasts between sandy meltwater deposits and underlying fine-grained deposits of the uppermost Elsterian tunnel-valley fills (Lauenburg Clay Complex). In contrast, larger glaciotectonic complexes with deep detachments (>100 m deep) formed further south ('Rehburg line') where large tunnel valleys are absent.

Niklas von Soest, Wera Sander-Beuermann, Christian Brandes, Runa Fälber and Jutta Winsemann (corresponding author: winsemann@geowi.uni-hannover.de), Institute of Earth System Sciences, Leibniz University Hanover, Callinstrasse 30, 30167 Hanover, Germany; Neda Rahimzadeh and Sumiko Tsukamoto, LIAG Institute for Applied Geophysics, Stilleweg 2, 30655 Hanover, Germany; Debra Colarossi, Department of Geography and Earth Sciences, Aberystwyth University, Ceredigion SY23 3DB, UK; Falko Malis, State Authority of Mining, Energy and Geology (LBEG), Stilleweg 2, 30655 Hanover, Germany; Tobias Lauer, Department of Geosciences, Eberhard Karls University Tübingen, Schnarrenbergstrasse 94-96, 72076 Tübingen, Germany; Yvonne Spychala, Geological Institute, RWTH Aachen University, Wüllnerstrasse 2, 52062 Aachen, Germany; *received 18th August 2025, accepted 12th December 2025.*

The age and number of the Middle Pleistocene ice advances into northern central Europe are still in debate (Ehlers *et al*. 2011; Böse *et al*. 2012; Roskosch *et al*. 2015; Lang *et al*. 2018; Lauer & Weiss 2018; Batchelor *et al*. 2019; Marks *et al*. 2019; Winsemann *et al*. 2020; Kronborg *et al*. 2025). Among the various Quaternary geochronological methods, luminescence dating has been widely used to establish chronologies for past glaciations. However, its application to glacigenic meltwater deposits presents considerable challenges. One major issue is insufficient bleaching of the luminescence signal, caused by limited light exposure during sediment transport in high-energy glacial environments, where transport distances are typically short (e.g. Fuchs & Owen 2008; King *et al*. 2014; Winsemann *et al*. 2018; Lang *et al*. 2021b; Krauß *et al*. 2025) and high flow turbulence and/or a high content of suspended particles can reduce the optical transparency of the water column (Thrasher *et al*. 2009; Alexanderson & Murray 2012; Weckwerth *et al*. 2013; Kalińska *et al*. 2025). Therefore, providing a reliable chronology of glacigenic deposits, which distinguishes various substages of ice advances during the Saalian and Elsterian glaciations, remains challenging.

The study area is located in northern Germany (Fig. 1) and only very few numerical ages of Elsterian glacigenic deposits are available and correlate with Marine Isotope Stage (MIS) 12 (Roskosch *et al*. 2015). Luminescence

DOI 10.1111/bor.70049

ages of fluvial deposits, overlying the Elsterian till in eastern Germany, correlate with MIS 11 or early MIS 10 and support an MIS 12 age of the Elsterian ice advances (Lauer & Weiss 2018), although these data only provide a minimum age for the Elsterian glaciation. Saalian ice advances during MIS 10 and MIS 8 into the study area have been discussed in previous studies (Beets *et al*. 2005; Laban & van der Meer 2011; Kars *et al*. 2012; Lee *et al*. 2012; Roskosch *et al*. 2015; Lang *et al*. 2018). However, these ages may be less reliable because a decade ago it was still challenging to establish resilient luminescence chronologies for Middle Pleistocene glacigenic deposits. Furthermore, these age estimates are not supported by the age of fluvial terrace deposits above the Elsterian till beds in eastern Germany (Krbetschek *et al*. 2008; Lauer & Weiss 2018).

During MIS 6, several ice advances occurred into the study area, which are referred to as Drenthe and Warthe glaciations (Litt *et al*. 2007; Skupin & Zandstra 2010; Ehlers *et al*. 2011; Böse *et al*. 2012; Stephan 2014; Roskosch *et al*. 2015; Lang *et al*. 2018). However, the exact age of these ice advances is still unknown and correlation problems exist. While the first two ice advances of the Saalian Drenthe glaciation had a similar maximum extent and can be correlated over longer distances, it is not known if the third ice advance (referred to as Hondsrug ice stream in the westernmost part of the study area) can be correlated with a third Saalian Drenthe or the Warthe ice advance into the easternmost part of the study area (Rappol 1984; Kluiving *et al*. 1991; von Poblozki 1995, 2002; Eissmann 2002; Meyer 2005; Litt *et al*. 2007; Passchier *et al*. 2010; Skupin & Zandstra 2010; Ehlers *et al*. 2011; Lang *et al*. 2018). During all these Saalian ice advances, glaciotectonic complexes formed, which mark major ice-marginal positions during ice advance and/or retreat.

In this study, we summarize the current state of knowledge on the age of the Middle Pleistocene Elsterian and Saalian ice advances into northern central Europe and provide 25 new single-grain feldspar luminescence ages of Elsterian and Saalian glacigenic sediments to constrain the age of the ice advances and their tentative correlation with marine isotope stages/substages. Samples for luminescence dating were collected for the first time from Elsterian tunnel-valley fills and five different Saalian ice-marginal positions. We analyse the glacigenic depositional systems, discuss the age and evolution of the glaciotectonic complexes and the lithological role of tunnel-valley fills for the location of the basal detachments in which the thrust faults are rooted.

Regional setting and previous work

The first advance of the Fennoscandian ice sheet that reached far into northern and central Germany (Fig. 1) probably occurred during MIS 12 and is referred to as Elsterian glaciation (e.g. Ehlers *et al*. 2011; Roskosch *et al*. 2015; Lauer & Weiss 2018). The occurrence of pre-Elsterian tills in Denmark and the northernmost area of Germany may be related to an earlier ice advance during MIS 16 (Winsemann *et al*. 2020) or MIS 22–24 (e.g. Ehlers *et al*. 2011; Kronborg *et al*. 2025).

From the Elsterian glaciation, two major ice advances are recorded in the study area. These ice advances occurred from the north, followed by a subsequent advance from the north-east (Meyer 1987b; Eissmann 2002; Litt *et al*. 2007; Lutz *et al*. 2009; Stackebrandt 2009; Ehlers *et al*. 2011; Stephan 2014; Coughlan *et al*. 2018; Lang *et al*. 2018). The Elsterian ice advances had approximately the same extent (Fig. 1B) and the two till beds are separated by fluvial deposits, referred to as Miltitz interval, indicating a major ice sheet retreat (Fig. 2; cf. Eissmann 2002). In north-western Germany, the two till beds cannot be correlated over longer distances and are separated by meltwater deposits (Caspers *et al*. 1995; Böse *et al*. 2012). During the Elsterian ice advances, deep subglacial tunnel valleys were incised into the subsurface. These tunnel valleys trend approximately N–S and NE–SW, are commonly between 100 and 300 m deep (Fig. 3) but may locally reach depths of more than 500 m (Breuer *et al*. 2023). They are mainly filled with meltwater deposits. In many localities, glaciolacustrine deposits of the Lauenburg Clay Complex fill the uppermost part of the tunnel valleys. The Lauenburg Clay Complex is therefore commonly used as a stratigraphic marker, although the deposition was likely time-transgressive (Janszen *et al*. 2013). These thick accumulations of sand, silt and clay were most probably deposited during the retreat of the second Elsterian ice sheet (Fig. 2) in underfilled tunnel valleys and are partly overlain by Holsteinian deposits (e.g. Caspers *et al*. 1995; Janszen *et al*. 2013; Steinmetz *et al*. 2015; Coughlan *et al*. 2018).

In front of the ice sheets, ice-dammed lakes formed (Klostermann 1992; Junge 1998; Eissmann 2002; Ros-

Fig. 1. Location of the study area. The DEM is based on Copernicus data and information funded by the European Union (EU-DEM layers). A. Overview map, showing Saalian ice-marginal positions and related composite ridge systems (black lines) that formed during ice advance. A = Altenwalde composite ridge system; L = Lamstedt composite ridge system; RL = composite ridge system of the so-called Rehburg line; S = Salzwedel composite ridge system. Ice-marginal positions are based on Ehlers *et al*. (2011) and Winsemann *et al*. (2020). A–A′ location of cross-section, shown in Fig. 3. B. Overview map, showing the maximum extent of the Middle and Late Pleistocene ice sheets with tentative correlation with marine isotope substages. Ice margins are based on Ehlers *et al*. (2011) and Lang *et al*. (2018). The Saalian Drenthe (III) ice advance in the western part of the study area is referred to as Hondsrug ice stream. White circles indicate new sampling locations for luminescence dating (this study). White stars indicate the locations of numerical ages from previous studies. For further information, see Table S1.

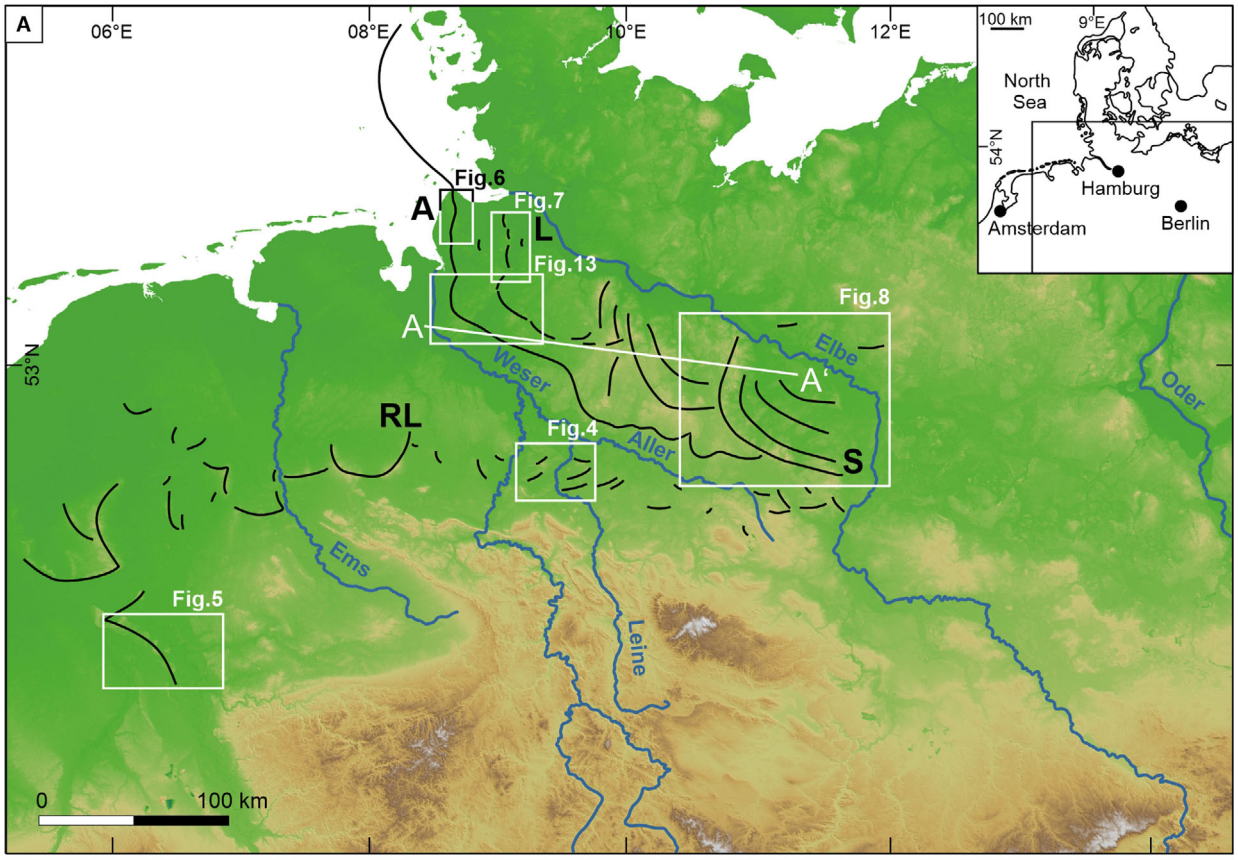

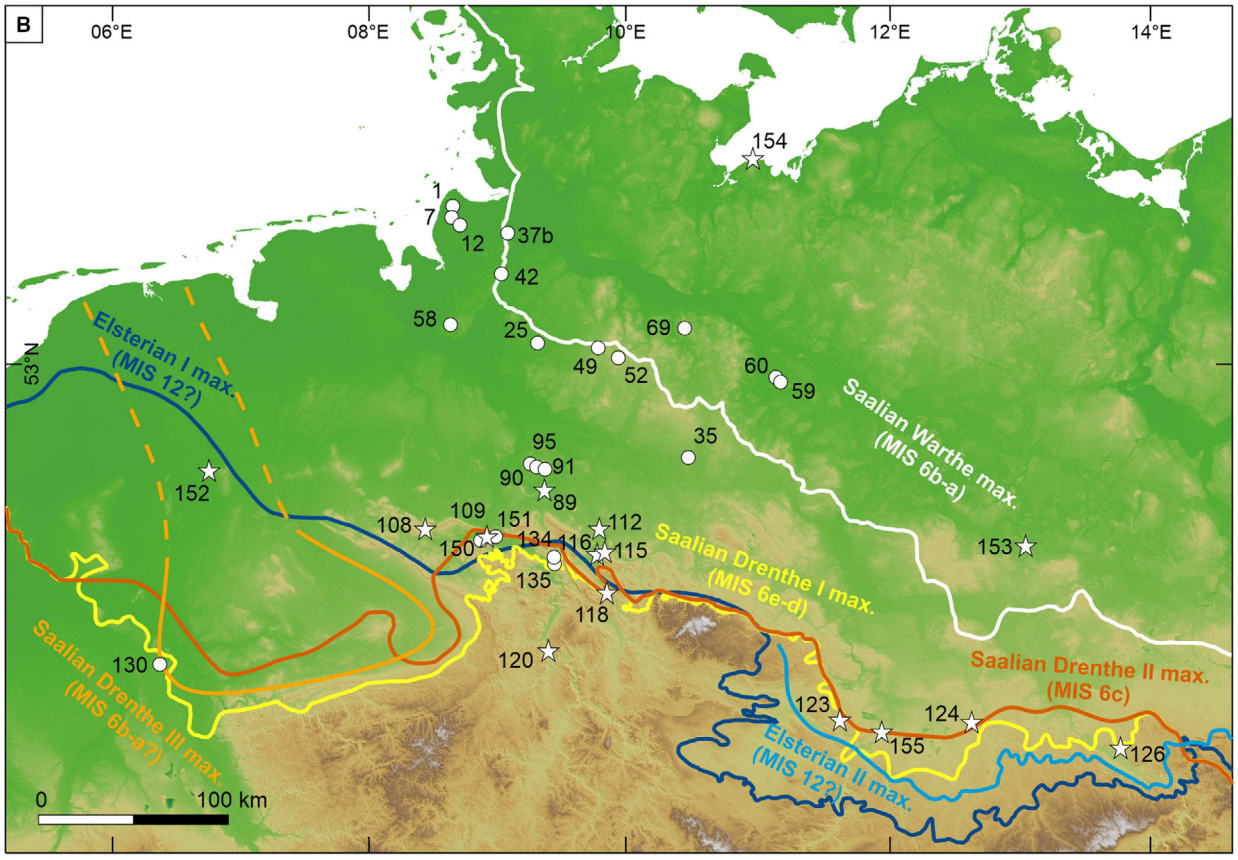

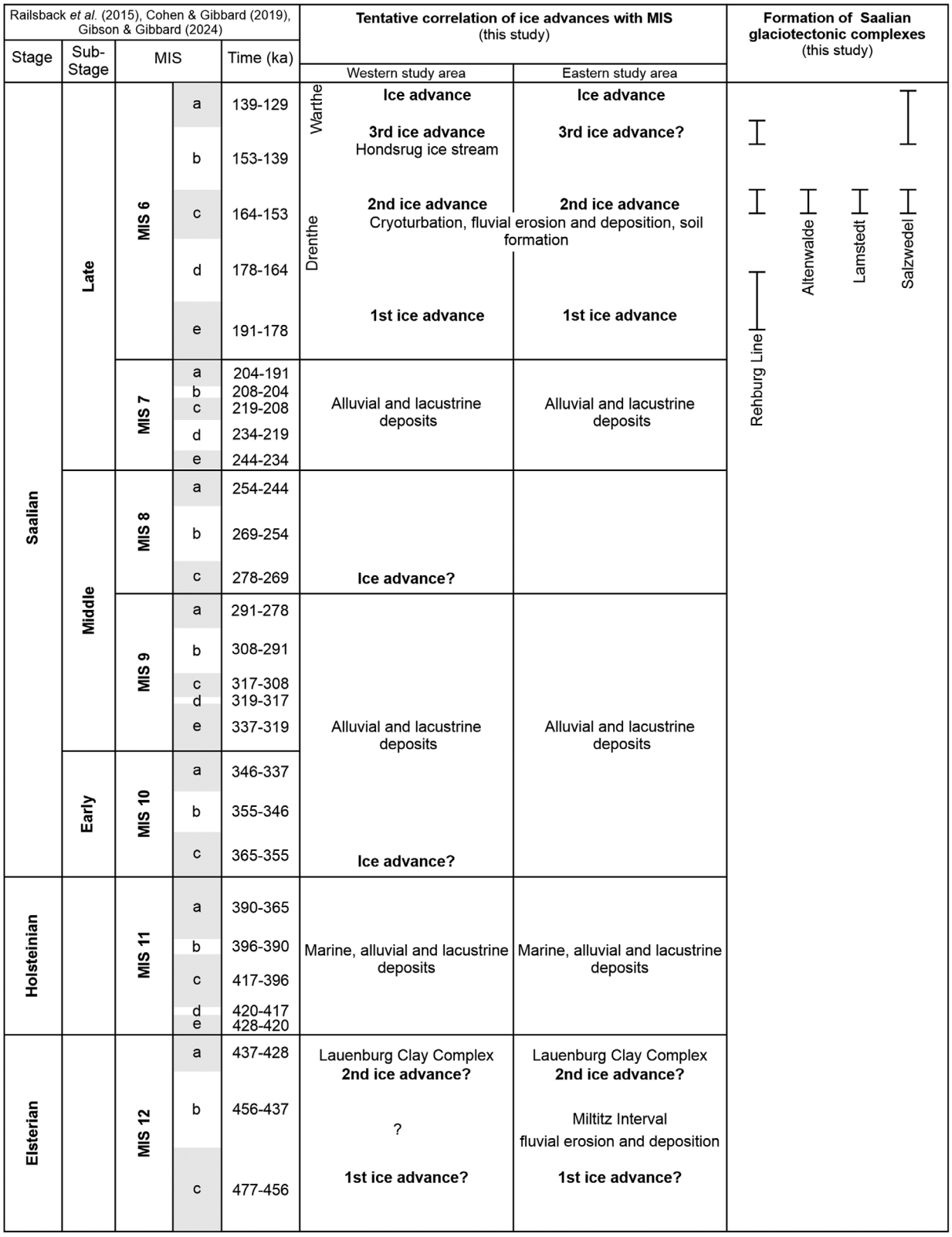

Fig. 2. Stratigraphic chart for the Middle Pleistocene in northern Germany summarizing lithostratigraphic units, the timing of ice advances and the formation of glaciotectonic complexes. Lithostratigraphic units are after Lüttig (1954, 1960), Eissmann (2002), Litt *et al.* (2007) and Lang *et al.* (2018).

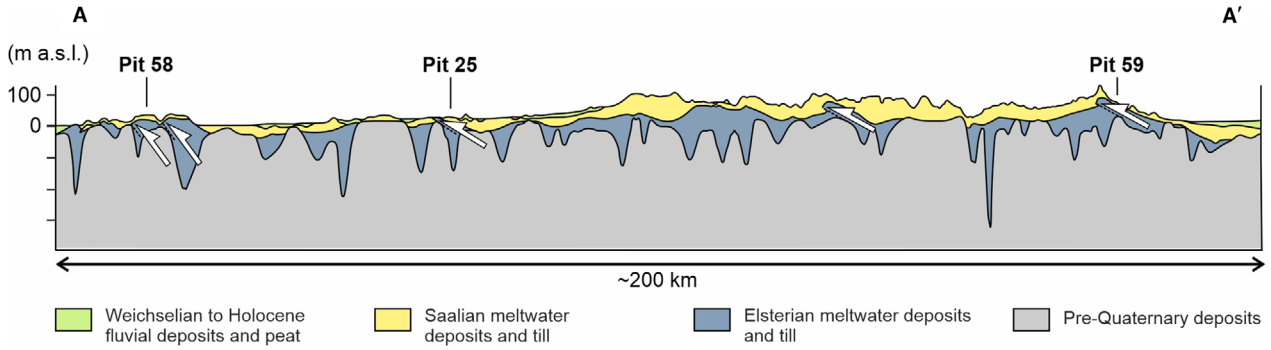

Fig. 3. Cross-section of the northern part of the study area showing the distribution and depth of Elsterian tunnel-valley fills in northern Germany and the location of measured logs. The cross-section was extracted from a 3D subsurface model conducted by Fälber *et al.* (2025), using the depth map of Kuster & Meyer (1995) and the 3D-subsurface model of LBEG (2013) for the base of the Quaternary succession. For location see Fig. 1A.

kosch *et al.* 2015). The best documentation of the Elsterian glaciation is recorded from eastern Germany.

Four Saalian ice-advances are commonly distinguished in the north-western part of the study area, which belong to the Drenthe and Warthe glaciations (Figs 1B, 2). These ice advances were defined on the base of clast composition of tills and reconstructed ice-flow directions (see Lang *et al.* 2018 for synopsis). During the Drenthe glaciation, three ice advances (in the following referred to as Saalian I, II and III) occurred into the north-western part of the study area, which approached from northerly, north-easterly and north-westerly to easterly directions (Rappol 1984; Meyer 1987a, b, 2005; Kluiving *et al.* 1991; Caspers *et al.* 1995; von Poblozki 1995, 2002; Eissmann 2002; Litt *et al.* 2007; Passchier *et al.* 2010; Skupin & Zandstra 2010; Ehlers *et al.* 2011; Böse *et al.* 2012; Lang *et al.* 2018; Winsemann *et al.* 2020).

The first and second Saalian Drenthe (I, II) ice advances nearly reached the same extent and are partly separated by fluvial deposits and a palaeosol, pointing to a major phase of ice-sheet retreat (Figs 1B, 2; cf. Lüttig 1960; Eissmann 2002; Lang *et al.* 2018). During maximum extents of these ice sheets, large ice-dammed lakes formed along the ice margins. Related ice-marginal deltas and subaqueous fans were comprehensively studied during the last two decades and the characteristics of the sedimentary facies and depositional architecture are summarized in Winsemann *et al.* (2003, 2004, 2009, 2011, 2018, 2021) and Lang *et al.* (2017, 2018, 2021b). Previous age estimates for these glaciolacustrine delta deposits range between 250±20 and 144±9 ka (Roskosch *et al.* 2015; Lang *et al.* 2018; Müller 2021; Winsemann *et al.* 2022). During ice-sheet retreat, these glacial lakes catastrophically drained (Meinsen *et al.* 2011; Winsemann *et al.* 2016; Lang *et al.* 2018, 2019; Winsemann & Lang 2020). Luminescence ages of glacial lake-outburst flood (GLOF) deposits range between 153±7 and 139±8 ka (Winsemann *et al.* 2016).

The third Saalian Drenthe (III) ice advance (Hondsrug ice stream) is best recorded from the westernmost part of the study area and the southern North Sea and characterized by a red till with a Fennoscandian provenance (Rappol 1984; Meyer 1987b, 2005; Kluiving *et al.* 1991; Passchier *et al.* 2010; Skupin & Zandstra 2010). The late Saalian Warthe ice advance (Fig. 1B) approached from an easterly to north-easterly direction and is also characterized by a red till with a Fennoscandian provenance (Caspers *et al.* 1995; von Poblozki 1995, 2002; Eissmann 2002; Meyer 2005; Ehlers *et al.* 2011). Luminescence ages of meltwater deposits range between 155±21 to 130±17 ka (Lüthgens *et al.* 2010; Kenzler *et al.* 2018).

The glaciotectonic complexes

During the Saalian glaciations, four major glaciotectonic complexes formed (Figs 1A, 2, 4–8), which represent so-called composite ridge systems (cf. Aber *et al.* 1989), characterized by subparallel ridges and valley systems, arcuate in plan view. They indicate major ice-marginal positions during ice advance and/or retreat and partly reveal a multi-phase deformation history (Sindowski 1965, 1969a; Höfle & Lade 1983; van der Wateren 1987; van Gijssel 1987; Klostermann 1992; Ites 1996; Skupin & Zandstra 2010).

The Rehburg Line composite ridge system. – The so-called Rehburg line forms part of a large, E–W trending composite ridge system north of the North German Uplands (Figs 1A, 4, 5), which stretches over 400 km from Germany to the Netherlands. This glaciotectonic complex initially formed during the first Saalian ice advance (van der Wateren 1987; Klostermann 1992; Skupin & Zandstra 2010; Ehlers *et al.* 2011; Laban & van der Meer 2011). The glaciotectonic ridges are up to 145 m high and partly bound deep glacial basins, >100 m deep, which were filled during ice-margin retreat and the Late Pleistocene (e.g. van den Berg & Beets 1987;

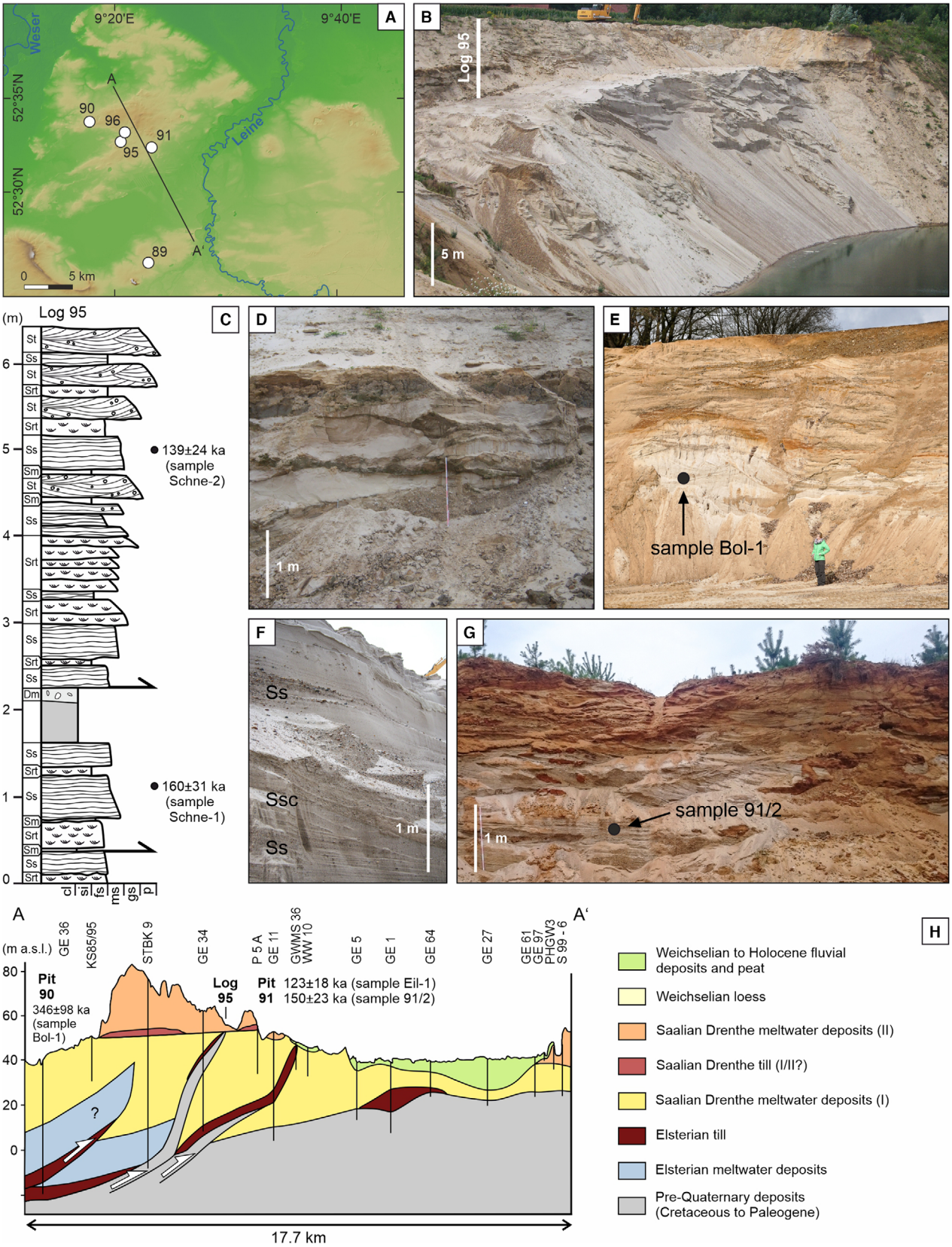

Fig. 4. Cross-section of the glaciotectonic complex of the Rehburg line near Steinhude, sampling location, sedimentary facies and luminescence ages. A. Digital elevation model, showing location of the cross-section and studied pits. B. Glaciotectonically deformed glaciolacustrine deposits of the first Saalian Drenthe (I) ice advance, unconformably overlain by undeformed glaciolacustrine deposits of the second Saalian Drenthe (II) ice advance (pit 95). C. Sediment log of pit 95 (Schneeren) with luminescence ages. The till on top of the thrust sheet (consisting of pre-Quaternary rocks) is interpreted to be Elsterian in age. For key, see Fig. 12 and Table 1. D. Close-up view of (B) showing deformed glaciolacustrine deposits. E. Upthrusted Elsterian glaciolacustrine delta and/or glaciofluvial deposits (pit 90 Bolsehle). F. Close-up view of (B) showing thick antidune deposits (Ss) and scour-fill deposits (Ssc) of the lower deformed glaciolacustrine succession (pit 95 Schneeren). G. Coarse-grained trough cross-stratified incised-valley fill deposits (pit 91, Eilvese). The incised valley probably formed during lake drainage after retreat of the second Saalian Drenthe (II) ice sheet. H. Cross-section of the glaciotectonic complex. The control by borehole data and numerical ages is limited and therefore the reconstructed cross-section is uncertain. For location, see Fig. 1A, B and Table S1.

Meyer 1987a, b; van der Wateren 1987; Hahne *et al.* 1994; Klimke *et al.* 2013). The glaciotectonic complex partly contains large thrust-sheets of Mesozoic, Cretaceous, Paleogene, Neogene and Lower Pleistocene sedimentary rocks/sediments (Klostermann 1986; Meyer 1987a, b; van der Wateren 1987, 1994; Hahne *et al.* 1994; Ites 1996). Incorporated Middle Pleistocene till beds, fluvial and meltwater sediments comprise pre-tectonic and syn-tectonic deposits that are Elsterian and Saalian in age. The main transport direction of thrust sheets was towards the south. Overprinting of the glaciotectonic complex occurred during the second Saalian Drenthe (II) ice advance (Lang 1964; Jordan 1979, 1980; Voss 1979, 1982, 1991; Klostermann 1990, 1992; Kluiving *et al.* 1991; van der Wateren 1994; Ites 1996; Skupin & Zandstra 2010). In the north-eastern Netherlands and the lower Rhine Embayment, the glaciotectonic complex of the Rehburg line has also been affected by the third Saalian Drenthe (III) ice advance, which is referred to as 'Hondsrug ice-stream' (Kluiving *et al.* 1991; Skupin & Zandstra 2010). The Hondsrug ice-stream approached from a northerly to north-westerly direction and partly steepened the older glaciotectonic ridges (Rappol 1984; van den Berg & Beets 1987; Passchier *et al.* 2010; Skupin & Zandstra 2010; Laban & van der Meer 2011; Lang *et al.* 2018). Post-glaciotectonic Saalian sediments consist of glaciofluvial and glaciolacustrine delta deposits, which onlap or overly the glaciotectonic complexes (Figs 4, 5; van der Wateren 1987, 1994; Lang & Winsemann 2013; Winsemann *et al.* 2016; Lang *et al.* 2021b; Müller 2021). Fading-corrected, pulsed IR_{50} feldspar ages of the southernmost glaciolacustrine delta deposits (pit 89, Figs 1B, 4A, Table S1) range between 158±4 ka and 189±5 ka (Müller 2021).

The Altenwalde and Lamstedt composite ridge systems. – The Altenwalde and Lamstedt composite ridges form parallel, N–S trending ridges that are approximately 30 km spaced apart (Figs 1A, 6, 7). Unlike the southernmost composite ridge system of the Rehburg line, the basal detachment is much shallower (20–60 m below surface). The age of these glaciotectonic complexes is still unknown and debated. The clast composition of till beds and the direction of ice push imply that both glaciotectonic complexes formed during the second Saalian Drenthe (II) ice advance (Richter 1956; Sindowski 1965, 1969a; Höfle & Lade 1983; van Gijssel 1987).

The Altenwalde glaciotectonic complex stretches from Cuxhaven in the north to Bremerhaven in the south (Fig. 6A). It consists of two major NNW–SSE trending ridges, 20–38 m high, and spaced apart approximately 2.5 km (Sindowski 1965, 1969a). The thrust sheets include Elsterian deposits of the Lauenburg Clay Complex, Saalian till and Saalian meltwater deposits. The location of the detachment surface is not exactly known but is likely located in the Elsterian fine-grained deposits of the Lauenburg Clay Complex at a depth of 20–60 m (Sindowski 1965, 1969a; Meyer & Schneekloth 1973). However, in the northernmost area, the detachment surface is most probably located at the base of the first Saalian till (Fig. 6F). Thrusting was towards the west. The till of the first Saalian Drenthe (I) ice advance commonly overlies Saalian meltwater sediments and partly fills the uppermost part of the Elsterian tunnel valleys and their marginal areas (Steinmetz *et al.* 2015). The younger second Saalian Drenthe (II) till was deposited on top and the ice-proximal side of the easternmost ridge (Sindowski 1969a, b) where it is partly overlain by meltwater sands deposited during ice retreat.

The Lamstedt composite ridge system is a N–S trending, curvilinear composite ridge system, which is up to 7 km wide (Fig. 7A). The two main ridges are 28–75 m high and spaced 1.5–4 km apart. They have an asymmetrical geometry, with a steeper ice-proximal side. The thrust sheets consist of Eocene marine clays, Elsterian till and clay, Holsteinian interglacial deposits, Saalian meltwater deposits and the first Saalian Drenthe (I) till (Fig. 7C; Höfle & Lade 1983; van Gijssel 1987). Ice push was towards the west and the tectonic structures and bedding planes gently dip (2°–8°) in north-easterly to south-easterly directions. The detachment surface is located in the Eocene marine clay and fine-grained Elsterian deposits of the Lauenburg Clay Complex (van Gijssel 1987). The deposits on the western, ice-distal slope of the Lamstedt composite ridge consist of two till beds separated by meltwater deposits (Fig. 7C), which were interpreted as the first and second Drenthe (I, II) till (Höfle & Lade 1983). The upper second Drenthe (II) till can be traced further westward for about 25 km until the Altenwalde composite ridge (Höfle & Lade 1983). As only the till of the first Saalian

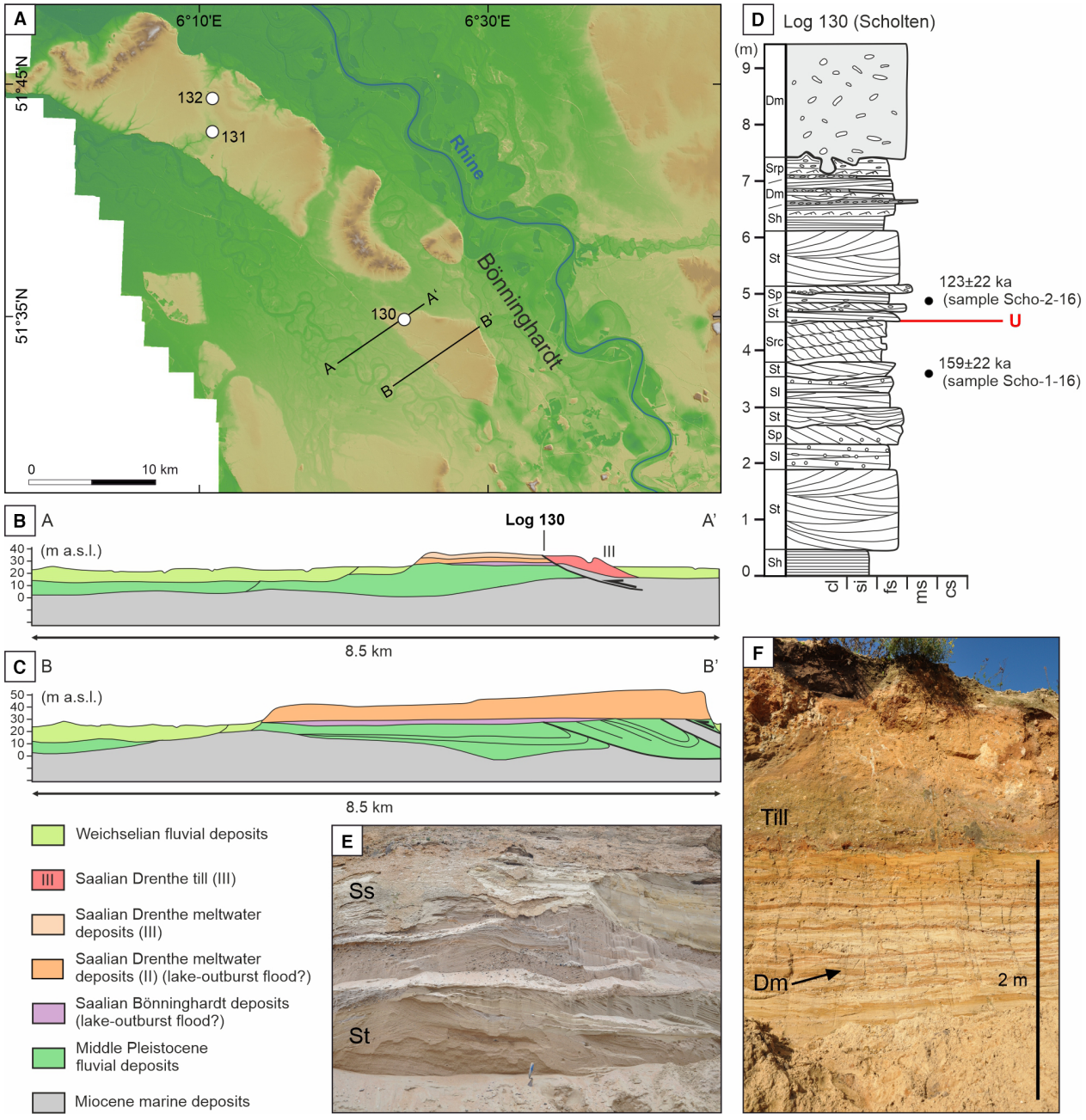

Fig. 5. Cross-sections of the glaciotectonic complex of the Rehburg line in the lower Rhine Embayment, sampling location, sedimentological log and luminescence ages. A. Digital elevation map of the study area, showing the location of pits and cross-sections. B and C. Cross-sections of the glaciotectonic complex (modified after Klostermann 1986 and Winsemann *et al.* 2016). D. Sediment log of pit 130 with luminescence ages (Scholten; Bönninghardt). The log was modified from Winsemann *et al.* (2016). For key, see Fig. 12 and Table 1. Red line indicates a major unconformity (U). E. Lower sedimentary succession exposed in pit 130 (Scholten; Bönninghardt), consisting of thick-bedded trough cross-stratified (St) and sinusoidally stratified (Ss) sand and pebbly sand. F. Uppermost sedimentary succession exposed in pit 130 (Scholten; Bönninghardt). Intercalation of thin- to medium-bedded ripple cross-laminated sand, trough cross-stratified pebbly sand and diamicton, overlain by the red subglacial till of the third Saalian Drenthe (III) ice advance (Hondsrug ice stream). The thin diamicton layers have a high proportion of clasts derived from Scandinavian and Baltic sources and may therefore indicate debris flows from the ablating ice front. For location, see Fig. 1A, B and Table S1.

Drenthe ice advance is incorporated in the thrust sheets, thrusting most likely occurred during the second Saalian Drenthe ice advance. The Lamstedt composite ridge system was subsequently overridden by the second Saalian ice sheet.

The Salzwedel composite ridge system. – The Salzwedel composite ridge system is located in the easternmost part of the study area (Figs 1A, 8) and probably has a multiphase development. It has an arcuate geometry and extends about 55 km from south-west to north-east

and 30–80 km from north-west to south-east (Fig. 8D, G). The individual glaciotectonic ridges are 25–160 m high, 2–9 km wide, spaced 7–13 km apart and their height decreases towards the north-east. Ridges and the intervening low areas form a subparallel arcuate pattern.

The thrust sheets consist of Elsterian meltwater deposits, the first Saalian Drenthe (I) till and Saalian meltwater deposits (Fig. 8G). Ice push was towards the south-west. Tectonic structures and bedding planes gently dip (5°–30°) in easterly directions. The detachment surface is located in fine-grained marine Neogene deposits and glaciolacustrine deposits of the Lauenburg Clay Complex (Fig. 8G). Unfortunately, the control by borehole data and numerical ages is very limited and therefore the reconstructed cross-section is uncertain.

The westernmost ridges of the Salzwedel glaciotectonic complex probably formed during the second Saalian Drenthe (II) ice advance, and the arcuate pattern of the outermost ridge probably marks the margin of the ice lobe advancing from an easterly to north-easterly direction (Fig. 8D). During the subsequent Warthe ice advance, renewed thrusting of sediments occurred further east. These glaciotectonic ridges are lower in height and covered by the late Saalian Warthe till, which is partly superimposed directly on the second Saalian Drenthe (II) till (Merkt 1975; von Poblozki 1981, 1995, 2002). Meltwater deposits of the Warthe ice advance are commonly sparse (Merkt 1975; von Poblozki 1981).

In the intervening low areas between the glaciotectonic ridges, elongated glacial lakes formed, which are mainly filled with fine-grained sediments, 3.5–15 m thick (von Poblozki 1981, 2002; Burchardt 1993; Meyer 2009; Hein *et al*. 2021; Rahimzadeh *et al*. 2024). Late Saalian glaciolacustrine sediments partly gradually pass into Eemian and Weichselian lacustrine and fluvial sediments (von Poblozki 1973, 1981, 1995; Meyer 2009; Hein *et al*. 2021; Rahimzadeh *et al*. 2024), filling the accommodation space of the former glacial (lake) basins (Fig. 8G). Previous age estimates based on fading corrected multiple-grain pulsed IR_{50} and pulsed $pIRIR_{225}$ feldspar ages for the uppermost glaciolacustrine sediments near Lichtenberg (Fig. 8F) range between 155±14 and 123±12 ka and between 313±32 and 174±35 ka for the underlying older (glacio)lacustrine sediments (Rahimzadeh *et al*. 2024). The application of a Bacon age depth model to these luminescence ages produced slightly younger posterior ages of ~275–127 ka.

Material and methods

Fieldwork and data analysis

Outcrop and borehole data were studied to reconstruct the sedimentary facies and depositional architecture of the glacigenic depositional systems and glaciotectonic complexes. Sedimentary logs were measured at the scale of individual beds, noting grain size, bed thickness, bed contacts, bed geometry, internal sedimentary structures and palaeocurrent directions. The grain size was determined in the field using a grain-size comparison chart, finger probing and a hand lens. Palaeocurrent directions were obtained from planar cross-stratification and planar ripple cross-lamination. Based on the measured sections, 10 sedimentary facies types were defined and interpreted (Table 1). The coding of the sedimentary facies is after Miall (1985), Krüger & Kjær (1999) and Lang *et al*. (2021a, b). Photomosaics of larger outcrops were used for the interpretation of architectural elements (e.g. Miall 1985; Winsemann *et al*. 2018; Lang *et al*. 2021b). For the description of channel geometries and channel stacking patterns, the nomenclature of Gibling (2006) was applied.

The cross-section, showing the distribution and depth of Elsterian tunnel valleys in the study area (Fig. 3), was extracted from an unpublished 3D subsurface model conducted by Fälber *et al*. (2025). This model used the depth map of Kuster & Meyer (1995) and the 3D-subsurface model of LBEG (2013; Niedersächsisches Landesamt für Bergbau, Energie und Geologie) for the base of the Quaternary succession. To illustrate the lithostratigraphy and structure of sampled glaciotectonic complexes (Figs 4–8), cross-sections were constructed using digital elevation models, outcrop data (geometry and orientation of structural elements and bedding), published geological and lithofacies maps (Table S1) and 84 borehole logs. The archived borehole logs were obtained from the database that is maintained by LBEG. Lithofacies maps were provided by Landesamt für Geologie und Bergwesen Sachsen-Anhalt (LAGB).

High-resolution digital elevation models (1 m grid, vertical resolution: ±0.15 cm and 5 m grid, vertical resolution: ±0.15 cm) were produced using data from the Landesamt für Geoinformation und Landesvermessung Niedersachsen (LGLN) and analysed in a geographical information system (QGIS, Version 3.34) to map palaeo-ice-marginal positions and to image the glaciotectonic complexes.

To gain insight into the timing of Elsterian to Saalian ice advances into north-western Germany, 25 new samples were collected for luminescence dating during two field campaigns (2016/2017 and 2023/2024). The samples were collected from sand and gravel pits located along former ice marginal positions (Fig. 1B, Tables 2, S1).

Luminescence dating

Sampling and sample preparation. – Twenty-five samples were taken using light-tight steel tubes, which were hammered into the freshly cleaned outcrop sections. Material for dose rate measurement was collected from the same positions as the luminescence samples and the nearby surroundings. Where possible, >30 cm thick

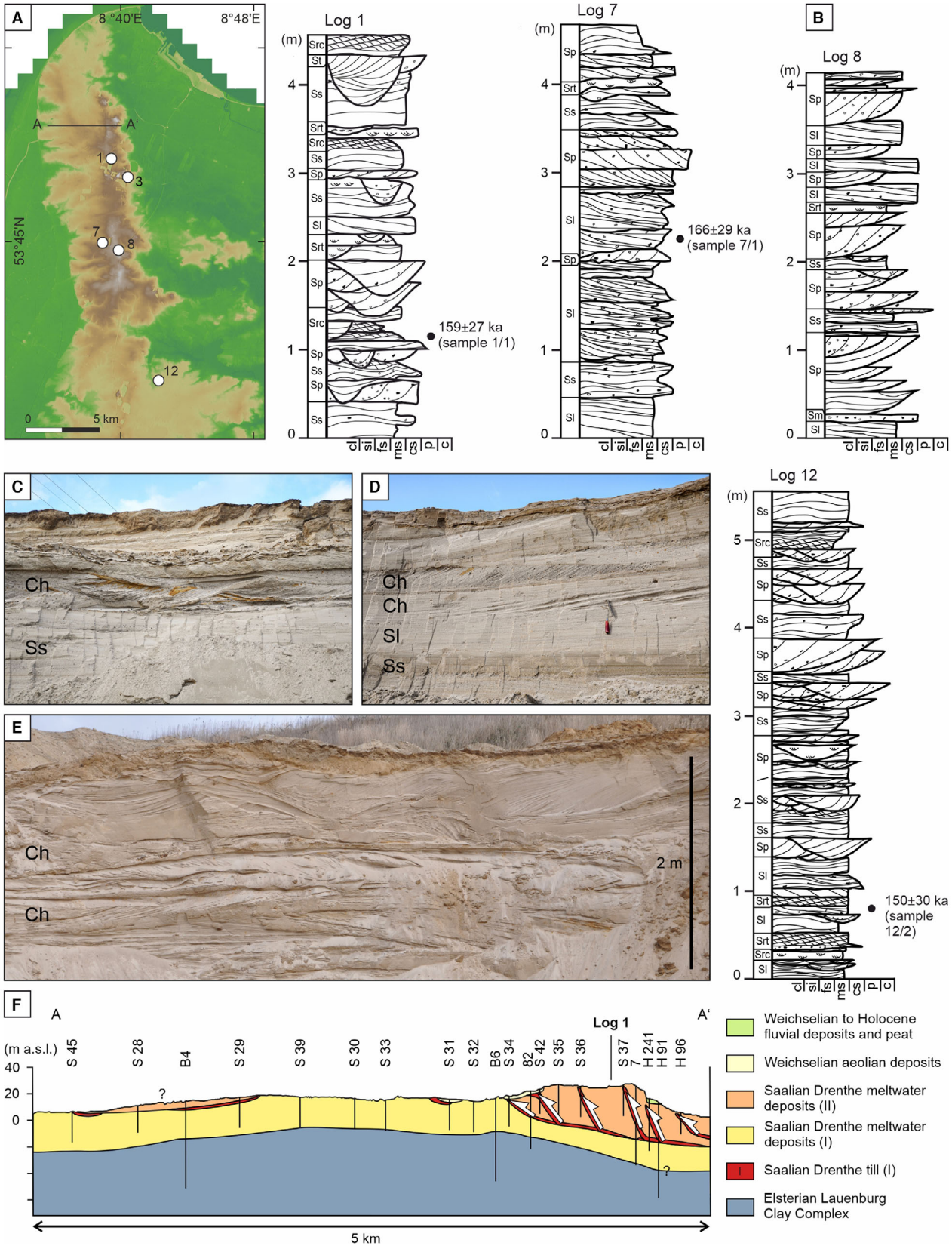

Fig. 6. Cross-section of the Altenwalde composite ridge system, sampling location and sedimentological logs. A. Digital elevation map of the study area, showing the location of pits and cross-sections. B. Sediment logs with luminescence ages. These sediments most probably represent meltwater deposits of the second Saalian Drenthe (II) ice advance. For key, see Fig. 12 and Table 1. C. Trough cross-stratified channel-fill deposits (Ch), overlying sinusoidally stratified sheetflood deposits (Ss). D. Glaciofluvial deposits of the upper succession exposed in pit 1. These deposits consist of low-angle cross-stratified (Sl) to sinusoidally stratified (Ss) sheetflood deposits, alternating with coarser-grained shallow multilateral channel fills (Ch). The trowel for scale is 30 cm. E. Glaciofluvial deposits of the uppermost succession exposed in pit 1, showing an increase in channel (Ch) depth and related bar size. F. Cross-section of the Altenwalde composite ridge system (modified after Sindowski 1969a and Grinat *et al.* 2021). For location, see Fig. 1A, B and Table S1.

sand beds were chosen for sampling to avoid potential effects of gamma-dose rate heterogeneity.

Sample preparation for luminescence dating was conducted under subdued red light in the OSL laboratory at the Max Planck Institute for Evolutionary Anthropology (MPI EVA) in Leipzig and at the LIAG Institute for Applied Geophysics in Hanover, Germany.

The material was treated with hydrochloric acid (HCl), sodium oxalate ($Na_2C_2O_4$) and hydrogen peroxide (H_2O_2) to remove carbonates, aggregates and organic matter, respectively. The material was then sieved to obtain the preferred grain-size fraction; 180–250 µm for samples analysed at MPI EVA and 125–180 µm for those processed at LIAG, except for four samples (Bol-1, Schne-1, Schne-2 and Eil-1; LUM 3699–3702), where the 150–200 µm fraction was isolated, and sample 91/2 (LUM 5034), for which the 125-200 µm fraction was used (Table 2). Potassium (K)-rich feldspar was separated using sodium polytungstate at a density of 2.58 g cm^{-3}. Subsequently, the K-feldspar grains were loaded onto stainless steel discs (1 mm diameter) using silicone spray for multi-grain measurements (Data S1, Table S2), and onto aluminium discs drilled with 100 holes (each 300 µm in depth and diameter) for single-grain measurements.

Dosimetry. – The activities of ^{238}U, ^{232}Th and ^{40}K, as well as of their daughter nuclides were measured in the Felsenkeller Laboratory in Dresden and LIAG in Hanover, using high-resolution gamma-spectrometry. The dose rate conversion factors from Liritzis *et al.* (2013) were used for dose rate calculation. The cosmic dose rate contribution was estimated by accounting for sediment thickness and altitude/latitude (Prescott & Hutton 1994). To consider dose rate attenuation by moisture, a water content of 20±10% was used and to address the alpha efficiency, an *a*-value of 0.09±0.02 was taken (Schmidt *et al.* 2018). The internal potassium content was estimated to be 12.5±0.5% (Huntley & Baril 1997). Details of dose rates are given in Tables 2 and S3.

Equipment and measurement protocols. – The samples were measured at the MPI EVA in 2017 and at LIAG in 2023/2024. Initial tests were conducted using small (1 mm) aliquots. The equivalent dose (D_e) distributions showed a pronounced skewness indicative of an incompletely bleached feldspar luminescence signal for some samples. To better overcome this issue, all further measurements were conducted on individual grains of K-feldspar. Details regarding the multi-grain measurements and results can be found in Tables S2 and S3. D_e measurements were made on individual grains of K-feldspar using two automated Risø TL/OSL readers (DA-20 at MPI EVA and DA-15 at LIAG). Optical stimulation of individual grains was undertaken with a focused 150 mW IR laser (830 nm) fitted with a RG780 longpass filter, while simultaneous IR stimulation of all grains was undertaken by the IR LED array (870 nm). Luminescence emitted in the blue region was detected by an EMI 9235QB PMT filtered by a 3 mm LOT-Oriel D410 glass filter at MPI EVA and a combination of Schott BG-39/Corning 7–59 filters at LIAG. Laboratory irradiations were made using a $^{90}Sr/^{90}Y$ beta source, with dose rates of 0.122 Gy s^{-1} at MPI EVA and 0.111 Gy s^{-1} at LIAG. To obtain a non-fading signal, a two-step post-infrared IRSL (pIRIR) protocol with a second high-temperature IR stimulation (i.e. 290 °C and/or 275 °C) was applied (Table 3). All D_e measurements carried out at MPI EVA were made using the $pIR_{50}IR_{290}$ protocol based on Thiel *et al.* (2011) (Table 3A). Measurements carried out at LIAG used the $pIR_{200}IR_{275}$ protocol described by Jacobs *et al.* (2019) (Table 3B), in which a high stimulation temperature (200 °C) for the first IR stimulation was used to deplete high-fading signal components.

Representative single-grain pIRIR decay curves from samples HBT-1-16 and Wo/1 (L-EVA 1549 and LUM 5031) are shown in Fig. 9. The pIRIR signals decayed to background levels within 0.5 s of stimulation time. For the D_e determination, the initial signal was derived from the first 0.1 s stimulation, and the last 0.2 s of the decay curves were subtracted as background. Dose–response curves (DRC) were fitted using a single saturating exponential function (Fig. 9).

A dose recovery test, whereby the signal is bleached from a sample and a known beta dose is given and then measured as though it were an unknown natural dose, was used to confirm the suitability of the pIRIR protocols used in this study. Dose recovery tests were conducted on samples 1/1, 91/2 and 69/1 (LUM 4911, 5034 and 5035) for the $pIR_{200}IR_{275}$ and on samples Mü-1-16, St-1-16 and Scho-1-16 (L-EVA 1544, 1548, and 1579) for the $pIR_{50}IR_{290}$ protocol. Several single-grain discs were bleached in the solar simulator (2 and 4 h for $pIR_{50}IR_{290}$ and $pIR_{200}IR_{275}$, respectively);

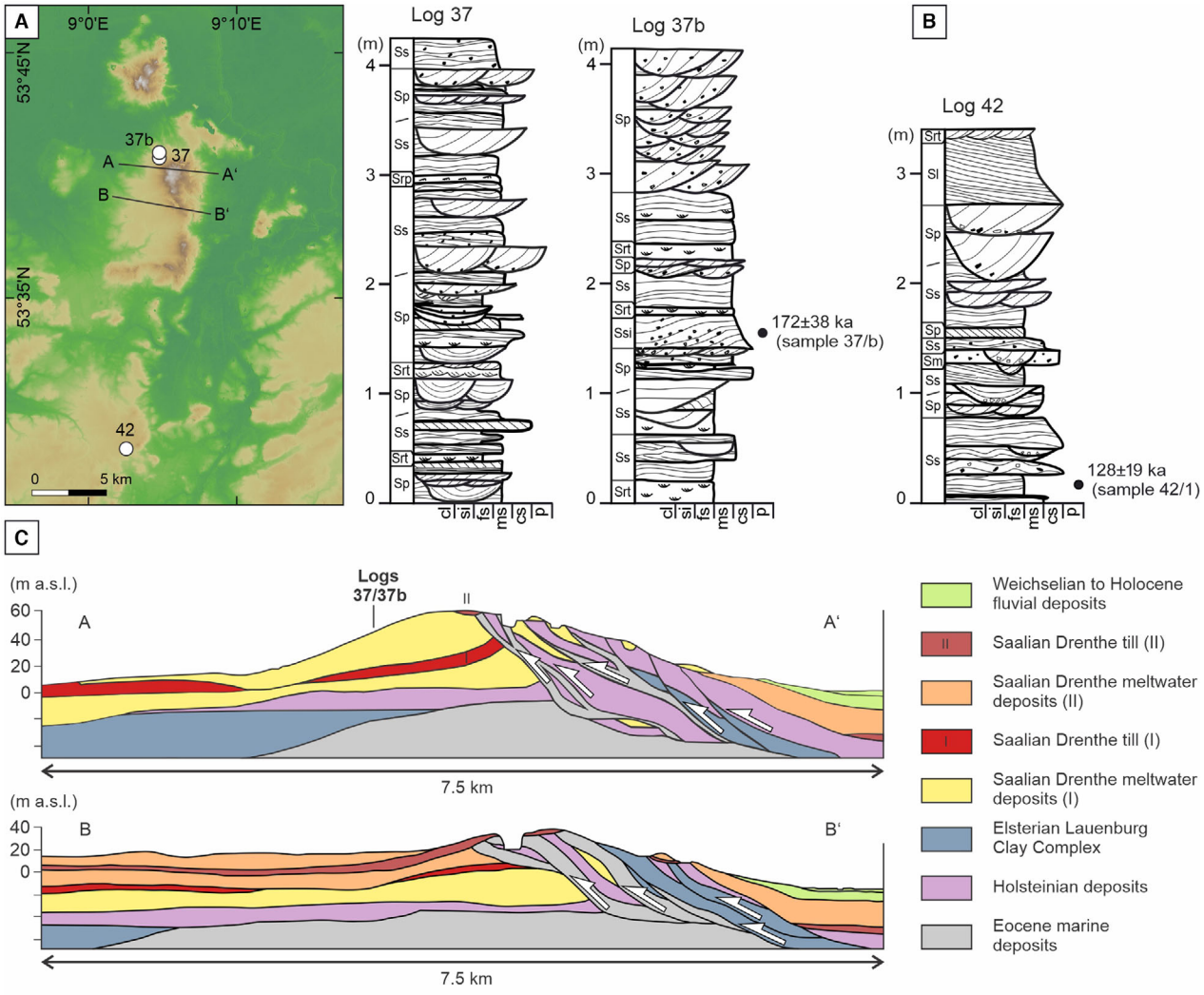

Fig. 7. Cross-section of the Lamstedt glaciotectonic complex, sampling location and sedimentological logs. A. Digital elevation map of the study area, showing the location of pits and cross-section. B. Sediment logs with luminescence ages. The glaciofluvial sediments of log 37 and 37 b most probably represent deposits of the retreating first Saalian Drenthe (I) ice sheet, whereas the glaciofluvial sediments of log 42 were deposited during the retreat of the second Saalian Drenthe (II) ice sheet or are related to the Warthe ice sheet. For key, see Fig. 12 and Table 1. C. Cross-sections of the glaciotectonic complex (modified after van Gijssel 1987). D. Sheetflood-dominated glaciofluvial fan deposits, exposed in pit 37b. E. Close-up view of (D) showing climbing-ripple cross-laminated sand (Src) at the base of the succession, overlain by sinusoidally stratified sand (Ss) and channelized, planar cross-stratified pebbly sand (Sp). The trowel for scale is 28 cm. F. Close-up view of (D) showing clastic dykes (arrows). The trowel for scale is 30 cm. G. Fine-grained multistorey channel fill (Ch), overlain by sheetflood deposits and multilateral channel fills. The planar cross-stratified pebbly sand that passes upwards into low-angle cross-stratified and sinusoidally stratified sand (Ssi) may either represent a larger bar or a humpback dune deposit (pit 37 b). The trowel for scale is 30 cm. For location, see Fig. 1A, B and Table S1.

between 1 and 5 single-grain discs were given a beta dose close to the natural dose and the remaining discs (between 3 and 8) were measured directly after bleaching to quantify the unbleachable component of the signal. The dose recovery ratio was calculated by dividing the recovered dose (after residual dose subtraction) by the given dose. The anomalous fading test for both signals was carried out using 1 mm multi-grain aliquots following the procedure by Auclair *et al.* (2003). Two samples (Mü-1-16, St-1-16; L-EVA 1544, 1548) were analysed for the $pIR_{50}IR_{290}$ protocol, while three samples (1/1, 91/2, 69/1; LUM 4911, 5034, 5035) were tested for the $pIR_{200}IR_{275}$ protocol.

Equivalent dose and age determinations. – Between three and six single-grain discs were measured for each sample. To select K-feldspar grains suitable for reliable D_e determination, the following rejection criteria were applied: (i) the initial T_n signal was less than 3σ of the corresponding background signal, or the relative error of T_n is >10%; (ii) the recycling ratio was not within the range of 0.9–1.1; (iii) the recuperation ratio was >5%; (iv) the figure of merit (FOM) was >10%; (v) the reduced chi-square (RCS) value for the DRC was >5; (vi) the L_n/T_n value reached or exceeded the saturation level of the corresponding DRC; and (vii) the D_e uncertainty could not be estimated. The numbers of grains measured, rejected and accepted are summarized in Table S4 for each of the samples, together with the reasons for rejection. The rejection process described above was carried out using the 'numOSL' R package (Peng & Li 2017).

Some single-grain data sets showed a high proportion of saturated grains (up to 66%; Table 4), defined as the number of grains rejected by rejection criteria vi and vii (Table S4) divided by the number of grains that passed criteria i–v. Excluding this large number of saturated grains results in a truncated D_e distribution and an underestimation of the final D_e determination (e.g. Duller 2012; Li *et al.* 2017; Jacobs *et al.* 2019). We therefore applied the L_nT_n method (Li *et al.* 2017, 2020), which is ideally suited for dating old samples where D_e values are beyond the linear part of the dose response curves. In contrast to the standard method, this approach does not reject saturated grains. Therefore, a full and untruncated distribution can be obtained.

All single-grain data were re-analysed using rejection criteria i to vi, therefore no grains were rejected because of saturation. The L_nT_n method is based on the establishment of a standardized growth curve (SGC) and the analysis of re-normalized L_n/T_n values for individual grains (Li *et al.* 2020). Note that in this study, the SGC was established only for applying the L_nT_n method, not for reducing the machine time. The SGC for each sample was built using the least square (LS) normalization procedure (Li *et al.* 2016), which involves iterative rescaling L_x/T_x ratios of all grains until there is negligible change in the rescaled L_x/T_x and all accepted grains converge onto a single dose–response curve (i.e. SGC), which is fitted using a single saturating exponential function. All L_x/T_x ratios, before and after LS-normalization, for two representative samples are shown in Fig. S1. The L_n/T_n ratios of individual grains were then re-normalized by multiplying L_n/T_n by their corresponding grain-specific scaling factors (so-called LS-normalized L_n/T_n). The LS-normalized L_n/T_n overdispersion values range from 45% (Schne-1; LUM 3700) to 18% (Th/1; LUM 5032) (Table 4). Fig. 10 shows example distributions of the LS-normalized L_n/T_n ratios in radial plots. For D_e determination, the re-normalized L_n/T_n ratios were then analysed using the 3-parameter minimum age model (MAM; Galbraith *et al.* 1999). The final MAM L_n/T_n value was then interpolated onto the SGC to obtain the final MAM D_e. All data analysis, including SGC construction, curve fitting and D_e and error estimation were achieved using the R package 'numOSL' (Peng & Li 2017). To apply the MAM to the poorly bleached sample, it is necessary to first determine the sigma-b (σ_b) parameter, which represents the scatter of a well-bleached grain population. Details on the σ_b determination are provided in Rahimzadeh *et al.* (2026), where six samples from this study (1/1, 7/1, 35/3, 37b/1, 69/1, 91/2, 69/1) were used. An average σ_b value of 0.22, derived from that study, was adopted here for the MAM analysis.

Results

Luminescence dating

Both pIRIR signals show an acceptable dose recovery ratio of 0.9–1.1, considering uncertainty. The residual-subtracted dose recovery ratios ranged from 1.05±0.03 (Ed-1-16; L-EVA 1545) to 1.12±0.02 (St-1-16; L-EVA 1548) for $pIR_{50}IR_{290}$ and from 0.91±0.04 (91/2; LUM 5034) to 0.93±0.08 (69/1; LUM 5035) for $pIR_{200}IR_{275}$

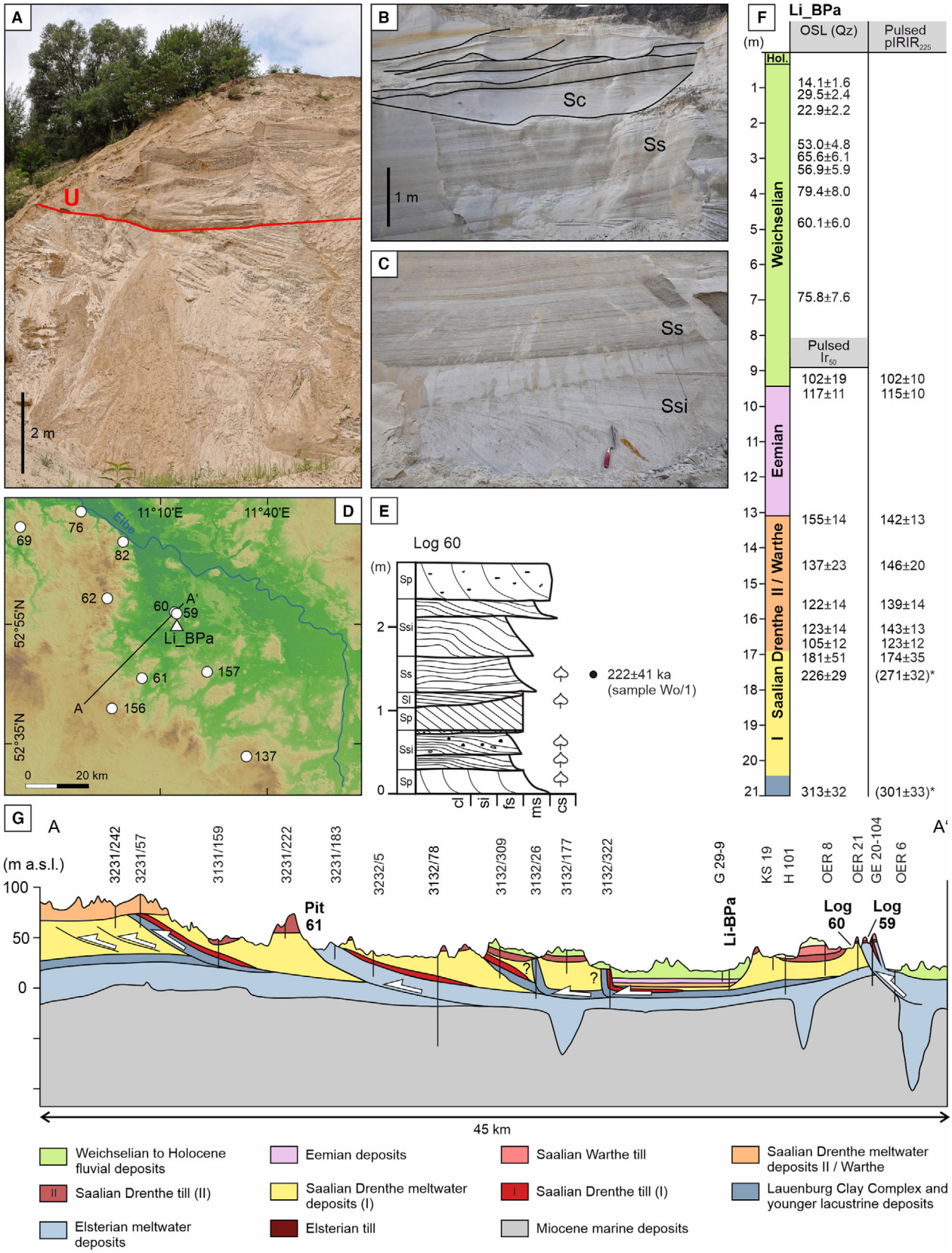

Fig. 8. Cross-section of the Salzwedel composite ridge system, sampling location, sedimentological logs and luminescence ages. A. Upthrusted glaciolacustrine deposits, unconformably overlain by delta deposits of the second Saalian Drenthe (II) ice advance (pit 62 Kröte). Red line indicates the unconformity U. B. Elsterian (?) subaqueous fan deposits exposed in pit 82 (Meudelfitz). Thick antidune deposits (Ss) are overlain by laterally and vertically stacked scour fills (Sc). C. Elsterian? subaqueous fan deposits exposed in pit 82 (Meudelfitz). Thick humpback-dune deposits (Ssi) at the base are overlain by antidune deposits (Ss). The trowel for scale is 30 cm. D. Digital elevation map of the study area showing the location of pits and cross-section. E. Sediment log of pit 60 with luminescence age. For key, see Fig. 12 and Table 1. F. Borehole log Li-BPa (Lichtenberg) with luminescence ages. The age estimates in brackets, indicated by asterisk* are less reliable because samples were in saturation (modified from Hein *et al*. 2021 and Rahimzadeh *et al*. 2024). G. Cross-section of the Salzwedel composite ridge system with location of pits, sediment logs and borehole Li-BPa. The control by borehole data and numerical ages is very limited and therefore the reconstructed cross-section is uncertain. The base of the Quaternary succession was extracted from a 3D subsurface model conducted by Fälber *et al*. (2025), using the depth map of Kuster & Meyer (1995) and the 3D-subsurface model of LBEG (2013). For location see Fig. 1A, B and Table S1.

(Rahimzadeh *et al*. 2026). The obtained fading rates (g_{2days}) ranged from 1.77±0.82%/decade (Mü-1-16; L-EVA 1544) to 2.0±0.6%/decade (St-1-16; L-EVA 1548) for $pIR_{50}IR_{290}$ and from 0.56±0.69%/decade (69/1; LUM 5035) to 1.16±0.72%/decade (91/2; LUM 5034) for $pIR_{200}IR_{275}$ (Rahimzadeh *et al*. 2026).

Table 1. Description and interpretation of sedimentary facies.

Facies	Description	Interpretation
Dm	Matrix-supported, poorly sorted, structureless diamicton. The matrix consists of clay, silt and fine-grained to coarse-grained sand. Pebble- to cobble-sized clasts have a high proportion (up to 25%) of material derived from Scandinavia and/or the Baltic area. Bed contacts are sharp, erosive or plan.	Thick, compacted beds with internal deformation structures are interpreted as subglacial tractional till. Thin beds represent cohesive debris flows of re-sedimented till or flow till from the ablating ice-front (Benn & Evans 2010).
Sm	Pebbly fine- to coarse-grained structureless or normally graded sand. Clasts are commonly pebble-sized. Bed contacts are sharp or erosive.	Suspension fallout from density flows in glaciolacustrine settings (Lang *et al*. 2017; Winsemann *et al*. 2018).
Ssc	Lenticular scours with structureless, diffusely stratified, lateral or concentric infills of sand and pebbly sand. Bed contacts are erosive.	Small, isolated scour fills formed by antidune-wave breaking (Cartigny *et al*. 2014; Winsemann *et al*. 2022). Laterally and vertically stacked larger scour fills or amalgamated scour fills indicate rapid cut-and-fill processes by supercritical density flows (Gorrell & Shaw 1991; Hofstra *et al*. 2015).
Sl	Tabular beds of low-angle cross-stratified to subhorizontally stratified sand and pebbly sand. Internal low-angle truncations are common. Bed contacts are sharp or erosive.	Deposits of breaking and upflow-migrating antidunes. Deposition by supercritical sheetfloods or density flows (Fielding 2006; Cartigny *et al*. 2014; Lang *et al*. 2021b) or deposits of shallow glaciofluvial bars (Miall 1985; Pisarska-Jamroży & Zieliński 2014).
Ss	Tabular beds of sinusoidally stratified sand and pebbly sand. Laterally, the thickness pinches and swells due to converging and diverging stratification. Bed contacts are sharp or erosive.	Deposits of stable, aggrading antidunes. Deposition by supercritical sheetfloods or quasi-steady density flows (Cartigny *et al*. 2014; Lang *et al*. 2017; Winsemann *et al*. 2018, 2022).
Ssi	Tabular beds of sigmoidally stratified sand and pebbly sand, displaying differentiation into topset, foreset and bottomset laminae. Bed contacts are sharp or erosive.	Deposits of migrating humpback dunes or transverse bars. Deposition by transcritical flows in glaciofluvial channels (Pisarska-Jamroży & Zieliński 2014) or density flows in glaciolacustrine settings. Metre-thick sigmoidally stratified sand beds may represent hydraulic jump bars (MacDonald *et al*. 2009; Winsemann *et al*. 2011; Lang *et al*. 2021b).
St	Trough cross-stratified fine- to coarse-grained sand and pebbly sand. Bed contacts are sharp or erosive.	Deposits of migrating 3D dunes or transverse bars. Deposition by subcritical flows in glaciofluvial channels (Miall 1985) or density flows in glaciolacustrine settings (Lang *et al*. 2017; Winsemann *et al*. 2018).
Sp	Planar cross-stratified fine- to coarse-grained sand and pebbly sand. Bed contacts are sharp or erosive.	Deposits of migrating 2D-dunes or transverse bars. Deposition by subcritical flows in glaciofluvial channels (Miall 1985; Pisarska-Jamroży & Zieliński 2014) or density flows in glaciolacustrine settings (Lang *et al*. 2017; Winsemann *et al*. 2018).
Srt	Ripple-trough cross-laminated fine- to coarse-grained sand. Bed contacts are sharp or erosive.	Deposits of migrating 3D ripples. Deposition by subcritical sheetfloods or flows in glaciofluvial channels (Miall 1985) or subcritical low-density turbidity currents in glaciolacustrine settings (Winsemann *et al*. 2018).
Srp	Planar-ripple cross-laminated fine- to coarse-grained sand. Bed contacts are sharp or erosive.	Deposits of migrating 2D ripples. Deposition by subcritical sheetfloods or flows in glaciofluvial channels (Miall 1985) or subcritical low-density turbidity currents in glaciolacustrine settings (Winsemann *et al*. 2018).
Src	Climbing-ripple cross-laminated fine- to medium-grained sand. Ripples are planar or trough cross-laminated and beds commonly show a fining-upward where a lamination with eroded ripple stoss sides passes upwards into lamination with preserved stoss sides and into draping lamination. Bed contacts are sharp, erosive or gradational.	Deposits of migrating 2D and 3D ripples. Deposition by waning subcritical sheetfloods or flows in glaciofluvial channels or waning subcritical low-density turbidity currents in glaciolacustrine settings. Climbing bedforms indicate high suspension fallout rates (Ashley *et al*. 1982). Upslope migrating climbing ripples may relate to cyclic steps (Tan & Plink-Björklund 2021).

Table 2. Measured radionuclide concentrations determined using gamma spectrometry, and calculated environmental dose rates.

Lab. ID	Sample ID	Depth (m)	Grain size (μm)	U (ppm)	Th (ppm)	K (%)	Dose rate (Gy ka^{-1})
Samples measured at LIAG (LUM)							
3699	Bol-1	4	150–200	0.38±0.02	1.21±0.06	0.59±0.03	1.47±0.12
3700	Schne-1	2	150–200	0.35±0.02	1.00±0.05	0.54±0.03	1.45±0.12
3701	Schne-2	3	150–200	0.49±0.03	1.41±0.07	0.84±0.04	1.73±0.13
3702	Eil-1	3.5	150–200	0.35±0.02	1.02±0.05	0.54±0.03	1.42±0.12
4911	1/1	4	125–180	0.80±0.04	2.81±0.14	0.69±0.03	1.66±0.13
4912	7/1	1.4	125–180	0.76±0.04	2.6±0.13	0.75±0.04	1.74±0.13
4915	12/2	1	125–180	0.34±0.02	0.97±0.05	0.78±0.04	1.58±0.13
4916	37b/1	4	125–180	0.65±0.03	2.13±0.11	0.77±0.04	1.65±0.13
4920	35/2	3	125–180	0.82±0.04	2.37±0.12	0.97±0.05	1.88±0.14
4921	35/3	1.5	125–180	0.42±0.02	1.17±0.06	0.57±0.03	1.43±0.12
4922	42/1	1.4	125–180	0.53±0.03	1.72±0.09	0.78±0.04	1.66±0.13
4923	52/1	4	125–180	0.44±0.02	1.16±0.06	0.67±0.03	1.47±0.13
4993[1]	25/1	2	125–180	0.74±0.12	2.37±0.17	0.95±0.10	1.87±0.15
4997[1]	49/1	1.5	125–180	0.41±0.08	0.83±0.07	0.63±0.07	1.46±0.13
5031	Wo/1	1.5	125–180	0.46±0.02	1.53±0.08	0.92±0.05	1.74±0.14
5032	Th/1	8	125–180	0.37±0.02	1.1±0.06	0.6±0.03	1.35±0.12
5033	58/1	0.8	125–180	0.75±0.04	2.53±0.13	0.83±0.04	1.81±0.14
5034	91/2	1.5	125–200	0.24±0.01	0.49±0.03	0.44±0.02	1.28±0.15
5035	69/1	5	125–180	0.40±0.02	1.31±0.07	0.65±0.03	1.44±0.13
Samples measured at MPI EVA (L-EVA)							
1544[1]	Mü-1-16	3	150–200	0.97±0.2	2.7±0.2	0.99±0.1	2.03±0.15
1545[1]	Ed-1-16	1	150–200	0.89±0.1	3.06±0.2	1.02±0.1	2.10±0.15
1548[1]	St-1-16	2	150–200	0.77±0.2	2.75±0.2	1.11±0.1	2.11±0.16
1549[1]	HBT-1-16	6	150–200	1.17±0.3	4.8±0.3	1.35±0.1	2.45±0.18
1579[1]	Scho-1-16	3	150–200	0.67±0.2	2.67±0.2	1.17±0.1	2.11±0.16
1580[1]	Scho-2-16	4.5	150–200	0.75±0.2	2.67±0.2	1.06±0.1	2.01±0.15

[1]Gamma spectroscopy measurements were carried out at Felsenkeller Laboratory, Dresden. The radionuclide concentrations for the other samples were measured at LIAG, Hanover.

Between 300 and 600 grains were measured for each sample, with 11% (12/1; LUM 4915 and 4997) to 31% (Scho-2-16; L-EVA 1580) passing all screening criteria (i–vi) and being used for L_nT_n D_e determination (Table S4). Previous studies have demonstrated that the D_e or L_n/T_n values of individual K-feldspar grains depend on signal sensitivity (T_n intensity) (Reimann *et al*. 2012; Guo *et al*. 2020; Long *et al*. 2024). Dim grains underestimate D_e values due to their lower potassium contents (resulting in lower internal dose rate) (Reimann *et al*. 2012; Guo *et al*. 2020), higher rates of anomalous fading (Guo *et al*. 2020) or failure in sensitivity correction (Jacobs *et al*. 2019). To investigate the dependence of L_n/T_n ratios on grain brightness, we conducted a 'T_n threshold plateau' test (Fig. 11) by plotting the minimum T_n responses of the selected grains (i.e. T_n threshold) against re-normalized L_n/T_n values of the selected grains (Guo *et al*. 2020). Three different patterns were observed for L_n/T_n variations: (i) re-normalized L_n/T_n values increased with T_n threshold and then reached a plateau (Fig. 11A); (ii) re-normalized L_n/T_n values showed no obvious trend with changes in T_n threshold (Fig. 11B) and (iii) re-normalized L_n/T_n values increased constantly, and no plateau was observed (Fig. 11C). For the first pattern, grains with T_n intensities above their corresponding thresholds where a plateau of L_n/T_n was observed were selected for D_e determination. In the second pattern, since the re-normalized L_n/T_n values did not

Table 3. pIRIR measurement protocols used in this study.

Step	K-feldspar single-grain pIRIR$_{290}$ protocol	K-feldspar single-grain pIRIR$_{275}$ protocol	Observed
1	Given regeneration dose	Given regeneration dose	
2	Preheat at 320 °C for 60 s	Preheat at 320 °C for 60 s	
3	IRSL using LEDs, 100 s at 50 °C	IRSL using LEDs, 200 s at 200 °C	
4	IRSL using IR laser, 2 s at 290 °C	IRSL using IR laser, 1 s at 275 °C	L_x
5	Given test dose	Given test dose	
6	Preheat at 320 °C for 60 s	Preheat at 320 °C for 60 s	
7	IRSL using LEDs, 100 s at 50 °C	IRSL using LEDs, 200 s at 200 °C	
8	IRSL using IR laser, 2 s at 290 °C	IRSL using IR laser, 1 s at 275 °C	T_x
9	Return to 1	IRSL, 100 s bleaching at 325 °C	
10		Return to 1	

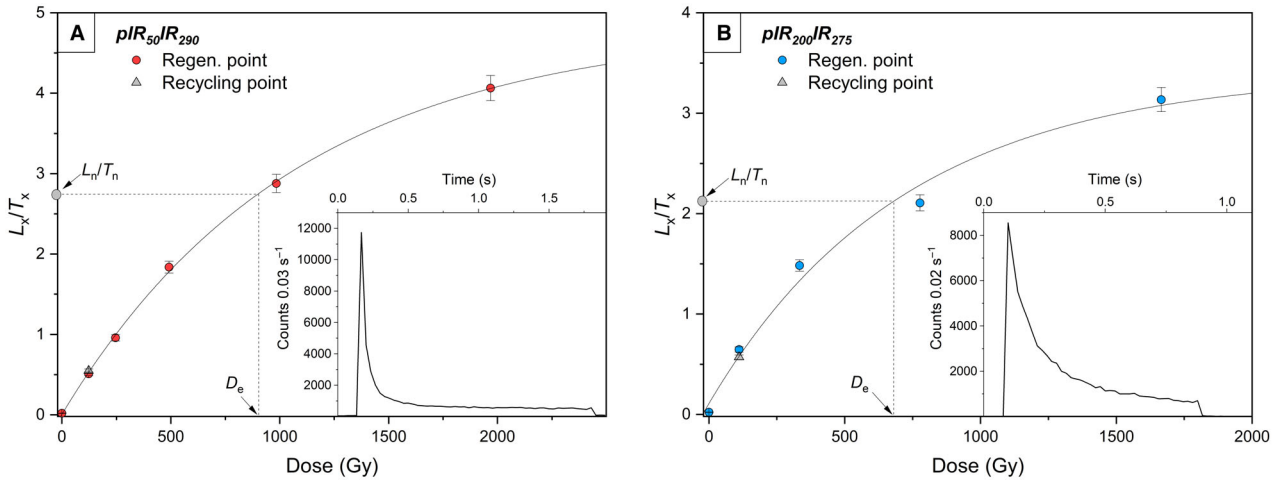

Fig. 9. Normalized sensitivity-corrected dose–response curves and natural decay curves (inset) for a grain of samples L-EVA 1549 (HBT-1-16) (A) and LUM 5031 (Wo/1) (B) measured using the $pIR_{50}IR_{290}$ and $pIR_{200}IR_{275}$ protocols, respectively.

change with grain brightness, all accepted grains were included in the D_e calculation. For the third pattern, the brightest 30% grains were used for D_e calculation, following Reimann *et al.* (2012). The results are summarized in Table 4.

For most samples from Elsterian deposits, the calculated L_n/T_n values exceeded 86% of the saturation signal intensity (I_{max}). As a result, minimum ages were determined by interpolating I_{max} onto the SGC. The single-grain ages range from >578 to 346±98 ka (Table 4). The feldspar single-grain luminescence ages of meltwater deposits of the first Saalian Drenthe (I) ice advance range in age from 293±59 to 209±37 ka (Table 4). The luminescence ages of meltwater deposits of the second Saalian Drenthe (II) ice advance range in age from 172±38 to 123±18 ka, and those attributed to the third Saalian Drenthe (III) ice advance are 123±22 ka in age (Table 4).

Depositional systems and chronology of Elsterian ice advances

The studied Elsterian meltwater deposits represent the upper fill of tunnel valleys and their marginal areas, which became partly upthrusted during the subsequent Saalian ice advances (Figs 3, 8G, 13F). Deposition most probably occurred during the retreat of the second Elsterian ice sheet (e.g. von Poblozki 1973, 1981; Meyer 1982, 1993; Caspers *et al.* 1995; Lang *et al.* 2012; Janszen *et al.* 2013; Steinmetz *et al.* 2015; Coughlan *et al.* 2018) and depositional systems comprise sand-rich subaqueous fans and deltas, which laterally and vertically partly pass into finer-grained silt and mud (cf. Meyer 1993; Janszen *et al.* 2013; Steinmetz *et al.* 2015).

The subaqueous fan deposits typically display a lobate, low-angle geometry (<10°) and commonly consist of whitish sand and pebbly sand, rich in reworked lignite (Figs 8B, C, 12, 13A, F). Thick sinusoidally stratified sand commonly alternates with normally graded, low-angle cross-stratified, trough-cross-stratified, sigmoidally stratified and (climbing)-ripple cross-laminated sand (Figs 12E, F, 13F). Wavelengths of the sinusoidal stratification range between 1 and 6 m. Finer-grained, thin-bedded sand-silt couplets occasionally occur. These sand beds are ripple cross-laminated and the silt beds are commonly structureless. Intercalated scour fills, 0.1 to 3 m deep and 2 to >4 m wide, consist of diffusely stratified to structureless, often amalgamated, fine sand (Figs 8B, 12D–F). The organic material is concentrated on the laminae of bedforms (mostly antidunes and ripples), accretion surfaces or amalgamation surfaces (Fig. 12B–F). Channel fills are scarce. A larger channel fill, approximately 30 m wide and up to 2 m thick, was exposed at the Thurauer Berg (pit 59). This channel had a sandy lateral infill, rich in reworked organic material.

The delta deposits display a steeper tangential geometry (>20°) than the subaqueous fans (Fig. 13B, C). Sandy delta-foreset deposits comprise thick beds of sinusoidally stratified medium to fine sand and pebbly sand, alternating with trough cross-stratified pebbly sand and (climbing-ripple) cross-laminated fine to medium sand (Fig. 13B, C, E). The exposed heights of sandy foresets range between 2 and 5 m. As in the subaqueous fan deposits, reworked organic material is commonly concentrated on laminae of climbing ripples or the larger bedforms (Fig. 13C, E). Coarser-grained delta foreset deposits consist of thin- to medium-bedded pebbly sand and fine gravel. Beds are structureless, normally graded or display low-angle cross-stratification and sinusoidal stratification.

The sand-rich subaqueous fans and deltas were deposited in glacial lakes that formed in underfilled tunnel valleys and their marginal areas. These whitish,

Table 4. D_e estimation details for age calculation using L_nT_n method.

Lab. ID	Sample ID	Number on maps	Glacigenic depositional environment	N_{sat} (%)[1]	Grain no.[2]	T_n threshold (cts 0.02 s^{-1}) (cts 0.03 s^{-1})[3]	OD (%)	D_e (Gy)	Age (ka)
Saalian Drenthe III or Warthe ice advances									
$pIR_{200}IR_{275}$									
4922	42/1	42	Glaciofluvial	14 (20%)	80/80/400	All	35±3	213±26	128±19
$pIR_{50}IR_{290}$									
1580	Scho-2-16	130	Glaciofluvial	6 (7%)	34/125/400	12 000	34±2	247±40	123±22
Saalian Drenthe II ice advance									
$pIR_{200}IR_{275}$									
4911	1/1	1	Glaciofluvial	13 (18%)	42/79/500	1600	33±3	263±40	159±27
4912	7/1	7	Glaciofluvial	17 (22%)	53/89/400	1500	38±3	288±46	166±29
4915	12/2	12	Glaciofluvial	12 (33%)	35/55/500	1000	37±4	237±43	150±30
4916	37b/1	37b	Glaciofluvial	22 (33%)	32/70/500	2000	40±3	283±58	172±38
5035	69/1	69	Glaciofluvial	15 (20%)	28/93/400	3380 (30%)	39±3	210±38	146±30
3702	Eil-1	91	Delta	4 (7%)	39/61/500	1000	33±3	175±21	123±18
5034	91/2	91	Glaciofluvial	5 (5%)	76/109/400	1000	26±2	192±18	150±23
3700	Schne-1	95	Subaqueous fan/delta	9 (13%)	29/79/500	4000	45±4	232±41	160±31
3701	Schne-2	95	Delta	5 (9%)	43/63/500	1500	35±3	240±38	139±24
$pIR_{50}IR_{290}$									
1579	Scho-1-16	130	Glaciofluvial/GLOF	0 (1%)	65/80/400	1500	27±2	335±38	159±22
1548	St-1-16	134	Subaqueous fan/GLOF	18 (15%)	40/141/500	12 500 (30%)	37±2	336±51	159±27
1545	Ed-1-16	150	Delta	3 (6%)	54/71/300	2000	36±3	297±39	141±21
Saalian Drenthe I ice advance									
$pIR_{200}IR_{275}$									
4997	49/1	49	Glaciofluvial	20 (43%)	53/53/500	All	32±3	427±76	293±59
5031	Wo/1	60	Delta	8 (13%)	55/63/500	500	27±2	387±64	222±41
$pIR_{50}IR_{290}$									
1549	HBT-1-16	135	Subaqueous fan/delta	10 (8%)	42/141/600	15 000 (30%)	31±2	511±82	209±37
1544	Mü-1-16	151	Delta	5 (10%)	20/52/300	8000	35±3	525±94	259±50
Elsterian ice advances									
$pIR_{200}IR_{275}$									
4993	25/1	25	Tunnel valley (subaqueous fan/delta)	47 (52%)	95/95/500	All	28±2	>719	>385[4]
4920	35/2	35	Tunnel valley (subaqueous fan/delta)	44 (45%)	113/113/500	All	19±1	>560	>298[4]
4921	35/3	35	Tunnel valley (delta)	9 (18%)	40/65/400	1500	28±3	522±72	365±59
4923	52/1	52	Delta	51 (48%)	115/115/500	All	26±2	>624	>425[4]
5033	58/1	58	Tunnel valley (subaqueous fan)	20 (34%)	72/72/400	All	21±2	>721	>398[4]
5032	Th/1	59	Tunnel valley (subaqueous fan)	56 (66%)	91/91/500	All	18±1	>777	>578[4]
3699	Bol-1	90	Glaciofluvial	13 (26%)	24/55/500	3000	36±4	510±139	346±98

[1]Number of saturated grains.
[2]The three grain numbers represent the total number of brightest grains used for L_n/T_n and D_e calculation (left), the number of grains that passed screening criteria i to vi (middle) and the total number of grains measured (right).
[3]Time per datapoint is 0.02 and 0.03 s for $pIR_{200}IR_{275}$ and $pIR_{50}IR_{290}$, respectively.
[4]Minimum age, as the MAM LS-normalized L_n/T_n values are greater than the 86% of the I_{max} (signal intensity at saturation) of the constructed SGC.

organic-matter bearing sands are widely distributed in north-western Germany and fill a remnant relief (e.g. Meyer 1982, 1993; Grube 2015). The common superposition of subaqueous fans or larger deltas by small deltas indicates the filling of the accommodation space (Fig. 13A, B, F, G).

The gentle dip, lobate geometry and frequent occurrence of sinusoidal stratification indicate deposition in a proximal lobe environment of subaqueous fans where laterally spreading fields of stable antidunes formed (cf. Lang *et al.* 2017, 2021a, b). The thick beds of stable antidunes reflect deposition by highly aggradational quasi-steady supercritical density flows (Lang & Winsemann 2013; Cartigny *et al.* 2014; Lang *et al.* 2017, 2021a, b). Isolated, shallow lenticular beds with structureless, concentric or lateral infills are interpreted as scour fills formed by antidune-wave breaking (Blair 1999; Alexander *et al.* 2001; Duller *et al.* 2008; Cartigny *et al.* 2014). Laterally and vertically stacked larger scour fills or coalesced, amalgamated scour fills (Figs 8B, 12D, F) indicate rapid cut-and-fill processes by Froude supercritical density flows (Gorrell & Shaw 1991; Leclair

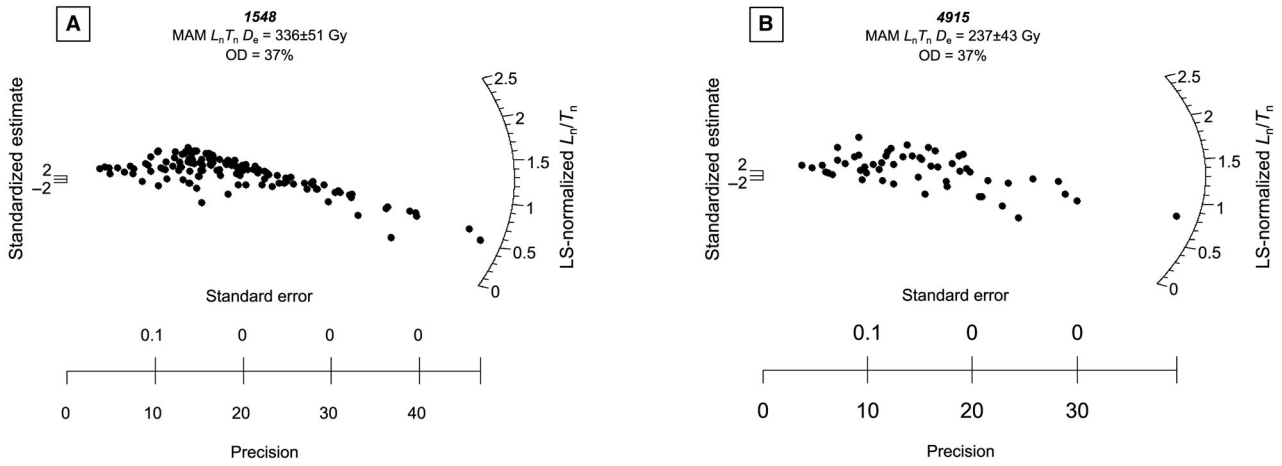

Fig. 10. Example of distributions of re-normalized L_n/T_n for two samples measured using the $pIR_{50}IR_{290}$ (A) and $pIR_{200}IR_{275}$ (B) protocols.

& Arnott 2005; Hofstra *et al.* 2015; Pohl *et al.* 2023). Amalgamated scour fills represent several successive flow events (e.g. Pohl *et al.* 2019). Meter-thick sigmoidally stratified sand beds below the sinusoidally stratified lobe deposits (Fig. 8C) may either represent hydraulic jump bars, which formed at the mouth of channels (MacDonald *et al.* 2009; Winsemann *et al.* 2011; Hamilton *et al.* 2015, 2017; Lang *et al.* 2021a) or humpback dunes that formed under transcritical flow conditions (Lang & Winsemann 2013; Lang *et al.* 2017, 2021b).

The delta foresets were also commonly deposited by supercritical density flows. The steep tangential geometry points to the formation of Gilbert-type deltas and/or shallow-water mouth-bar deltas (cf. Winsemann *et al.* 2018, 2021). Low-angle to sinusoidal stratification indicates the deposition by stable antidunes (Fig. 8B, C, E). The association of antidune and humpback-dune deposits is characteristic for transcritical density flows and (climbing-ripple) cross-lamination reflects deposition by (waning) subcritical density flows (e.g. Lang & Winsemann 2013; Lang *et al.* 2017; Winsemann *et al.* 2018, 2021).

Reworked organic material has previously been described from tunnel-valley deposits and attributed to plume sedimentation of suspended material (Janszen *et al.* 2013). However, our outcrop data show that the high concentration of organic material in both subaqueous fan and delta deposits is related to the deposition by highly aggradational, quasi-steady supercritical density flows (Lang & Winsemann 2013; Lang *et al.* 2017), which enabled the preservation of organic material. The preferred concentration of organic material on the laminae of antidunes (Figs 8C, E, 12C, E, F, 13C, E) requires flow unsteadiness, which may be related to Kelvin–Helmholtz instabilities along the upper interface of the density flows, leading to rapid waxing–waning cycles (cf. Cartigny *et al.* 2013; Slootman *et al.* 2021; Spychala *et al.* 2025) or lower frequency flow unsteadiness caused by the upstream formation of hydraulic jumps (cf. Ono *et al.* 2021; Slootman *et al.* 2021; Spychala *et al.* 2025). The deposition of climbing-ripple cross-laminated sand with organic material (Fig. 12B, C) is attributed to waning low-density turbidity flows, as is indicated by the upwards increasing angle of climb and decreasing grain size (cf. Ashley *et al.* 1982; Winsemann *et al.* 2018). The organic material and well-sorted, fine-grained sand were likely reworked from underlying Miocene and Paleogene lignite-bearing shallow-marine deposits (Figs 3, 8G; cf. Schneekloth & Sickenberg 1968; Meyer 1982, 1993, 2009).

Depositional systems and chronology of the Saalian Drenthe (I, II, III) ice advances

During the first two Saalian Drenthe (I, II) ice advances, large ice-dammed lakes formed south of the North German Lowlands. The related ice-marginal delta and subaqueous fan systems (Fig. 14A–E) were studied in detail by Winsemann *et al.* (2003, 2004, 2009, 2011, 2018, 2021), Hornung *et al.* (2007) and Lang *et al.* (2017, 2018, 2021b). North of the Rehburg line (Fig. 1A), mainly glaciofluvial sediments were deposited (e.g. Sindowski 1969a, b; van Gijssel 1987; Lang & Winsemann 2013; Lang *et al.* 2021b).

The Saalian meltwater sediments, which are incorporated in and onlap the glaciotectonic complex of the Rehburg line north of the North German Uplands, mainly consist of glaciolacustrine deposits (cf. van der Wateren 1994; Lang *et al.* 2021b), which partly overlie Elsterian till. These subaqueous fan and delta deposits consist of whitish fine- to medium-grained sand and pebbly sand that partly contain reworked organic material from underlying Neogene and older Pleistocene sediments (Jordan 1980). Sedimentary structures comprise sinusoidal stratification, planar cross-stratification, (climbing) ripple cross-lamination or normal grading.

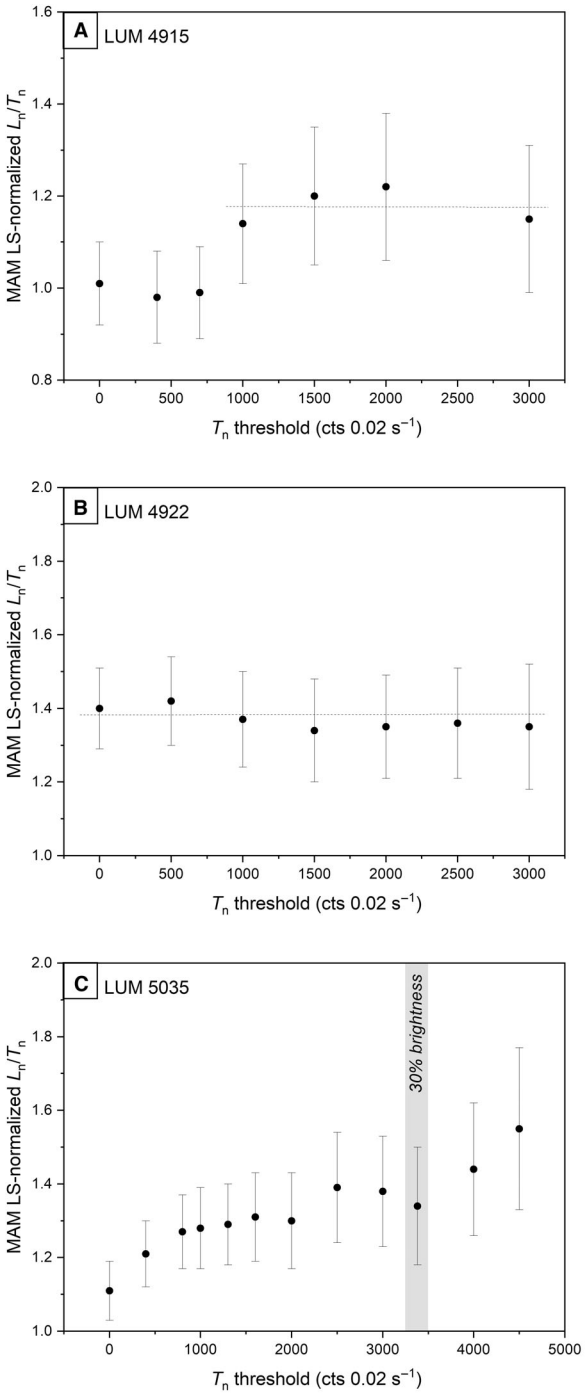

Fig. 11. MAM LS-normalized L_n/T_n values plotted as a function of T_n threshold, showing three distinct patterns of L_n/T_n variation with increasing T_n threshold. A. Increase to a plateau, with grains above the plateau threshold was used for D_e determination. B. No clear trend, with all accepted grains included. C. Continuous increase, where the brightest 30% of grains (grey bar) were selected. The dashed lines indicate the LS-normalized L_n/T_n plateau.

Scour fills are commonly structureless, normally graded, diffusely stratified or backset cross-stratified (Fig. 4B, C, F). These pre- and syntectonic glaciolacustrine deposits were deformed and overridden by the first and second Saalian Drenthe (I, II) ice sheet. During subsequent ice sheet retreat, glaciofluvial and shallow-water deltas were deposited, partly forming coarse-grained isolated mound-shaped sediment bodies on top of the glaciotectonic ridges (Fig. 4H; cf. Voss 1979, 1982; Jordan 1980).

Further west, in the lower Rhine Embayment, small, steep glaciofluvial fans formed on the ice-distal lee side of composite ridge systems. These fans are up to 25 m thick and up to 5.5 km long (Fig. 5A–C). Previous studies reported a dominance of supercritical to transcritical bedforms, including deposits of cyclic steps, breaking antidunes, stable antidunes and humpback dunes (Lang & Winsemann 2013; Winsemann *et al.* 2016). The uppermost successions comprise thin layers of matrix-supported diamicton, interpreted as flow till from the ablating ice front (Fig. 5D–F).

The glaciofluvial sediments, which are incorporated in or onlap the glaciotectonic complexes further north, are characterized by tabular sandy sheetflood deposits, alternating with coarser-grained single storey, multilateral or multistorey channel bodies (Figs 6, 7). In tunnel valleys and their marginal areas, partly fine-grained glaciolacustrine deposits occur (cf. Sindowski 1969a; von Poblozki 1973, 1981; Janszen *et al.* 2013; Steinmetz *et al.* 2015). Sheetflood deposits are 4–70 cm thick and mainly consist of sinusoidally stratified medium to fine sand or pebbly sand. Wavelengths range between 0.7 and 8 m; most common are wavelengths between 0.7 and 3 m. (Climbing) planar ripple or ripple-trough cross-laminated sheetflood deposits consist of thin- to thick-bedded (8–70 cm) fine sand (Figs 6D, 7E). Beds with climbing-ripple cross-lamination often show a fining-upwards where a lamination with eroded ripple stoss sides passes upwards into lamination with preserved stoss sides. The sheetflood deposits commonly form packages, approximately 0.25–2.5 m thick, that fine or coarsen upwards.

Single-storey channel bodies are rare and occur in sheetflood-dominated successions. They are 0.3–2.5 m wide, 0.04–0.7 m thick and have concave or lateral infills of fine to medium sand and silt, which commonly display ripple-trough cross-lamination. The width to thickness ratios range between 3.3 and 10.

Multilateral channel bodies are 0.65 m to more than 8 m wide, 0.04–0.5 m thick and commonly form broad gravel sheets (Fig. 6D). They show a lateral amalgamation of several channels at the same stratigraphic level and a composite basal surface of erosion. Because of the amalgamation and outcrop conditions, the number and true widths of individual channels are difficult to estimate. The width to thickness ratios range between 4.3 and 100. The internal architecture of individual channels consists of a single bar macroform and a laterally adjacent concentric or trough cross-stratified sandy or gravelly fill. The bars partly have a lower coarse-grained

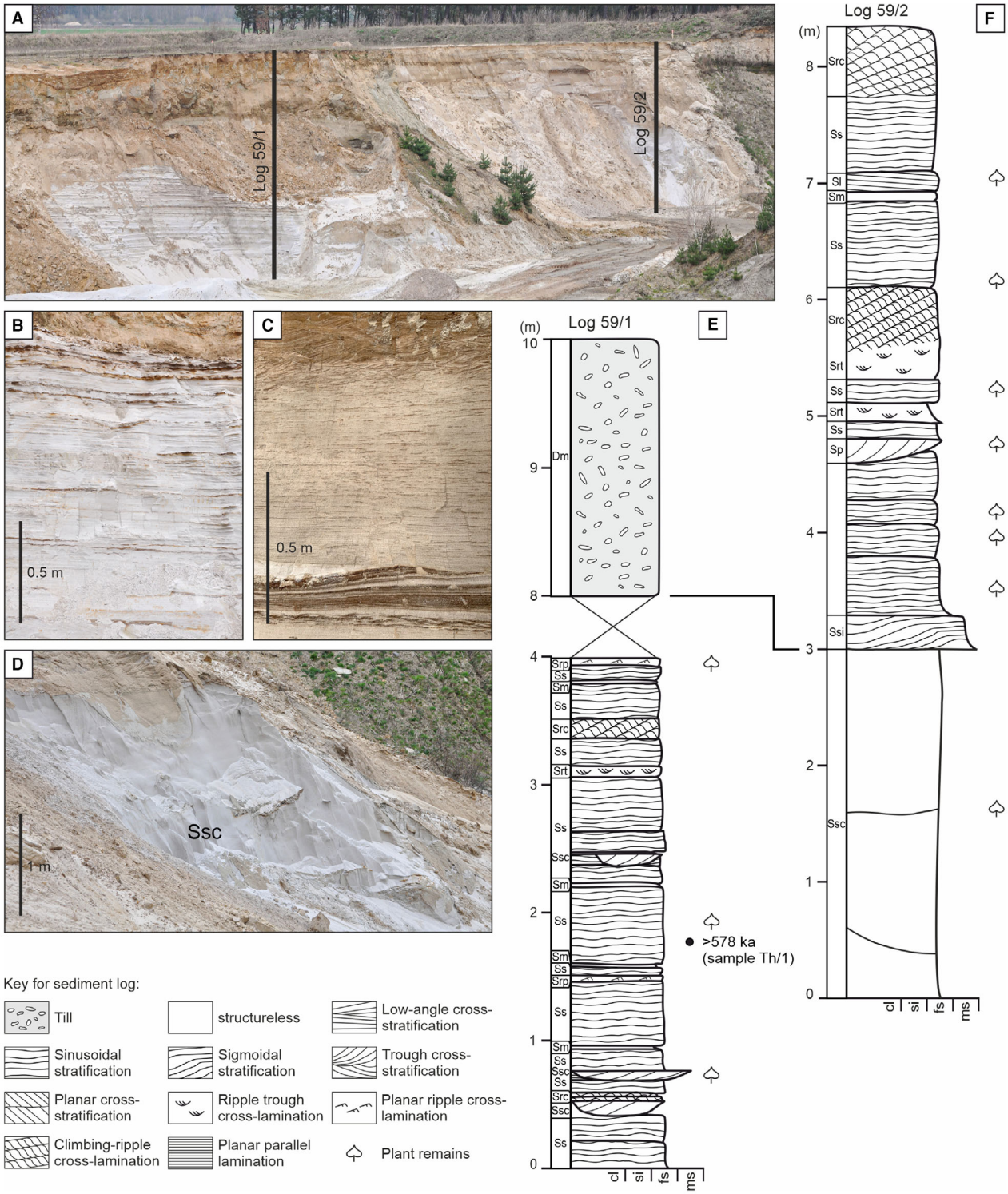

Fig. 12. Sedimentary facies of Elsterian glaciolacustrine subaqueous-fan deposits. A. Overview figure, showing glaciolacustrine deposits, overlain by Warthian till and the location of sediment logs (pit 59, Thurauer Berg). B. Thin- to medium-bedded antidune deposits, alternating with ripple-cross-laminated sand, rich in reworked lignite (distal lobe deposits of the lower succession; log 59/1, 2.5–4 m). C. Thick antidune deposits, overlain by climbing-ripple cross-laminated sand, both rich in reworked lignite (proximal lobe deposits of the upper succession; log 59/2, 4.6–6 m). D. Large amalgamated scour-fill (Ssc) with reworked lignite (log 59/2, 0–3 m). E. and F. Sediment logs with luminescence age. For key, see this figure and Table 1. For location, see Fig. 1A, B and Table S1.

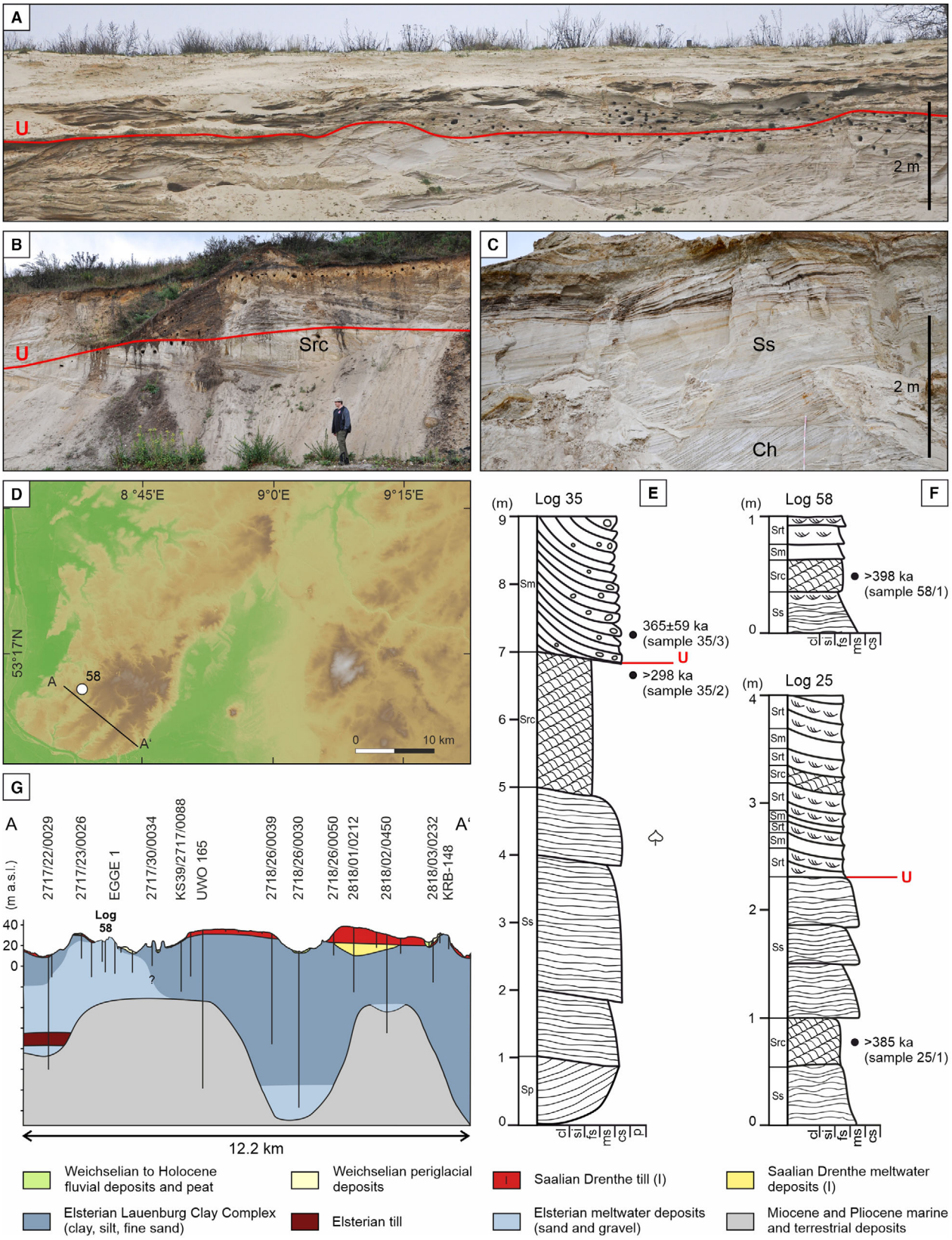

Fig. 13. Sedimentary facies of Elsterian glaciolacustrine deposits. A. Glaciotectonically deformed subaqueous fan deposits are unconformably overlain by delta deposits, characterized by tangential foresets (Pit 25 Bötersen). Red line indicates the unconformity (U). B. and C. Vertically stacked delta deposits, exposed in pit 35. C. The lower delta deposits consist of channelized planar cross-stratified sand (Sp), overlain by thick antidune deposits (Ss) and climbing-ripple deposits (Src), which are partly rich in reworked lignite (see black intercalations in the uppermost deposits). These delta deposits are unconformably overlain by delta foreset deposits, which consist of coarser-grained, structureless to subhorizontally stratified pebbly sand. D. Digital elevation map of the study area showing the location of pit 58 and the cross-section shown in (F). E. Sediment log of pit 25 (Bötersen). F. Sediment log of pit 58 (Eggestedt) and pit 35 (Wesendorf). For key, see Fig. 12 and Table 1. G. Cross-section of Elsterian tunnel-valley fills near Eggestedt. For location, see Fig. 1A, B and Table S1.

pebbly or gravelly planar cross-stratified interval, passing upwards into low-angle cross-stratified and/or sinusoidally stratified sand (Figs 6D, 7G).

Multistorey channel bodies consist of laterally and vertically stacked amalgamated channels, which commonly have a lateral to concentric infill. Trough cross-stratified fills are rare and consist of pebbly sand and sandy gravel with 0.1–0.3 m thick cross-sets (Fig. 6C). Rarely, fine-grained multistorey channel fills occur, which consist of (climbing) ripple-cross-laminated fine sand and silt (Fig. 7G). Individual channels are 0.20–1.5 m thick and 2–8 m wide. However, the outcrop conditions do not allow for an estimation of the number and true widths of individual channels and size of the channel belts. The vertical stacking pattern of these glaciofluvial deposits displays a common decrease in the number and thickness of sheetflood deposits and an increase in the number, size and amalgamation of channel bodies (Fig. 7B).

The glaciolacustrine delta and subaqueous fan deposits, which are incorporated in the glaciotectonic complex of the Rehburg line, were shed into ice-dammed glacial lakes that formed between the Saalian Drenthe (I, II) ice sheets and the North German Uplands (van der Wateren 1994; Lang *et al.* 2018). The sedimentary facies types resemble those of the Elsterian depositional systems (Figs 4B, C, F, 8E), deposited by supercritical density flows (van der Wateren 1994; Lang *et al.* 2021b). The frequent occurrence of organic material points to the subglacial reworking of Miocene and/or Paleogene lignite-bearing shallow-marine deposits. During further ice-sheet advance, these glaciolacustrine deposits were overridden and partly incorporated into the glaciotectonic complex of the Rehburg line.

The sand-rich meltwater deposits of the northern part of the study area that overlie the first Saalian Drenthe (I) till represent glaciofluvial deposits, which form part of small, steep glaciofluvial fans (cf. Zieliński & van Loon 2000, 2003; Kjær *et al.* 2004; Pisarska-Jamroży 2008; Mleczak *et al.* 2021) or larger shallow outwash plains with a downstream distributive runoff pattern (cf. Zieliński & van Loon 2003; Weissmann *et al.* 2010; Pisarska-Jamroży & Zieliński 2014; Moscariello 2018). Tabular sheetflood deposits with low-angle cross-stratification and sinusoidal stratification indicate upper-flow regime deposition by breaking or aggrading stable antidunes (Fielding 2006; Duller *et al.* 2008; Blair & McPherson 2009; Lang & Winsemann 2013; Lang *et al.* 2021a; Winsemann *et al.* 2022) and probably record high discharge events during the melt season (cf. Kjær *et al.* 2004; Pisarska-Jamroży 2008; Fielding *et al.* 2009; Pisarska-Jamroży & Zieliński 2014; Peng *et al.* 2017; Mleczak *et al.* 2021; Winsemann *et al.* 2022). The dominance of aggrading stationary antidune deposits may have been controlled by grain size (cf. Ono *et al.* 2021).

Isolated single-storey channel fills with low aspect ratios record fixed channels in a distal fan environment, which was dominated by sheetfloods (cf. Krzyszkowski & Zieliński 2002). They either record ephemeral streams (Gibling 2006) or rapid cut-and-fill processes during sheetfloods (van Dijk *et al.* 2009; Hamilton *et al.* 2013). The average wavelength of stationary antidunes (L) scales with the depth of the water flow (h), and wavelength can therefore be used to estimate flow palaeodepths of sheetfloods ($L = 2\pi h$) (Allen 1984). From this equation and the range of wavelengths (0.2–8 m), the water depth during stationary antidune formation was up to approximately 1.3 m.

The predominance of lateral accretion elements in multilateral channel bodies points to sinuous distributary channel networks with higher lateral migration rates in a distal mid-fan environment (Gibling 2006; Blair & McPherson 2009; Huerta *et al.* 2011; Meinsen *et al.* 2014; Lowe & Arnott 2016; Winsemann *et al.* 2022) or the medial area of larger glaciofluvial distributive systems (e.g. Moscariello 2018). The incision of these channels probably occurred during the falling stage of the sheetfloods or a subsequent reduced discharge (Gibling 2006; Blair & McPherson 2009; Peng *et al.* 2017). Low-angle cross-stratified, planar cross-stratified to sigmoidally cross-stratified pebbly sand and sand (Figs 6D, E, 7B, G) may represent bars that formed during high or rising water depths. Vertically, the planar to sigmoidally cross-stratified pebbly sand or sandy gravel frequently passes into subhorizontal or sinusoidal stratification (Fig. 7G), indicating the transition from subcritical to supercritical flow conditions during vertical bar accretion caused by the local decrease in flow depth above the bars (cf. Zieliński & van Loon 2003; Pisarska-Jamroży & Zieliński 2014; Lang *et al.* 2021a). Alternatively, these bedforms may represent humpback dunes that formed under transcritical sheetflood conditions (Lang & Winsemann 2013). Deeper multistorey channelfills (Figs 6B, 14G) indicate higher water depth and a reoccupation of previously abandoned channels

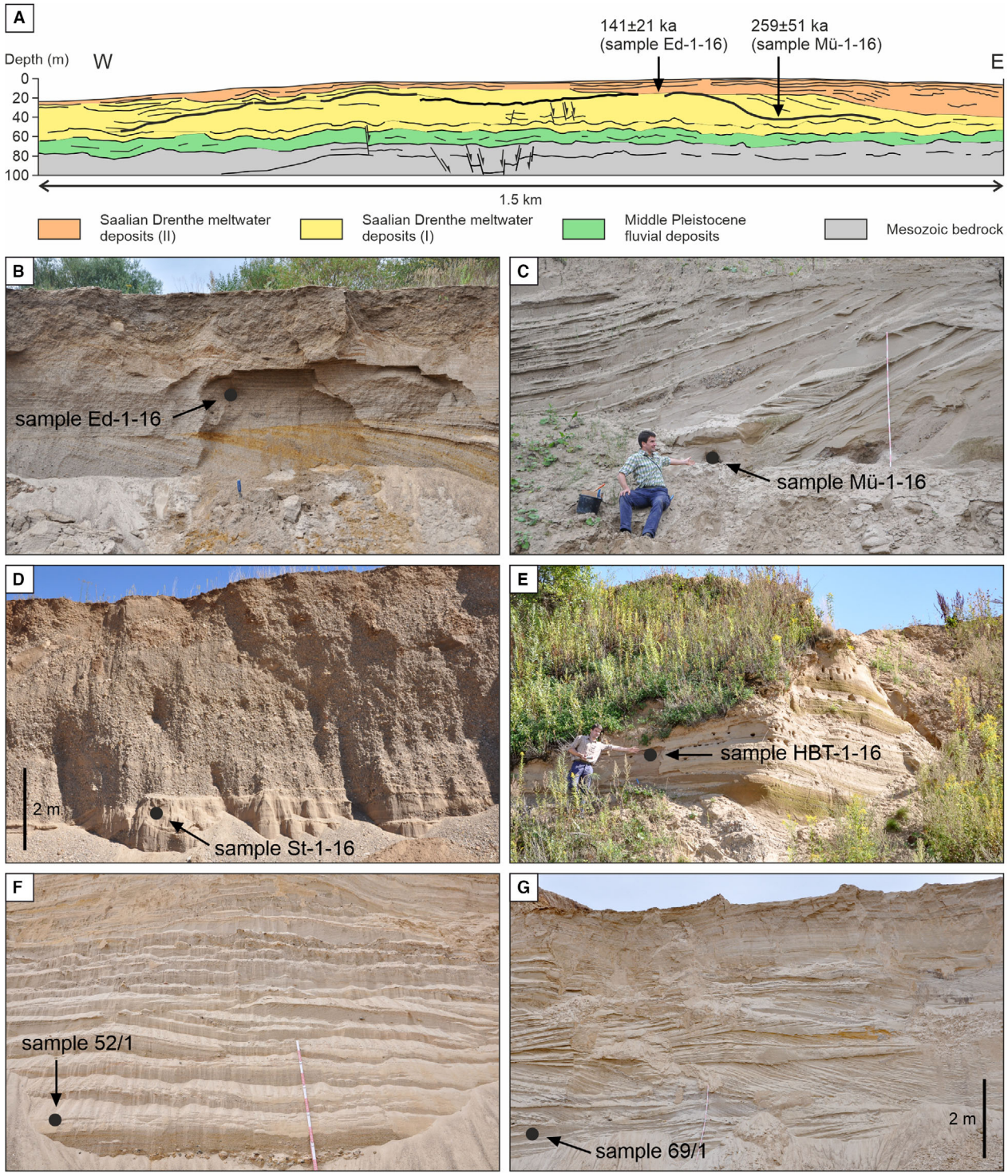

Fig. 14. Sedimentary facies of Saalian glaciolacustrine and glaciofluvial deposits. A. Cross-section of the Porta subaqueous fan and delta complex (modified from Winsemann *et al.* 2009, 2018) with new luminescence ages. B. Uppermost coarse-grained shallow-water delta deposits of the Porta complex with sample location (pit 150 Edler). C. Gilbert-type delta deposits, unconformably onlapping the central subaqueous fan of the Porta complex with sample location (pit 151 Müller). D. Deposits of the Coppenbrügge subaqueous-fan complex with sample location (pit 134 Steinbrink). These deposits may represent glacial lake-outburst flood deposits. E. Uppermost sandy deposits of the Coppenbrügge subaqueous fan complex with sample location (pit 135 HBT). These deposits may represent glacial lake-outburst flood deposits. F. Glaciolacustrine delta deposits with sample location (pit 52 Bispingen). G. Glaciofluvial deposits exposed in pit 69 (Volkstorf) with sample location. For location, see Fig. 1A, B and Table S1.

after local avulsion in a more proximal environment (cf. Zieliński & van Loon 2003; Gibling 2006; Huerta *et al*. 2011; Moscariello 2018).

The vertical stacking patterns of architectural elements commonly point to prograding glaciofluvial systems, indicated by the transition from single-storey channels to more sinuous multilateral channel bodies to amalgamated multistorey channel bodies as well as the increase in width and depth of channels (cf. Zieliński & van Loon 2003; Pisarska-Jamroży 2008; Pisarska-Jamroży & Zieliński 2014; Moscariello 2018; Winsemann *et al*. 2022). These glaciofluvial deposits were subsequently partly upthrusted and incorporated into the Altenwalde and Lamstedt composite ridge systems. The post-tectonic small glaciofluvial fans on the ice-distal lee side of the glaciotectonic ridges are very similar to ice-marginal fans (also referred to 'terminoglacial fans'), which were described from Poland (Zieliński & van Loon 2000; Pisarska-Jamroży 2008; Mleczak *et al*. 2021) and Iceland (Kjær *et al*. 2004). The fans on the lee side of the glaciotectonic ridges of the Lower Rhine Embayment may partly record GLOF deposits from the Weser Lake (Lang & Winsemann 2013; Winsemann *et al*. 2016). Similar sedimentary successions were described from Poland and interpreted as chute bars that formed in distal fan areas during the waning stage of GLOFs (Weckwerth *et al*. 2024).

Depositional systems and chronology of the younger Saalian Warthe ice advance

Meltwater deposits of the younger Saalian Warthe ice advance are sparse in the study area and related glacigenic deposits mainly consist of till, which covers large areas of the north-eastern part of the study area. Meltwater deposits south of the Lamstedt composite ridge system (Fig. 7A, B log 42) may be Warthian in age (128±19 ka; Table 4) or belong to a retreat phase of the second Saalian Drenthe (II) ice sheet. Fine-grained lake bottom sediments, which fill an intervening (syntectonic?) basin between glaciotectonic ridges of the Salzwedel composite ridge system (Fig. 8F, G), were dated in a previous study by Rahimzadeh *et al*. (2024). The fading corrected multiple-grain pulsed IR_{50} and pulsed $pIRIR_{225}$ feldspar ages (Fig. 8F) range between 146±20 and 123±12 ka, probably recording continuous sedimentation between the second Saalian Drenthe (II) ice advance and the Eemian. OSL and $pIRIR_{225}$ ages of meltwater deposits in north-eastern Germany, which were correlated with the Warthian ice advance, range from 155±21 to 130±17 ka (Lüthgens *et al*. 2010; Kenzler *et al*. 2018).

Discussion

Reliability and consistency of luminescence dating

The dated ice-marginal deposits consist of glaciolacustrine fans, deltas and glaciofluvial deposits with partly short transport distances. Some of these sediments may therefore have been exposed to sunlight for a rather short period, potentially leading to insufficient bleaching of the feldspar luminescence signal (cf. Fuchs & Owen 2008; King *et al*. 2014; Weckwerth *et al*. 2024; Kalińska *et al*. 2025; Krauß *et al*. 2025). Dating tunnel-valley fills presents an even greater challenge, as these sediments are mainly deposited subglacially and may contain reworked older material that did not experience sunlight exposure before re-deposition (e.g. Buechi *et al*. 2024). Consequently, establishing a reliable chronology that distinguishes between substages of ice advances during the Saalian and Elsterian glaciations remains difficult.

To address this problem, the single-grain measurement was used to isolate well-bleached grain populations. The difference between single-grain and multiple-grain age estimates is significant, ranging from 20 to 350 ka (Tables 4, S3), highlighting the impact of partial bleaching in many of the studied samples. We argue that all new single-grain age estimates presented and discussed in this study deliver a robust chronological framework but it should also be considered that luminescence signals measured at elevated temperature (i.e. 275 °C and 290 °C) might tend more towards age overestimation if compared to feldspar signals stimulated at slightly lower (here 225 °C) temperature ranges (e.g. Li & Li 2011). On the other hand, lower stimulation temperatures might tend towards stronger anomalous fading, and therefore fading correction becomes necessary. For the samples analysed in this study, where the natural signal lies in the non-linear part of the DRC, the fading correction model of Kars *et al*. (2008) is considered the most appropriate correction method. However, applying this model requires constructing the DRC up to full saturation, which significantly increases measurement time in single-grain analyses. To avoid this, we aim to measure pIRIR signals at elevated temperatures, which are known to be free of fading.

In addition, a detailed methodological study was conducted by Rahimzadeh *et al*. (2026), using six samples from this study (samples 1/1, 7/1, 37b/1, 35/3, 69/1 and 91/2; Table 4). They investigated different approaches to date these glacigenic sediments, analysing single-grain data sets using both standard single-grain analysis and the L_nT_n method. Their initial analysis focused on accepted grains from which the saturated grains were excluded. The study concluded that the L_nT_n approach is the most suitable method for age estimation in such contexts. A comparison of ages obtained using both approaches (standard single-grain analysis and the L_nT_n method) shows that the standard MAM ages slightly underestimate the MAM L_nT_n ages, probably because excluding saturated grains truncates the D_e distribution. This highlights the importance of including saturated grains, as they may contain valuable information critical to accurate D_e estimation. Systematic rejection of these

grains can introduce significant bias into age calculations.

Luminescence signal properties in different depositional environments. – As mentioned in the previous section, the studied samples contain between 1% and 66% saturated grains (Table 4). The Elsterian deposits show the highest proportion of saturated grains, with an average of 44% of grains in saturation. One possible explanation for this high percentage is the considerable age of these samples (e.g. ≥MIS 12), suggesting that they are close to or possibly beyond the upper limit of feldspar luminescence dating in this region. Another factor could be their depositional environment. All Elsterian samples were taken from upthrusted tunnel-valley fills. Samples from subaqueous fan systems (Table 4, samples Th/1, 25/1, 58/1) were most probably deposited by subglacial meltwater streams and exposure to sunlight and thus bleaching of the luminescence signal is unlikely. In contrast, the sampled delta deposits of the uppermost tunnel-valley fills (Table 4) that partly overly the subaqueous fan systems have higher chances of luminescence signal resetting (cf. Fuchs & Owen 2008; Lang *et al.* 2018; Buechi *et al.* 2024) and were at least partially bleached and datable.

In contrast, the Saalian delta and glaciofluvial deposits commonly exhibit lower proportions of saturated grains, with averages of 18%, 13% and 7% for the different ice advances. Although glaciofluvial and glacigenic delta deposits are also susceptible to incomplete bleaching (e.g. Fuchs & Owen 2008; Thrasher *et al.* 2009; Alexanderson & Murray 2012; Weckwerth *et al.* 2013; King *et al.* 2014), they generally show better bleaching than the tunnel-valley deposits. The study of Alexanderson & Murray (2012) showed that a rapid, significant bleaching takes place from subglacial to proglacial sediments, which occurred in a distance of approximately 1 km, suggesting that large age overestimation in subaerial and subaqueous deposits due to incomplete bleaching is mainly restricted to deposits very close to the ice margin. Distal glaciofluvial deposits therefore may be well bleached. Furthermore, glaciofluvial sediments typically undergo several phases of erosion, transport, and redeposition before final burial (Thrasher *et al.* 2009; Weckwerth *et al.* 2013; King *et al.* 2014), offering moderate potential for signal resetting (Fuchs & Owen 2008). As a result, a mix of grain populations is expected in these settings: some grains may have been fully bleached at the time of deposition, others only partially bleached and some may remain entirely unbleached (i.e. saturated). Further important parameters in subaerial glaciofluvial environments are water depths and flow properties, which control the turbulence, density, viscosity and thus the related transport mode in and bleaching potential of specific subenvironments such as channels and overbank areas (Thrasher *et al.* 2009; Weckwerth *et al.* 2013; King *et al.* 2014). Our glaciofluvial samples were taken from shallow channel fills and the uppermost part of shallow bars. According to Thrasher *et al.* (2009), the upper parts of bars that formed under waning flow conditions (often comprising ripple cross-laminated sand or (sub)horizontally stratified sand) have the best chance of bleaching, especially when they emerged. In contrast, large-scale cross-stratified sand that was deposited in deep channels tends to overestimate ages because the sand was transported and deposited in deep, fast-flowing turbid sediment-laden currents and experienced poor bleaching. These results are supported by the study of Weckwerth *et al.* (2013), who showed that ripple cross-laminated sand deposited in overbank areas and horizontally stratified shallow channel-fills are better bleached than sandy deposits of deep channel fills and therefore are more suitable for luminescence dating than larger compound bars deposited in deeper channels.

In contrast to the studied glaciofluvial depositional systems (e.g. Fuchs & Owen 2008; Thrasher *et al.* 2009; Alexanderson & Murray 2012; Weckwerth *et al.* 2013; King *et al.* 2014), no consistent relationship between bleaching characteristics and transport distance and/or sedimentary structures was found in GLOF deposits. The best bleaching of these GLOF-related sediments occurred during the final stage of flood (cf. Kalińska *et al.* 2025), when the flow velocities decreased and the flows were likely depleted of sediment. This might also apply to our field examples (samples St-1-16, Scho-1-16).

Comparison with age estimates of previous studies. – During the last decade, several luminescence-dating studies were conducted to determine the chronology of Elsterian and Saalian ice advances into northern Germany. As quartz is commonly in saturation in Elsterian and Saalian deposits, all these luminescence-dating approaches focused on feldspar dating. The approaches mainly used elevated temperature approaches to minimize the effect of fading. For instance, Lang *et al.* (2018) and Lauer & Weiss (2018) used a $pIRIR_{290}$ approach, whereas Winsemann *et al.* (2022) and Rahimzadeh *et al.* (2024) applied $pIRIR_{225}$ protocols, with the latter incorporating pulsed stimulation with fading correction. An earlier study by Roskosch *et al.* (2015) used pulsed stimulation at 50 °C, which is known to have fading rates as low as those of pIRIR signals and also bleach as fast as IR_{50} signals (Tsukamoto *et al.* 2017). Infrared-Radiofluorescence (IR-RF) dating, which is known to be less affected by anomalous fading, was used by Krbetschek *et al.* (2008) to gain insights into the timing of the Saalian glaciation. Previously published ages may therefore be affected by different biases (fading; age over-/underestimation) that can complicate direct comparisons between studies. While fluvial and especially meltwater sediments can be challenging for trapped charge dating due to incomplete bleaching and/or fading, methodological advances in the last decade have

significantly improved the robustness of age estimates. However, validating these luminescence chronologies against independent age control is often difficult. Volcanic tephra, often used for such cross checks, are not preserved in the study area. Similarly, estimating minimum ages for the Saalian or Elsterian tills using overlying loess-palaeosol sequences is often not possible, as the tills/meltwater sediments of Fennoscandian ice sheets are located north of the European loess belt (cf. Lehmkuhl *et al.* 2016). Furthermore, the available chronologies are often based on the dating of different depositional systems. For instance, Busschers *et al.* (2008) and Lauer & Weiss (2018) dated fluvial sediments preserved between the Saalian and Elsterian tills to obtain minimum or maximum ages for the Middle Pleistocene ice sheet extensions, whereas Roskosch *et al.* (2015) and Lang *et al.* (2018) dated ice-marginal sediments with a close temporal/spatial relationship to the ice sheets. These sediments show significant differences in their bleaching behaviour, which further complicates direct comparison of age estimates across studies.

Chronology of ice advances during the Elsterian and Saalian glaciation into north-western and central Europe

Comparison with the marine record and onshore data from north-western and central Europe. – From the sedimentary record of the Bay of Biscay, increased meltwater input has been reconstructed for the times around 455 ka (MIS 12), 340 ka (MIS 10), 270 ka (MIS 8), 155 ka (MIS 6) and 18 ka (MIS 2). Ice-sheet reconstructions by Batchelor *et al.* (2019) show that during MIS 12 and MIS 6 ice coverage in northern central Europe was greatest and nearly similar. These reconstructions are in agreement with high meltwater input into the Bay of Biscay (Toucanne *et al.* 2009a, b). The Fleuve Manche river activity was significantly less during MIS 10 and MIS 8, implying smaller ice sheets (Toucanne *et al.* 2009a, b). The reconstruction of the Fennoscandian ice sheets during these time periods is still highly uncertain, and strongly differs between the estimated minimum and maximum extents (Batchelor *et al.* 2019).

The highest meltwater input during the Saalian glaciation occurred between 160 and 150 ka (Toucanne *et al.* 2009a), corresponding to the retreat of the second Saalian Drenthe (II) ice sheet during MIS 6c. After 150 ka, eustatic sea-level records suggest that ice sheets expanded, with global ice volumes reaching their maximum towards the end of MIS 6 (Elderfield *et al.* 2012), reflecting the growth of the late Illinoian ice sheet in North America (Margari *et al.* 2014). In central Europe, the late Saalian Warthe ice advances were less extensive than the Drenthe ice advances (e.g. Eissmann 2002; Ehlers *et al.* 2011; Böse *et al.* 2012) and no Warthian glacigenic deposits have been recorded so far from the Netherlands (e.g. Laban & van der Meer 2011) and lowland Britain (Gibson & Gibbard 2024). During the Warthe stage (*c.* 150–140 ka, MIS 6b), the southern North Sea was probably ice free and a large amount of meltwater did not flow through the Dover Strait (Toucanne *et al.* 2009a), but drained towards the North Sea, explaining the strong increase in sediment input in the south-eastern North Sea during late MIS 6 (Brendryen *et al.* 2008). However, our dating results and the provenance of till clasts may imply that the Hondsrug ice stream belongs to the Warthian glaciation. Nevertheless, more numerical ages are required to constrain the age of the Hondsrug ice stream. The strong decrease of the Northern Hemisphere summer insolation between 150 and 140 ka could have favoured the re-growth of the Fennoscandian Ice Sheet (Toucanne *et al.* 2009a). The significant Fleuve Manche river activity during MIS 2 correlates with the Last Glacial Maximum (LGM) (Toucanne *et al.* 2009a, b).

Ice advances during the Elsterian glaciation (≥MIS 12). – The estimated single-grain $pIR_{200}IR_{275}$ ages for the assumed Elsterian deposits range from >578 ka to 346±98 ka (Table 4), correlating with >MIS 14 to MIS 8. The sampled glaciolacustrine sediments mainly represent the uppermost fill of tunnel valleys and most probably were deposited during the retreat of the second Elsterian ice advance (e.g. Meyer 1987b; Eissmann 2002; Litt *et al.* 2007), which has been attributed to late MIS 12 (Fig. 2). Comparable age estimates (461±34 to 421±25 ka; pulsed IR_{50} feldspar ages) were published by Roskosch *et al.* (2015) for meltwater deposits from the Leine Valley (Germany) and by Pawley *et al.* (2008) for glaciofluvial sediments from the eastern British Lowlands (494±42 to 391±39 ka; quartz OSL ages), although these age estimates may be less reliable than those determined by more modern methodological approaches. However, the low radioactive isotope concentrations in the eastern British Lowlands allowed to extend the age limit of quartz OSL dating. The form of the dose response curves, pre-heat plateaux tests and dose recovery experiments further indicate that the estimated ages may be reliable (Pawley *et al.* 2008).

Previous age estimates based on feldspar $pIRIR_{290}$ ages of fluvial deposits, overlying the first Elsterian till, also point to an MIS 12 age of the Elsterian deposits (Lauer & Weiss 2018). The older age of the Thurauer Berg succession (>578 ka; sample Th/1; Table 4; Figs 8G, 12) may therefore point to the absence of bleaching caused by subglacial erosion of Neogene sediments and subsequent redeposition in tunnel valleys/glacial lakes. However, we cannot exclude an older or younger than MIS 12 age of the dated tunnel-valley fills.

Ice advances during the early Saalian glaciations (MIS 10 and 8). – Our new single-grain luminescence ages (Table 4) do not provide clear evidence for ice advances during MIS 10 and MIS 8 because the error bars of the estimated ages are too large. It is likely that the MIS 10

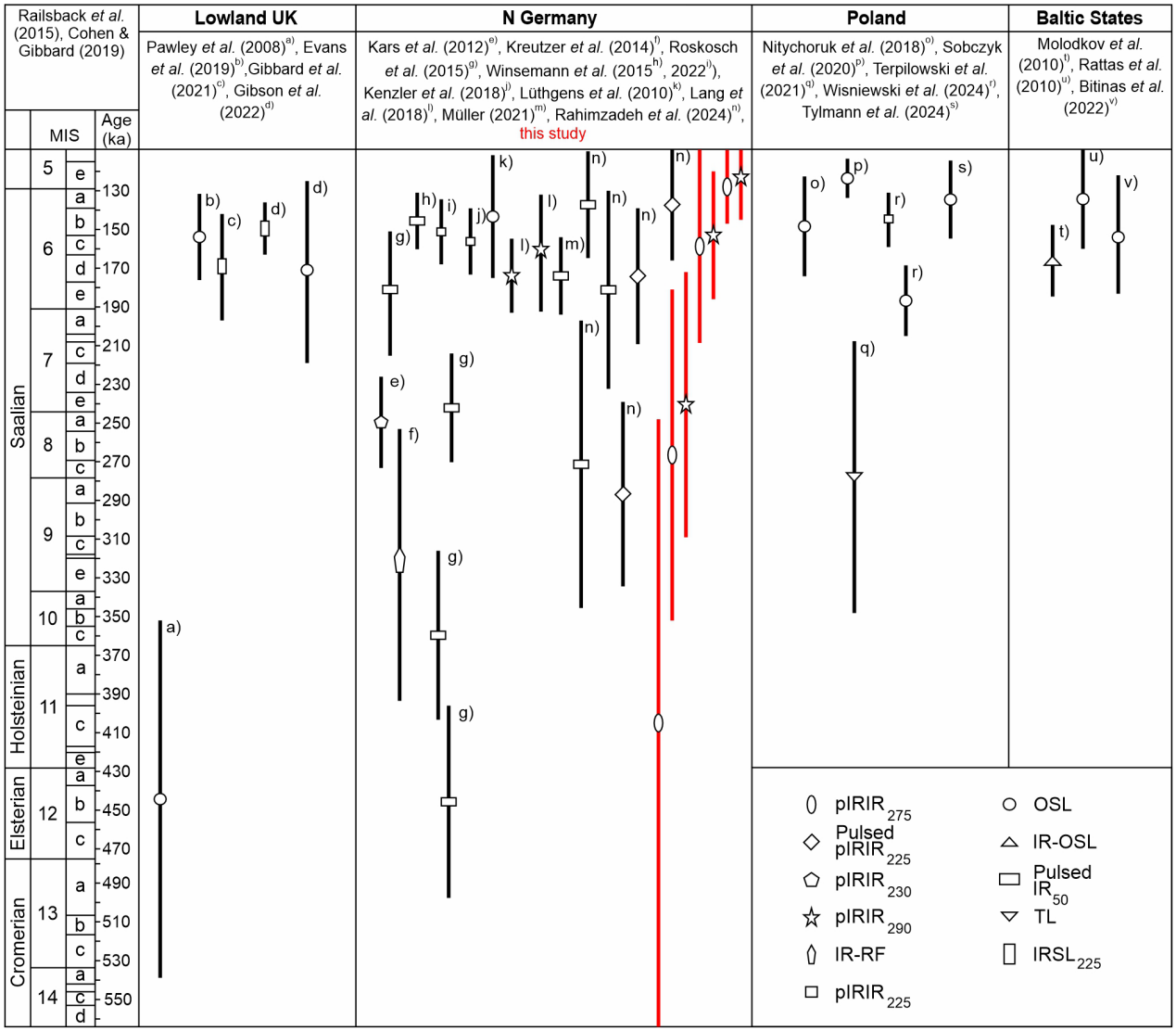

Fig. 15. Compilation of Elsterian and Saalian luminescence ages of meltwater deposits in lowland Britain, northern Germany, Poland, Lithuania and Estonia, compared with the Marine Isotope Stages (MIS) chronology.

and MIS 8 age estimates of previous studies (Kars *et al.* 2012; Kreutzer *et al.* 2014; Roskosch *et al.* 2015), which were based on multiple-grain dating approaches, are overestimated, as is indicated by the comparison of multiple-grain and single-grain feldspar luminescence ages (Tables 4, S3). Furthermore, the dating of fluvial terrace deposits above Elsterian till beds in eastern Germany (Krbetschek *et al.* 2008; Lauer & Weiss 2018) does not provide evidence for an ice advance during MIS 10, which would have reached far into northern Germany.

The southernmost new sample with a potential MIS 8 age was taken from the Porta subaqueous fan and delta complex (259±50 ka; sample Mü-1-16; Table 4, Fig. 14A, C). However, a MIS 8 age of these deposits is probably not very likely as the Porta subaqueous fan and delta complex overlies Saalian fluvial deposits of the Weser Middle Terrace (cf. Winsemann *et al.* 2015). The dated deltaic sediments, which onlap the subaqueous fan, were deposited during forced regression (Winsemann *et al.* 2011, 2018), which was likely associated with poor bleaching of reworked sediments. Further north-east, the upthrusted glaciofluvial deposits of pit 49 (293±59 ka; sample 49/1; Table 4, Fig. 1B) may provide evidence for an MIS 8 ice advance into the north-eastern part of the study area, corresponding to age estimates of glaciolacustrine deposits of the Salzwedel composite ridge system (Rahimzadeh *et al.* 2024). However, the sample shows a high proportion of saturated grains (44%), pointing to poor bleaching. Therefore, we cannot exclude that an MIS 8 (or MIS 10) ice advance may have occurred in the north-easternmost part of the study area (Fig. 15) as has been discussed for the southern North

Sea (Beets *et al*. 2005; Laban & van der Meer 2011) and eastern Poland based on new thermoluminescence ages of meltwater deposits (318±48 to 266±40 ka; Terpiłowski *et al*. 2021).

Ice advances during the late Saalian glaciations (MIS 6). – The best age record is available for the late Saalian Drenthe and Warthe glaciations. Three ice advances into the north-western part of the study area are recorded from the Saalian Drenthe (I, II, III) glaciation, which differ in ice flow direction and clast composition of till beds (e.g. Gundlach & Speetzen 1990; Meyer 2005; Skupin & Zandstra 2010; Lang *et al*. 2018). These ice advances were likely related to ice streaming, indicated by the presence of mega-scale glacial lineations (cf. King *et al*. 2009; Margold *et al*. 2015; Lang *et al*. 2018; Stokes 2018). These Saalian Drenthe ice advances have been previously thought to have occurred during a short time span because the different till beds are partly superimposed without intercalated meltwater deposits (e.g. Klostermann 1992; Meyer 2005). However, luminescence ages of meltwater deposits (Roskosch *et al*. 2015; Winsemann *et al*. 2015, 2022; Lang *et al*. 2018; this study) indicate that the first and the second Saalian Drenthe (I, II) ice advances were probably separated by a longer time period (spanning from late MIS 6d to early MIS 6c) and thus probably corresponding to climate oscillations (cf. Toucanne *et al*. 2009a; Wainer *et al*. 2013). This is supported by soil formation and fluvial erosion after the first ice advance (cf. Lüttig 1960; Junge *et al*. 1999; Eissmann 2002; Lang *et al*. 2018) as well as the denudation of the Bönninghardt glaciotectonic ridge in the lower Rhine Embayment (Klostermann 1986, 1992), which is overlain by younger meltwater deposits (Fig. 5C) that partly may represent GLOF deposits of the Weser and Münsterland Lakes (Winsemann *et al*. 2016).

Global sea-level reconstructions (Elderfield *et al*. 2012) indicate sea-level falls after *c*. 200, 178, 163 and 153 ka. The following sea-level rises at *c*. 173 and 157 ka are probably related to the onset of melting of the first and second Saalian Drenthe (I, II) ice sheets.

The first Saalian Drenthe (I) ice advance into northern Germany probably occurred during MIS 6e to MIS 6d (Figs 1B, 2, 15, Table 4). Related ice-marginal deposits are recorded from the Leine valley (Freden delta, pit 118), the Weser valley (Porta and Coppenbrügge subaqueous fan and delta complex, pits 135, 150, 151) and the Unstrut valley (Zeuchfeld delta, pit 155). These depositional systems formed during maximum ice advance, when the ice-dammed lakes reached their highest lake-levels (cf. Winsemann *et al*. 2011, 2018; Lang *et al*. 2018). The new single-grain luminescence ages range from 259±50 to 209±37 ka (Table 4). These ages match with fading corrected multiple-grain pulsed IR_{50} and pulsed $pIRIR_{225}$ feldspar ages of glaciolacustrine deposits of the Salzwedel composite ridge system (Fig. 8F) which range between 174±35 and 226±29 ka (Rahimzadeh *et al*. 2024). A lower age limit for the maximum extent of the first Saalian Drenthe (I) ice advance is provided by glaciotectonically deformed fluvial deposits of the Leine River, which yielded a pulsed IR_{50} feldspar age of 192±13 ka (Winsemann *et al*. 2015) and organic-rich palustrine and lacustrine deposits in the Weser Valley with ^{230}Th/U ages of 227±9 to 201±15 ka (Waas *et al*. 2011), which are overlain by glaciolacustrine deposits (Winsemann *et al*. 2015). Lauer & Weiss (2018) dated fluvial deposits in eastern Germany, which are partly overlain by the first Saalian Drenthe (I) till. The multiple-grain $pIRIR_{290}$ feldspar ages range between 280±45 and 144±13 ka. If these ages are reliable and the depositional system has been correctly interpreted, the first Saalian ice advance into eastern Germany may have occurred later than in the south-west. However, these ages have not been corrected for fading and therefore might be slightly older, although luminescence signals measured at 290 °C might tend more towards age overestimation if compared to feldspar signals stimulated at lower temperatures.

Age estimates of the first Saalian ice advance from the English West Midlands, which are based on OSL and $pIRSL_{225}$ dating of meltwater deposits cluster at around 200 ka (Fig. 15; Gibbard *et al*. 2021; Gibson *et al*. 2022; Gibson & Gibbard 2024). In Lowland Britain, the main Saalian ice advance occurred some 20 ka later and correlates with MIS 6d (Gibson & Gibbard 2024).

The single-grain feldspar ages of the second Saalian Drenthe (II) ice advance range from 172±38 to 123±18 ka (Table 4, Fig. 15), corresponding to late MIS 6e-5d, although a correlation with late MIS 6c is most likely. Deposits of the second Saalian Drenthe (II) ice advance erosively overly the Porta subaqueous fan and delta complex in the Weser Valley (Fig. 14A, B), implying that the first and second Saalian Drenthe (I, II) ice advances had a quite similar extent in this region (cf. Lang *et al*. 2018). Previous age estimates based on pulsed IR_{50} feldspar dating of the upper Freden delta (161±10 ka; Roskosch *et al*. 2015) and Weser lake-outburst flood deposits (153±7 to 139±8 ka; Winsemann *et al*. 2015), $pIRIR_{225}$ feldspar dating of glaciolacustrine fan and delta deposits of the Elbe Lake (157±8 to 144±9 ka; Winsemann *et al*. 2022) and $pIRIR_{290}$ ages of glaciolacustrine delta deposits of the Weser, Saale-Unstrut and Halle-Leipzig lakes (175±10 to 156±24 ka; Lang *et al*. 2018) are in the same range (Fig. 15). The very young age obtained for meltwater deposits of the Rehburg line near Eilvese (123±18 ka, sample Eil-1, pit 91; Table 4, Figs 1B, 4A, H) probably underestimates the age of deposition.

Lower age limits for the second Saalian Drenthe (II) ice advance are provided by OSL ages of fluvial deposits of the Rhine-Maas system near Utrecht in the central

Netherlands (168±19 ka; Busschers *et al*. 2008). A younger fluvial unit from the central Netherlands, which was deposited south of the ice margin, yielded OSL ages of 149±13 to 137±11 ka and is interpreted to pass laterally into glaciofluvial deposits of the second Saalian Drenthe ice advance (Busschers *et al*. 2008). Age estimates of the second Saalian ice advance from the English West Midlands, which are based on OSL and $pIRSL_{225}$ dating of meltwater deposits, cluster at around 147±3 ka (Gibson *et al*. 2022; Gibson & Gibbard 2024). Quartz ages of meltwater deposits in the lowlands of eastern England range from 165±11 to 141±9.4 ka (Evans *et al*. 2019). These ages correspond with a $pIRIR_{225}$ age of meltwater deposits in southern Poland (145±14 ka; Wiśniewski *et al*. 2024) and IR-OSL ages of till and meltwater deposits from the Lithuanian Baltic Sea coast (173±11.5 to 158±10.4 ka; Molodkov *et al*. 2010) (Fig. 15). The single-grain feldspar dating of meltwater deposits of the third Saalian Drenthe (III) ice advance (referred to as Hondsrug ice-stream in the westernmost part of the study area) gave an age of 123±22 ka (Table 4, Figs 1B, 5). Based on the composition of the red till with a high proportion of clasts derived from Fennoscandia (Skupin & Zandstra 2010) and the age estimate, the Hondsrug ice stream may alternatively belong to the Warthian glaciation. However, more single-grain luminescence ages are required for a robust correlation.

Because of the assumed lesser extent of the Saalian Warthe ice sheet (Fig. 1B), meltwater deposits are sparse in the study area. Meltwater deposits with a potential Warthian age (sample 42/1; 128±19 ka) are exposed south of the Lamstedt composite ridge system (Figs 1A, 7A, Table 4). Luminescence dating of the Lichtenberg core (Fig. 8G) gave pulsed IR_{50} ages ranging from 155±14 to 122±14 ka and pulsed $pIRIR_{225}$ ages ranging from 146±20 to 123±12 ka (Rahimzadeh *et al*. 2024). Applying a Bacon-age depth model to 55 individual luminescence ages from 24 samples (quartz OSL, fading corrected pulsed IR_{50} and fading corrected pulsed $pIRIR_{225}$ on 24 samples) produces posterior ages of ~148–127 ka for the Saalian Drenthe II/Warthe deposits, coherently integrating the individual age likelihoods and stratigraphic order and thereby yielding a narrower, stratigraphically consistent age range than the raw spread of individual ages. Previous dating of Warthian meltwater deposits (Fig. 15) in north-eastern Germany gave OSL and $pIRIR_{225}$ ages between 155±21 and 130±17 ka (Lüthgens *et al*. 2010; Kenzler *et al*. 2018), corresponding to OSL quartz ages of Warthian meltwater deposits in Poland (160±14 to 132.5±9.9 ka, Nitychoruk *et al*. 2018; 123.6±10.1 ka, Sobczyk *et al*. 2020; 148.9±7.2 to 126.8±11 ka, Tylmann *et al*. 2024). Glaciolacustrine sediments from the Lithuanian Baltic Sea coast have OSL ages of 164±19 to 134±12 ka (Bitinas *et al*. 2022) and OSL ages of glaciolacustrine deposits in south-western Estonia range from 151±9 to 117± 9 ka (Rattas *et al*. 2010).

Implications for the age of the glaciotectonic complexes and related ice-marginal positions

The large composite ridge systems usually contain pre-Pleistocene sediments and bedrock such as the Rehburg line and the Lamstedt system (Figs 1A, 4H, 5B, C, 7C), whereas the Altenwalde and Salzwedel composite ridge systems are mainly composed of unconsolidated Middle Pleistocene sediments (Figs 6F, 8G). However, the reconstruction of the internal architecture of the composite ridge systems is hampered by the number and quality of outcrops and borehole data, often lacking reliable stratigraphic assignments and numerical age control. Therefore, uncertainties remain.

The Rehburg line is the oldest glaciotectonic complex and initially formed during the first Saalian Drenthe (I) ice advance that approached from a northerly direction. This glaciotectonic complex has been overprinted by the second Saalian Drenthe (II) and partly also by the third Saalian Drenthe (III; Hondsrug ice stream) ice advances (Figs 4H, 5B, C), approaching from the north-east and north-west leading to erosion and/or steepening of the oldest ridges (e.g. Klostermann 1986, 1992; van der Wateren 1987; Skupin & Zandstra 2010).

The formation of the glaciotectonic complexes further north and north-east is less well understood and has previously been related to the second Saalian Drenthe (II) and Warthe ice advances, as the first Saalian Drenthe till (I) forms part of the internal thrusts (Sindowski 1965; Höfle & Lade 1983; van Gijssel 1987). After thrusting, the Lamstedt composite ridge system was overridden by the second Saalian Drenthe (II) ice sheet (Höfle & Lade 1983; van Gijssel 1987). Apparently, the Altenwalde composite ridge system was not overridden by the second Drenthe (II) ice sheet and may correspond to an ice-marginal position mapped in the southern North Sea (Fig. 1A; Lohrberg *et al*. 2020; Winsemann *et al*. 2020), which may indicate a younger re-advance of the second Saalian Drenthe (II) ice sheet. Undeformed glaciofluvial deposits south-east of the Altenwalde composite ridge system are 150±30 ka old (sample 12/2; Table 4, Fig. 6A, B, pit 12, log 12) corresponding with the luminescence ages of meltwater deposits of the second Drenthe (II) ice advance further south (Table 4; Winsemann *et al*. 2015, 2022; Lang *et al*. 2018). The Lamstedt composite ridge system may then be slightly older and represent an ice-marginal position further east during re-advance. Undeformed glaciofluvial deposits south of the Lamstedt composite ridge system are 128±19 ka old (sample 42/1; Table 4, Fig. 7A, B, pit 42, log 42) and may therefore be related to the subsequent Warthe ice advance.

The extensive size of the Salzwedel composite ridge system with an arcuate suite of subparallel ridges and intervening depressions, in which glacial lakes formed (Fig. 8D, G), points to a multiphase development during overall ice-margin retreat, including phases of re-advances, still-stands and rapid retreats (cf. Aber

et al. 1989; Lee *et al*. 2013). The curved shape of the ridge system probably conforms to the general shape of the second Saalian Drenthe (II) ice lobe that produced them. Individual ridge crests probably correspond to the crests of thrust sheets and overlying syntectonic meltwater sediments. During the subsequent Warthe ice advance, renewed thrusting occurred in the eastermost part of the composite ridge system.

The detachments of the composite ridges in which the thrust faults sole were probably controlled by the rheological contrasts between sandy meltwater deposits and the underlying fine-grained Lauenburg Clay Complex or Holsteinian clay, which commonly represent the uppermost tunnel-valley fills and their marginal areas. Partly, the detachment is located in older fine-grained marine Neogene, Palaeogene and Cretaceous sediments/sedimentary rocks (Figs 4, 5, 7). Higher porewater pressure and porewater flow in proglacial sediments reduce shear strength, weaken an already incompetent zone and thus become of great importance in the initial development of a detachment surface (Andersen *et al*. 2005). Therefore, the detachments of the described glaciotectonic complexes probably preferentially formed in overpressurized clays of different ages, which became further weakened by increasing porewater pressure under the load of the advancing ice sheets (e.g. Lee *et al*. 2013; Vaughan-Hirsch & Phillips 2017; Winsemann *et al*. 2020). An important finding is that the depths of the detachment surfaces seem to be controlled by the presence of tunnel-valley fills. In the northern part of the study area, smaller composite ridge systems formed, where the basal detachment is shallow (20–60 m below surface) and likely controlled by the Lauenburg Clay Complex of the uppermost tunnel-valley fills, whereas the larger composite ridge system of the Rehburg line further south and south-west partly has a much deeper detachment surface (>100 m; cf. van den Berg & Beets 1987; Hahne *et al*. 1994). We cannot exclude that the base of the permafrost or another kind of rheological boundary within the frozen sediment in the glacier foreland played a role in the location of the basal detachment surfaces. An impermeable permafrost ground can lead to the formation of a zone of high pore-water pressure at the base of the frozen sediment (e.g. Boulton *et al*. 1999) and thus cause differences in cohesive strength and mechanical properties (e.g. Astakhov *et al*. 1996; Etzelmüller *et al*. 1996; Andersen *et al*. 2005; Lee *et al*. 2013; Vaughan-Hirsch & Phillips 2017; Winsemann *et al*. 2020). The depths of the detachments may partly correspond to the modelled depth of permafrost (Graßmann *et al*. 2010) for the Saalian glaciation (~50 to 100 m), which is based on a calibrated basal heat flow of 50 mW m^{-2} (Graßmann *et al*. 2005).

Conclusions

Despite the use of a single-grain dating approach, it remains challenging to correlate the Middle Pleistocene ice advances with marine isotope stages or even marine isotope substages due to the large uncertainties of estimated ages. These uncertainties are mainly related to the high natural signal intensities of the studied samples, which fall within the non-linear part of the DRC. In this region of the DRC, even small uncertainties in the natural signal intensity are magnified by interpolation, leading to potentially unbounded uncertainties in the D_e estimates.

The age estimates for the Elsterian glacigenic deposits range from >578 to 348±98 ka, correlating with >MIS 14 to MIS 8, although an MIS 12 age is most likely. The sampled subaqueous fan and delta sediments were deposited in underfilled tunnel valleys, probably during retreat of the second Elsterian ice sheet. They consist of fine- to medium-grained whitish sands with reworked lignite from underlying Neogene and Palaeogene shallow-marine deposits. The partly very old luminescence ages therefore may point to an absence of bleaching caused by subglacial erosion of older sediments and subsequent re-deposition in tunnel valleys and/or glacial lakes. However, we cannot exclude a partly younger (MIS 10 or MIS 8) age of the dated uppermost tunnel-valley fills.

The correlation of the Saalian Drenthe and Warthe ice advances with MIS 6 is well constrained. Based on the new single-grain luminescence ages and regional lithostratigraphic data, we tentatively attribute the first Saalian Drenthe (I) ice advance to MIS 6e-d. After a longer phase of ice-sheet retreat, fluvial erosion and soil formation, the second Saalian Drenthe (II) ice advance probably occurred during late MIS 6c, matching with data from England, Poland and Lithuania. Both ice advances reached far into northern Germany and had approximately the same extent. In the northern part of the study area, glaciofluvial fans and larger glaciofluvial distributive systems formed along the advancing/retreating ice sheets. These sand-rich glaciofluvial systems are commonly characterized by tabular sandy sheetflood deposits, alternating with coarser-grained single-storey, multilateral or multistorey channel bodies. During the maximum extent of the first and second Saalian Drenthe (I, II) ice sheets, large ice-dammed lakes formed, which catastrophically drained during ice-margin retreat. The third Saalian Drenthe (III; Hondsrug ice stream) and Warthe ice advances probably correlate with MIS 6b-a. The Hondsrug ice stream may therefore belong to the Warthe ice advance, as supported by the occurrence of red till with Fennoscandian provenance. However, more single-grain dating is required for a robust correlation. The glaciotectonic complexes partly have a multiphase development related to the different Saalian ice advances. Smaller composite ridge systems with shallow detachments evolved in areas with tunnel-valley fills, probably controlled by the rheological contrasts between sandy meltwater deposits and underlying fine-grained deposits of the uppermost Elsterian tunnel-valley fills (Lauenburg Clay Complex) and/or

Neogene marine deposits of their marginal areas. In contrast, larger glaciotectonic complexes with deep detachments formed further south ('Rehburg line') where large tunnel valleys are absent.

Acknowledgements. – This research was financed by the Lower Saxony MWK with funds from the *zukunft.niedersachsen* program of the VolkswagenStiftung, grant number ZN3985. We thank two anonymous reviewers for constructive comments, which helped to improve the manuscript as well as Gianpiero Di Maida and Jan A. Piotrowski for the editorial handling of the manuscript. The hill-shaded relief maps were produced using Copernicus data, information funded by the European Union (EU-DEM layers) and data from the Landesamt für Geoinformation und Landesvermessung Niedersachsen (LGLN). We thank LBEG (Niedersächsisches Landesamt für Bergbau, Energie und Geologie) for providing borehole data and LAGB (Landesamt für Geologie und Bergwesen Sachsen-Anhalt) for providing borehole data and lithofacies maps. We thank S. Mogwitz, P. Posimowski, S. Riemenschneider and S. Hesse for sample preparation and technical support in the luminescence laboratory, Tim Hartmann, Malte Hoffmann, Jörg Lang, Katharina Müller and Klaus Skupin for help with fieldwork and discussion. Many thanks are also due to the owners of the open-pits for permitting us to work on their properties.

Author contributions. – NS: Fieldwork, analysis of borehole data, visualization, writing and editing. NR: Methodology, luminescence dating, visualization, writing and editing. DC: Methodology, luminescence dating, visualization, writing and editing. FM: Fieldwork and visualization. TL: Funding acquisition, methodology, luminescence dating, writing and editing. WS-B: Visualization and editing. YS: Fieldwork and editing. CB: Fieldwork, visualization, writing and editing. RF: Analysis of borehole data, visualization and editing. ST: Funding acquisition, methodology, luminescence dating, writing and editing. JW: Funding acquisition, conceptualization, methodology, fieldwork, visualization, writing and editing.

Data availability statement. – All data are available through this publication.

References

Aber, J. S., Croot, D. G. & Fenton, M. M. 1989: *Glaciotectonic Landforms and Structures*. 200 pp. Kluwer, Dordrecht.

Alexander, J., Bridge, J. S., Cheel, R. J. & Leclair, S. F. 2001: Bedforms and associated sedimentary structures formed under supercritical water flows over aggrading sand beds. *Sedimentology 48*, 133–152. https://doi.org/10.1046/j.1365-3091.2001.00357.x.

Alexanderson, H. & Murray, A. S. 2012: Problems and potential of OSL dating Weichselian and Holocene sediments in Sweden. *Quaternary Science Reviews 44*, 37–50. https://doi.org/10.1016/j.quascirev.2009.09.020.

Allen, J. R. L. 1984: Sedimentary structures: their character and physical basis. *Developments in Sedimentology 30*, 1–663.

Andersen, L. T., Hansen, D. L. & Huuse, M. 2005: Numerical modelling of thrust structures in unconsolidated sediments: implications for glaciotectonic deformation. *Journal of Structural Geology 27*, 587–596. https://doi.org/10.1016/j.jsg.2005.01.005.

Ashley, G. M., Southard, J. B. & Boothroyd, J. C. 1982: Deposition of climbing-ripple beds: a flume simulation. *Sedimentology 29*, 67–79. https://doi.org/10.1111/j.1365-3091.1982.tb01709.x.

Astakhov, V. I., Kaplyanskaya, F. A. & Tarnogradsky, V. D. 1996: Pleistocene permafrost of West Siberia as a deformable glacier bed. *Permafrost and Periglacial Processes 7*, 165–191. https://doi.org/10.1002/(SICI)1099-1530(199604)7:2<165::AID-PPP218>3.0.CO;2-S.

Auclair, M., Lamothe, M. & Huot, S. 2003: Measurement of anomalous fading for feldspar IRSL using SAR. *Radiation Measurements 37*, 487–492. https://doi.org/10.1016/S1350-4487(03)00018-0.

Batchelor, C. L., Margold, M., Krapp, M., Murton, D. K., Dalton, A. S., Gibbard, P. L., Stokes, C. R., Murton, J. B. & Manica, A. 2019: The configuration of Northern Hemisphere ice sheets through the Quaternary. *Nature Communications 10*, 3713. https://doi.org/10.1038/s41467-019-11601-2.

Beets, D. J., Meijer, T., Beets, C. J., Cleveringa, P., Laban, C. & Van der Spek, A. J. F. 2005: Evidence for a Middle Pleistocene glaciation of MIS 8 age in the southern North Sea. *Quaternary International 133*, 7–19. https://doi.org/10.1016/j.quaint.2004.10.002.

Benn, D. I. & Evans, D. J. A. 2010: *Glaciers and Glaciation*. 802 pp. Hodder Education, London.

van den Berg, M. W. & Beets, D. J. 1987: Saalian glacial deposits and morphology in the Netherlands. *In* Van der Meer, J. J. M. (ed.): *Tills and Glaciotectonics*, 235–251. Balkema, Rotterdam.

Bitinas, A., Molodkov, A., Damušytė, A., Grigienė, A., Satkūnas, J., Šeirienė, V. & Šlauteris, A. 2022: Reconstruction of the geological history of the Lithuanian Maritime Region from MIS 6 to MIS 3. *Quaternary International 617*, 4–20. https://doi.org/10.1016/j.quaint.2021.05.014.

Blair, T. C. 1999: Sedimentary processes and facies of the waterlaid Anvil Spring Canyon alluvial fan, Death Valley, California. *Sedimentology 46*, 913–940. https://doi.org/10.1046/j.1365-3091.1999.00259.x.

Blair, T. C. & McPherson, J. G. 2009: Processes and forms of alluvial fans. *In* Parsons, A. & Abrahams, A. (eds.): *Geomorphology of Desert Environments*, 413–467. Springer, Dordrecht.

Böse, M., Lüthgens, C., Lee, J. R. & Rose, J. 2012: Quaternary glaciations of northern Europe. *Quaternary Science Reviews 44*, 1–25. https://doi.org/10.1016/j.quascirev.2012.04.017.

Boulton, G. S., van der Meer, J. J. M., Beets, D. J., Hart, J. K. & Ruegg, G. H. J. 1999: The sedimentary and structural evolution of a recent push moraine complex: Holmstrømbreen, Spitsbergen. *Quaternary Science Reviews 18*, 339–371. https://doi.org/10.1016/S0277-3791(98)00068-7.

Brendryen, J., Grasmo, K., Haflidason, H., Zuhlsdorff, C. & Sejrup, H. P. 2008: Ocean–ice-sheet interaction and tephrastratigraphy from the SE Nordic seas region between 50–150 ka. *Geophysical Research Abstracts EGU2008-A-09844*. EGU General Assembly 2008, Vienna, Austria.

Breuer, S., Bebiolka, A., Noack, V. & Lang, J. 2023: The past is the key to the future – considering Pleistocene subglacial erosion for the minimum depth of a radioactive waste repository. *E&G Quaternary Science Journal 72*, 113–125. https://doi.org/10.5194/egqsj-72-113-2023.

Buechi, M. W., Landgraf, A., Madritsch, H., Mueller, D., Knipping, M., Nyffenegger, F., Preusser, F., Schaller, S., Schnellmann, M. & Deplazes, G. 2024: Terminal glacial overdeepenings: patterns of erosion, infilling and new constraints on the glaciation history of Northern Switzerland. *Quaternary Science Reviews 344*, 108970. https://doi.org/10.1016/j.quascirev.2024.108970.

Burchardt, I. 1993: *Lithofazieskarten Quartär, Blatt 2063 Gardelegen*. Geologisches Landesamt Sachsen-Anhalt, Halle.

Busschers, F. S., Van Balen, R. T., Cohen, K. M., Kasse, C., Weerts, H. J. T., Wallinga, J. & Bunnik, F. P. M. 2008: Response of the Rhine-Meuse fluvial system to Saalian ice-sheet dynamics. *Boreas 37*, 377–398. https://doi.org/10.1111/j.1502-3885.2008.00025.x.

Cartigny, M. J. B., Eggenhuisen, J. T., Hansen, E. W. M. & Postma, G. 2013: Concentration-dependent flow stratification in experimental high-density turbidity currents and their relevance to turbidite facies models. *Journal of Sedimentary Research 83*, 1047–1065. https://doi.org/10.2110/jsr.2013.71.

Cartigny, M. J. B., Ventra, D., Postma, G. & van den Berg, J. H. 2014: Morphodynamics and sedimentary structures of bedforms under supercritical-flow conditions: new insights from flume experiments. *Sedimentology 61*, 712–748. https://doi.org/10.1111/sed.12076.

Caspers, G., Jordan, H., Merkt, J., Meyer, K.-D., Müller, H. & Streif, H. 1995: Niedersachsen. *In* Benda, L. (ed.): *Das Quartär Deutschlands*, 23–58. Bornträger, Berlin.

Cohen, K. M. & Gibbard, P. L. 2019: Global chronostratigraphical table for the last 2.7 million years, version 2019 QI-500. *Quaternary International 500*, 20–31. https://doi.org/10.1016/j.quaint.2019.03.009.

Coughlan, M., Fleischer, M., Wheeler, A. J., Hepp, D. A., Hebbeln, D. & Mörz, T. 2018: A revised stratigraphical framework for the Quaternary deposits of the German North Sea sector: a geological-geotechnical approach. *Boreas 47*, 80–105. https://doi.org/10.1111/bor.12253.

van Dijk, M., Postma, G. & Kleinhans, M. G. 2009: Autocyclic behaviour of fan deltas: an analogue experimental study. *Sedimentology 56*, 1569–1589. https://doi.org/10.1111/j.1365-3091.2008.01047.x.

Duller, G. A. T. 2012: Improving the accuracy and precision of equivalent doses determined using the optically stimulated luminescence signal from single grains of quartz. *Radiation Measurements 47*, 770–777. https://doi.org/10.1016/j.radmeas.2012.01.006.

Duller, R. A., Mountney, N. P., Russell, A. J. & Cassidy, N. C. 2008: Architectural analysis of a volcaniclastic jökulhlaup deposit, southern Iceland: sedimentary evidence for supercritical flow. *Sedimentology 55*, 939–964. https://doi.org/10.1111/j.1365-3091.2007.00931.x.

Ehlers, J., Grube, A., Stephan, H. J. & Wansa, S. 2011: Pleistocene glaciations of North Germany – new results. *In* Ehlers, J., Gibbard, P. L. & Hughes, P. D. (eds.): *Quaternary Glaciations – Extent and Chronology – A Closer Look. Developments in Quaternary Sciences 15*, 149–162. Elsevier, Amsterdam. https://doi.org/10.1016/B978-0-444-53447-7.00013-1.

Eissmann, L. 2002: Quaternary geology of eastern Germany (Saxony, Saxon–Anhalt, South Brandenburg, Thüringia), type area of the Elsterian and Saalian Stages in Europe. *Quaternary Science Reviews 21*, 1275–1346. https://doi.org/10.1016/S0277-3791(01)00075-0.

Elderfield, H., Ferretti, P., Greaves, M., Crowhurst, S., McCave, I. N., Hodell, D. & Piotrowski, A. M. 2012: Evolution of ocean temperature and ice volume through the mid-Pleistocene climate transition. *Science 337*, 704–709. https://doi.org/10.1126/science.1221294.

Etzelmüller, B., Hagen, J. O., Vatne, G., Ødegård, R. S. & Sollid, J. L. 1996: Glacier debris accumulation and sediment deformation influenced by permafrost: examples from Svalbard. *Annals of Glaciology 22*, 53–62. https://doi.org/10.3189/1996AoG22-1-53-62.

Evans, D. J. A., Roberts, D. H., Bateman, M. D., Ely, J., Medialdea, A., Burke, M. J., Chiverrell, R. C., Clark, C. D. & Fabel, D. 2019: A chronology for North Sea lobe advance and recession on the Lincolnshire and Norfolk coasts during MIS 2 and 6. *Proceedings of the Geologists' Association 130*, 523–540. https://doi.org/10.1016/j.pgeola.2018.10.004.

Fälber, R., Jungdal-Olesen, G., Pedersen, V. K., Damsgaard, A., Piotrowski, J. A., Brandes, C. & Winsemann, J. 2025: Construction of hydrostratigraphic subsurface models of the Northwest German Basin: input for numerical simulation of subglacial erosion during past and future glaciations. *Abstract, EGU General Assembly 2025, Vienna, Austria, 27 April–2 May 2025, EGU25-1788*. https://doi.org/10.5194/egusphere-egu25-1788.

Fielding, C. R. 2006: Upper flow regime sheets, lenses and scour fills: extending the range of architectural elements for fluvial sediment bodies. *Sedimentary Geology 190*, 227–240. https://doi.org/10.1016/j.sedgeo.2006.05.009.

Fielding, C. R., Allen, J. P., Alexander, J. & Gibling, M. R. 2009: Facies model for fluvial systems in the seasonal tropics and subtropics. *Geology 37*, 623–626. https://doi.org/10.1130/G25727A.1.

Fuchs, M. & Owen, L. A. 2008: Luminescence dating of glacial and associated sediments: review, recommendations and future direction. *Boreas 37*, 636–659. https://doi.org/10.1111/j.1502-3885.2008.00052.x.

Galbraith, R. F., Roberts, R. G., Laslett, G. M., Yoshida, H. & Olley, J. M. 1999: Optical dating of single and multiple grains of quartz from Jinmium Rock Shelter, northern Australia: part I, experimental design and statistical models. *Archaeometry 41*, 339–364. https://doi.org/10.1111/j.1475-4754.1999.tb00987.x.

Gibbard, P. L., Bateman, M. D., Leathard, J. & West, R. G. 2021: Luminescence dating of a late middle Pleistocene glacial advance in eastern England. *Netherlands Journal of Geosciences 100*, e18. https://doi.org/10.1017/njg.2021.13.

Gibling, M. R. 2006: Width and thickness of fluvial channel bodies and valley fills in the geological record: a literate compilation and classification. *Journal of Sedimentary Research 76*, 731–770. https://doi.org/10.2110/jsr.2006.060.

Gibson, S. M. & Gibbard, P. L. 2024: Late Middle Pleistocene Wolstonian Stage (MIS 6) glaciation in lowland Britain and its North Sea regional equivalents – a review. *Boreas 53*, 543–561. https://doi.org/10.1111/bor.12674.

Gibson, S. M., Bateman, M. D., Murton, J. B., Barrows, T. T., Fifield, L. K. & Gibbard, P. L. 2022: Timing and dynamics of Late Wolstonian Substage 'Moreton Stadial' (MIS 6) glaciation in the English West Midlands, UK. *Royal Society Open Science 9*, 220312. https://doi.org/10.1098/rsos.220312.

van Gijssel, K. 1987: A lithostratigraphic and glaciotectonic reconstruction of the Lamstedt moraine, Lower Saxony (Frg). *In* van der Meer, J. J. M. (ed.): *Tills and Glaciotectonics*, 145–155. Balkema, Rotterdam.

Gorrell, G. & Shaw, J. 1991: Deposition in an esker, bead and fan complex, Lanark, Ontario, Canada. *Sedimentary Geology 72*, 285–314. https://doi.org/10.1016/0037-0738(91)90016-7.

Graßmann, S., Cramer, B., Delisle, G., Hantschel, T., Messner, J. & Winsemann, J. 2010: pT-effects of Pleistocene glacial periods on permafrost, gas hydrate stability zones and reservoir of the Mittelplate oil field, northern Germany. *Marine and Petroleum Geology 27*, 298–306. https://doi.org/10.1016/j.marpetgeo.2009.08.002.

Graßmann, S., Cramer, B., Delisle, G., Messner, J. & Winsemann, J. 2005: Geological history and petroleum system of the Mittelplate oil field, Northern Germany. *International Journal of Earth Sciences 94*, 979–989. https://doi.org/10.1007/s00531-005-0018-x.

Grinat, M., Günther, T., Igel, J. & Müller-Petke, M. 2021: *Geophysical investigations at the GE2 pilot area using ERT, electromagnetics and ground-penetrating radar. Result Report, Project: Interreg VB NSR: Topsoil*. 14 pp. Leibniz-Institut für Angewandte Geophysik, Hannover.

Grube, F. 2015: Saale-Komplex in der Hamburger Region. *Verhandlungen Naturwissenschaftlicher Verein Hamburg 49*, 99–154.

Gundlach, J. & Speetzen, E. 1990: Untersuchungen zur Petrographie und Genese der drenthestadialen Grundmoräne im Westmünsterland (Westfälische Bucht, NW-Deutschland). *Neues Jahrbuch für Geologie und Paläontologie-Abhandlungen 181*, 471–499.

Guo, Y., Li, B. & Zhao, H. 2020: Comparison of single-aliquot and single-grain MET-pIRIR D_e-results for potassium feldspar samples from the Nihewan Basin, northern China. *Quaternary Geochronology 56*, 101040. https://doi.org/10.1016/j.quageo.2019.101040.

Hahne, J., Kemle, S. & Merkt, J. 1994: Eem-, weichsel- und saalezeitliche Ablagerungen der Bohrung "Quakenbrück GE 2". *In* Meyer, K.-D. (ed.): *Neuere Untersuchungen an Interglazialen in Niedersachsen*, 9–69. *Geologisches Jahrbuch, Reihe A, Band A 134*.

Hamilton, P., Gaillot, G., Strom, K., Fedele, J. & Hoyal, D. C. 2017: Linking hydraulic properties in supercritical submarine distributary channels to depositional-lobe geometry. *Journal of Sedimentary Research 87*, 935–950. https://doi.org/10.2110/jsr.2017.53.

Hamilton, P. B., Strom, K. & Hoyal, D. C. J. D. 2013: Autogenic incision-backfilling cycles and lobe formation during the growth of alluvial fans with supercritical distributaries. *Sedimentology 60*, 1498–1525. https://doi.org/10.1111/sed.12046.

Hamilton, P. B., Strom, K. B. & Hoyal, D. C. J. D. 2015: Hydraulic and sediment transport properties of autogenic avulsion cycles on submarine fans with supercritical distributaries. *Journal of Geophysical Research: Earth Surface 120*, 1369–1389. https://doi.org/10.1002/2014JF003414.

Hein, M., Urban, B., Tanner, D. C., Buness, A. H., Tucci, M., Hoelzmann, P., Dietel, S., Kaniecki, M., Schultz, J., Kasper, T., von Suchodoletz, H., Schwalb, A., Weiss, M. & Lauer, T. 2021: Eemian landscape response to climatic shifts and evidence for northerly Neanderthal occupation at a palaeolake margin in northern Germany. *Earth Surface Processes and Landforms 46*, 2884–2901. https://doi.org/10.1002/esp.5219.

Höfle, H. C. & Lade, U. 1983: The stratigraphic position of the Lamstedter moraine within the younger Drenthe substage (middle Saalian). *In* Ehlers, J. (ed.): *Glacial Deposits in North-West Europe*, 343–346. Balkema, Rotterdam.

Hofstra, M., Hodgson, D. M., Peakall, J. & Flint, S. S. 2015: Giant scour-fills in ancient channel-lobe transition zones: formative processes and depositional architecture. *Sedimentary Geology 329*, 98–114. https://doi.org/10.1016/j.sedgeo.2015.09.004.

Hornung, J. J., Asprion, U. & Winsemann, J. 2007: Jet-efflux deposits of a subaqueous ice-contact fan, glacial lake Rinteln, northwestern Germany. *Sedimentary Geology 193*, 167–192. https://doi.org/10.1016/j.sedgeo.2005.11.024.

Huerta, P., Armenteros, I. & Silva, P. G. 2011: Large-scale architecture in non-marine basins: the response to the interplay between accommodation space and sediment supply. *Sedimentology 58*, 1716–1736. https://doi.org/10.1111/j.1365-3091.2011.01231.x.

Huntley, D. J. & Baril, M. R. 1997: The K content of the K-feldspars being measured in optical dating or in thermoluminescence dating. *Ancient TL 15*, 11–13. https://doi.org/10.26034/la.atl.1997.271.

Ites, R. 1996: Lagerungsverhältnisse und Schichtaufbau in Quartäraufschlüssen der östlichen Brelinger Berge (N Hannover). *Mitteilungen aus dem Geologischen Institut der Universität Hannover 36*, 1–99.

Jacobs, Z., Li, B., Shunkov, M. V., Kozlikin, M. B., Bolikhovskaya, N. S., Agadjanian, A. K., Uliyanov, V. A., Vasiliev, S. K., O'Gorman, K., Derevianko, A. P. & Roberts, R. G. 2019: Timing of archaic hominin occupation of Denisova Cave in southern Siberia. *Nature 565*, 594–599. https://doi.org/10.1038/s41586-018-0843-2.

Janszen, A., Moreau, J., Moscariello, A., Ehlers, J. & Kröger, J. 2013: Time transgressive tunnel-valley infill revealed by a three-dimensional sedimentary model, Hamburg, north-west Germany. *Sedimentology 60*, 693–719. https://doi.org/10.1111/j.1365-3091.2012.01357.x.

Jordan, H. 1979: *Geologische Karte von Niedersachsen 1:25000. Erläuterungen zu Blatt Nr. 3521 Rehburg*. 134 pp. Niedersächsisches Landesamt für Bodenforschung, Hannover.

Jordan, H. 1980: *Geologische Karte von Niedersachsen 1:25000. Erläuterungen zu Blatt Nr. 3422 Neustadt am Rübenberge*. 88 pp. Niedersächsisches Landesamt für Bodenforschung, Hannover.

Junge, F. W. 1998: Die Bändertone Mitteldeutschlands und angrenzender Gebiete. *Altenburger naturwissenschaftliche Forschungen 9*, 1–210.

Junge, F. W., Böttger, T. & Siegert, C. 1999: Die Stauseesedimente des Bruckdorfer Horizontes: Ergebnis der Eisrandoszillation des saaleglazialen skandinavischen Inlandeises in Mitteldeutschland. *Mauritiana 17*, 257–276.

Kalińska, E., Weckwerth, P., Alexanderson, H., Piotrowski, J. A. & Wysota, W. 2025: OSL dating of glacial outburst flood deposits in NE Poland and their bleaching problem inferred from the landform-sediment associations and regional context. *Quaternary Research 124*, 26–46. https://doi.org/10.1017/qua.2024.50.

Kars, R. H., Busschers, F. S. & Wallinga, J. 2012: Validating post IR-IRSL dating on K-feldspars through comparison with quartz OSL ages. *Quaternary Geochronology 12*, 74–86. https://doi.org/10.1016/j.quageo.2012.05.001.

Kars, R. H., Wallinga, J. & Cohen, K. M. 2008: A new approach towards anomalous fading correction for feldspar IRSL dating – tests on samples in field saturation. *Radiation Measurements 43*, 786–790. https://doi.org/10.1016/j.radmeas.2008.01.021.

Kenzler, M., Rother, H., Hüneke, H., Frenzel, P., Strahl, J., Tsukamoto, S., Li, Y., Meng, S., Gallas, J. & Frechen, M. 2018: A multi-proxy palaeoenvironmental and geochronological reconstruction of the Saalian-Eemian-Weichselian succession at Klein Klütz Höved, NE Germany. *Boreas 47*, 114–136. https://doi.org/10.1111/bor.12255.

King, E. C., Hindmarsh, R. C. A. & Stokes, C. R. 2009: Formation of mega-scale glacial lineations observed beneath a West Antarctic ice stream. *Nature Geoscience 2*, 585–588. https://doi.org/10.1038/ngeo581.

King, G. E., Sanderson, D. C. W., Robinson, R. A. J. & Finch, A. A. 2014: Understanding process of sediment bleaching in glacial settings using a portable OSL reader. *Boreas 43*, 955–972. https://doi.org/10.1111/bor.12078.

Kjær, K. H., Sultan, L., Krüger, J. & Schomacker, A. 2004: Architecture and sedimentation of outwash fans in front of the Mýrdalsjökull ice cap, Iceland. *Sedimentary Geology 172*, 139–163. https://doi.org/10.1016/j.sedgeo.2004.08.002.

Klimke, J., Wiederhold, H., Winsemann, J., Ertl, G. & Elbracht, J. 2013: Three-dimensional mapping of Quaternary sediments improved by airborne electromagnetics in the case of the Quakenbrück Basin, Northern Germany. *Zeitschrift der Deutschen Gesellschaft für Geowissenschaften 164*, 369–384. https://doi.org/10.1127/1860-1804/2013/0023.

Klostermann, J. 1986: *Geologische Karte von Nordrhein-Westfalen 1: 25000. Erläuterungen zu Blatt 4404 Issum*. 120 pp. Geologisches Landesamt Nordrhein-Westfalen, Krefeld.

Klostermann, J. 1990: Saalezeitliche Stauchmoränentypen am Niederrhein und ihre Entstehung. *Neues Jahrbuch für Geologie und Paläontologie-Abhandlungen 181*, 455–470. https://doi.org/10.1127/njgpa/181/1990/455.

Klostermann, J. 1992: *Das Quartär der Niederrheinischen Bucht – Ablagerungen der letzten Eiszeit am Niederrhein*. 200 pp. Geologisches Landesamt Nordrhein-Westfalen, Krefeld.

Kluiving, S. J., Rappol, M. & van der Wateren, D. 1991: Till stratigraphy and ice movements in eastern Overijssel, the Netherlands. *Boreas 20*, 193–205. https://doi.org/10.1111/j.1502-3885.1991.tb00150.x.

Krauß, N., Börner, A. & Kenzler, M. 2025: Geochronological investigations at the maximum extent of the Fennoscandian ice sheet during the Late Weichselian glaciation in northern Germany. *Boreas 54*, 246–257. https://doi.org/10.1111/bor.12695.

Krbetschek, M. R., Degering, D. & Alexowsky, W. 2008: Infrarot-Radiofluoreszenz-Alter (IR-RF) unter-saalezeitlicher Sedimente Mittel- und Ostdeutschlands (infrared radiofluorescence ages (IR-RF) of Lower Saalian sediments from Central and Eastern Germany). *Zeitschrift der Deutschen Gesellschaft für Geowissenschaften 159*, 133–140. https://doi.org/10.1127/1860-1804/2008/0159-0133.

Kreutzer, S., Lauer, T., Meszner, S., Krbetschek, M., Faust, D. & Fuchs, M. 2014: Chronology of the Quaternary profile Zeuchfeld in Saxony-Anhalt/Germany – a preliminary luminescence dating study. *Zeitschrift für Geomorphologie, Supplementary Issues 58*, 5–26. https://doi.org/10.1127/0372-8854/2012/S-00112.

Kronborg, C., Nielsen, O. B., Beyer, C. & Thomsen, E. 2025: Early Pleistocene interglacial-glacial deposits in Denmark linked to the Matuyama Chron and MIS 22–21. *Quaternary Science Reviews 366*, 109502. https://doi.org/10.1016/j.quascirev.2025.109502.

Krüger, J. & Kjær, K. H. 1999: A data chart for field description and genetic interpretation of glacial diamicts and associated sediments with examples from Greenland, Iceland, and Denmark. *Boreas 28*, 386–402. https://doi.org/10.1111/j.1502-3885.1999.tb00228.x.

Krzyszkowski, D. & Zieliński, T. 2002: The Pleistocene end moraine fans: controls on their sedimentation and location. *Sedimentary Geology 149*, 73–92. https://doi.org/10.1016/S0037-0738(01)00245-7.

Kuster, H. & Meyer, K.-D. 1995: *Karte der Lage der Quartärbasis in Niedersachsen und Bremen, 1:500 000*. Landesamt für Bergbau, Energie und Geologie, Hannover.

Laban, C. & van der Meer, J. J. 2011: Pleistocene glaciation in the Netherlands. *In* Ehlers, J., Gibbard, P. L. & Hughes, P. D. (eds.): *Quaternary Glaciations – Extent and Chronology – A Closer Look*, 247–260. *Developments in Quaternary Sciences 15*. Elsevier, Amsterdam. https://doi.org/10.1016/B978-0-444-53447-7.00020-9.

Landesamt für Bergbau, Energie und Geologie (LBEG) 2013: *Geologisches 3D-Modell des tieferen Untergrundes von Niedersachsen (GTA3D)*. LBEG, Hannover.

Lang, H. D. 1964: Über glaziäre Stauchungen in den Mellendorfer und Brelinger Bergen nördlich von Hannover. *Eiszeitalter und Gegenwart 15*, 207–220. https://doi.org/10.3285/eg.15.1.16.

Lang, J. & Winsemann, J. 2013: Lateral and vertical facies relationships of bedforms deposited by aggrading supercritical flows: from cyclic steps to humpback dunes. *Sedimentary Geology 296*, 36–54. https://doi.org/10.1016/j.sedgeo.2013.08.005.

Lang, J., Alho, P., Kasvi, E., Goseberg, N. & Winsemann, J. 2019: Impact of Middle Pleistocene (Saalian) glacial lake-outburst floods on the meltwater-drainage pathways in northern central Europe: insights from 2D numerical flood simulation. *Quaternary Science Reviews 209*, 82–99. https://doi.org/10.1016/j.quascirev.2019.02.018.

Lang, J., Fedele, J. J. & Hoyal, D. C. J. D. 2021a: Three-dimensional submerged wall jets and their transition to density flows: morphodynamics and implications for the depositional record. *Sedimentology 68*, 1297–1327. https://doi.org/10.1111/sed.12860.

Lang, J., Lauer, T. & Winsemann, J. 2018: New age constraints for the Saalian glaciation in northern central Europe: implications for the extent of ice sheets and related proglacial lake systems. *Quaternary Science Reviews 180*, 240–259. https://doi.org/10.1016/j.quascirev.2017.11.029.

Lang, J., Le Heron, D. P., van den Berg, J. H. & Winsemann, J. 2021b: Bedforms and sedimentary structures related to supercritical flows in

glacigenic settings. *Sedimentology 68*, 1539–1579. https://doi.org/10.1111/sed.12776.

Lang, J., Sievers, J., Loewer, M., Igel, J. & Winsemann, J. 2017: 3D architecture of cyclic step and antidune deposits in glacigenic subaqueous fan and delta settings: integrating outcrop and ground-penetrating radar data. *Sedimentary Geology 362*, 83–100. https://doi.org/10.1016/j.sedgeo.2017.10.011.

Lang, J., Winsemann, J., Steinmetz, D., Polom, U., Pollok, L., Böhner, U., Serangeli, J., Brandes, C., Hampel, A. & Winghart, S. 2012: The Pleistocene of Schöningen, Germany: a complex tunnel valley fill revealed from 3D subsurface modelling and shear wave seismics. *Quaternary Science Reviews 39*, 86–105. https://doi.org/10.1016/j.quascirev.2012.02.009.

Lauer, T. & Weiss, M. 2018: Timing of the Saalian- and Elsterian glacial cycles and the implications for Middle–Pleistocene hominin presence in central Europe. *Scientific Reports 8*, 5111. https://doi.org/10.1038/s41598-018-23541-w.

Leclair, S. F. & Arnott, R. W. C. 2005: Parallel lamination formed by high-density turbidity currents. *Journal of Sedimentary Research 75*, 1–5. https://doi.org/10.2110/jsr.2005.001.

Lee, J. R., Busschers, F. S. & Sejrup, H. P. 2012: Pre-Weichselian Quaternary glaciations of the British Isles, the Netherlands, Norway and adjacent marine areas south of 68°N: implications for long-term ice sheet development in northern Europe. *Quaternary Science Reviews 44*, 213–238. https://doi.org/10.1016/j.quascirev.2010.02.027.

Lee, J. R., Phillips, E., Booth, S. J., Rose, J., Jordan, H. M., Pawley, S. M., Warren, M. & Lawley, R. S. 2013: A polyphase glacitectonic model for ice-marginal retreat and terminal moraine development: the Middle Pleistocene British Ice Sheet, northern Norfolk, UK. *Proceedings of the Geologists' Association 124*, 753–777. https://doi.org/10.1016/j.pgeola.2013.07.002.

Lehmkuhl, F., Zens, J., Krauß, L., Schulte, P. & Kels, H. 2016: Loess-paleosol sequences at the northern European loess belt in Germany: distribution, geomorphology and stratigraphy. *Quaternary Science Reviews 153*, 11–30. https://doi.org/10.1016/j.quascirev.2016.10.008.

Li, B. & Li, S.-H. 2011: Luminescence dating of K-feldspar from sediments: a protocol without anomalous fading correction. *Quaternary Geochronology 6*, 468–479. https://doi.org/10.1016/j.quageo.2011.05.00.

Li, B., Jacobs, Z. & Roberts, R. G. 2016: Investigation of the applicability of standardized growth curves for OSL dating of quartz from Haua Fteah cave, Libya. *Quaternary Geochronology 35*, 1–15. https://doi.org/10.1016/j.quageo.2016.05.001.

Li, B., Jacobs, Z. & Roberts, R. G. 2020: Validation of the LnTn method for De determination in optical dating of K-feldspar and quartz. *Quaternary Geochronology 58*, 101066. https://doi.org/10.1016/j.quageo.2020.101066.

Li, B., Jacobs, Z., Roberts, R. G., Galbraith, R. & Peng, J. 2017: Variability in quartz OSL signals caused by measurement uncertainties: problems and solutions. *Quaternary Geochronology 41*, 11–25. https://doi.org/10.1016/j.quageo.2017.05.006.

Liritzis, I., Stamoulis, K., Papachristodoulou, C. & Ioannides, K. 2013: A re-evaluation of radiation dose-rate conversion factors. *Mediterranian Archaeology and Archaeometry 13*, 1–15.

Litt, T., Behre, K.-E., Meyer, K.-D., Stephan, H.-J. & Wansa, S. 2007: Stratigraphische Begriffe für das Quartär des norddeutschen Vereisungsgebietes. *E&G Quaternary Science Journal 56*, 7–65. https://doi.org/10.3285/eg.56.1-2.02.

Lohrberg, A., Schwarzer, K., Unverricht, D., Omlin, A. & Krastel, S. 2020: Architecture of tunnel valleys in the southeastern North Sea: new insights from high-resolution seismic imaging. *Journal of Quaternary Science 35*, 892–906. https://doi.org/10.1002/jqs.3244.

Long, H., Zhang, J., Huang, X., Zhang, A., Yang, N., He, M. & Yang, L. 2024: Single-grain K-feldspar luminescence dating of the late Quaternary rapid decline in the largest Lake over the Tibetan Plateau. *Quaternary Geochronology 81*, 101503. https://doi.org/10.1016/j.quageo.2024.101503.

Lowe, D. G. & Arnott, R. W. C. 2016: Composition and architecture of braided and sheetflood-dominated ephemeral fluvial strata in the Cambrian–Ordovician Potsdam Group: a case example of the morphodynamics of Early Phanerozoic fluvial systems and climate change. *Journal of Sedimentary Research 86*, 587–612. https://doi.org/10.2110/jsr.2016.39.

Lüthgens, C., Böse, M. & Krbetschek, M. 2010: On the age of the young morainic morphology in the area ascribed to the maximum extent of the Weichselian glaciation in north-eastern Germany. *Quaternary International 222*, 72–79. https://doi.org/10.1016/j.quaint.2009.06.028.

Lüttig, G. 1954: Alt- und mittelpleistozäne Eisrandlagen zwischen Harz und Weser. *Geologisches Jahrbuch 70*, 43–125.

Lüttig, G. 1960: Neue Ergebnisse quartärgeologischer Forschung im Raume Alfeld – Hameln – Elze. *Geologisches Jahrbuch 77*, 337–390.

Lutz, R., Kalka, S., Gaedicke, C., Reinhardt, L. & Winsemann, J. 2009: Pleistocene tunnel valleys in the German North Sea: spatial distribution and morphology. *Zeitschrift der Deutschen Gesellschaft für Geowissenschaften 160*, 225–235. https://doi.org/10.1127/1860-1804/2009/0160-0225.

MacDonald, R. G., Alexander, J., Bacon, J. C. & Cooker, M. J. 2009: Flow patterns, sedimentation and deposit architecture under a hydraulic jump on a non-eroding bed: defining hydraulic-jump unit bars. *Sedimentology 56*, 1346–1367. https://doi.org/10.1111/j.1365-3091.2008.01037.x.

Margari, V., Skinner, L. C., Hodell, D. A., Martrat, B., Toucanne, S., Grimalt, J. O., Gibbard, P. L., Lunkka, J. P. & Tzedakis, P. C. 2014: Land-ocean changes on orbital and millennial time scales and the penultimate glaciation. *Geology 42*, 183–186. https://doi.org/10.1130/G35070.1.

Margold, M., Stokes, C. R. & Clark, C. D. 2015: Ice streams in the Laurentide Ice Sheet: identification, characteristics and comparison to modern ice sheets. *Earth-Science Reviews 143*, 117–146. https://doi.org/10.1016/j.earscirev.2015.01.011.

Marks, L., Bińka, K., Woronko, B., Majecka, A. & Teodorski, A. 2019: Revision of the late Middle Pleistocene stratigraphy and palaeoclimate in Poland. *Quaternary International 534*, 5–17. https://doi.org/10.1016/j.quaint.2019.02.023.

Meinsen, J., Winsemann, J., Roskosch, J., Brandes, C., Frechen, M., Dultz, S. & Böttcher, J. 2014: Climate control on the evolution of Late Pleistocene alluvial-fan and aeolian sand-sheet systems in NW-Germany. *Boreas 43*, 42–66. https://doi.org/10.1111/bor.12021.

Meinsen, J., Winsemann, J., Weitkamp, A., Landmeyer, N., Lenz, A. & Dölling, M. 2011: Middle Pleistocene (Saalian) lake outburst floods in the Münsterland Embayment (NW Germany): impacts and magnitudes. *Quaternary Science Reviews 30*, 2597–2625. https://doi.org/10.1016/j.quascirev.2011.05.014.

Merkt, J. 1975: *Geologische Karte von Niedersachsen 1:25000, Blatt 3033 Woltersdorf*. Landesamt für Bergbau, Energie und Geologie, Hannover.

Meyer, K.-D. 1982: *Geologische Karte von Niedersachsen 1:25000. Erläuterungen zu Blatt Nr. 2524 Buxtehude*. 120 pp. Niedersächsisches Landesamt für Bodenforschung, Hannover.

Meyer, H.-H. 1987a: Die Stauchendmoränen der Rehburger Eisrandlage und ihre Entstehung. *Osnabrücker naturwissenschaftliche Mitteilungen 13*, 23–42.

Meyer, K.-D. 1987b: Ground and end moraines in Lower Saxony. *In* van der Meer, J. J. M. (ed.): *Tills and Glaciotectonics*, 197–204. Balkema, Rotterdam.

Meyer, K.-D. 1993: *Geologische Karte von Niedersachsen 1:25000. Erläuterungen zu Blatt Nr. 2827 Amelinghausen*. 119 pp. Niedersächsisches Landesamt für Bodenforschung, Hannover.

Meyer, K.-D. 2005: Zur Stratigraphie des Saale-Glazials in Niedersachsen und zu Korrelationsversuchen mit Nachbargebieten. *Eiszeitalter und Gegenwart 55*, 25–42. https://doi.org/10.3285/eg.55.1.02.

Meyer, K.-D. 2009: *Geologische Karte von Niedersachsen 1:25000. Erläuterungen zu Blatt Nr. 2830 Dahlenburg*. 33 pp. Landesamt für Bergbau, Energie und Geologie, Hannover.

Meyer, K.-D. & Schneekloth, H. 1973: *Geologische Karte von Niedersachsen 1:25000. Erläuterungen zu Blatt Neuenwalde Nr. 2318*. 80 pp. Niedersächsisches Landesamt für Bodenforschung, Hannover.

Miall, A. D. 1985: Architectural-element analysis: a new method of facies analysis applied to fluvial deposits. *Earth-Science Reviews 22*, 261–308. https://doi.org/10.1016/0012-8252(85)90001-7.

Mleczak, M., Woronko, B., Pisarska-Jamroży, M. & Bujak, Ł. 2021: Permafrost as the main factor controlling the fluvial sedimentation style on glaciomarginal fans. *Sedimentary Geology 422*, 105971. https://doi.org/10.1016/j.sedgeo.2021.105971.

Molodkov, A., Bitinas, A. & Damušytė, A. 2010: IR-OSL studies of till and inter-till deposits from the Lithuanian maritime region. *Quaternary Geochronology 5*, 263–268. https://doi.org/10.1016/j.quageo.2009.04.004.

Moscariello, A. 2018: Alluvial fans and fluvial fans at the margins of continental sedimentary basins: geomorphic and sedimentological distinction for geo-energy exploration and development. *In* Ventra, D. & Clarke, L. E. (eds.): *Geology and Geomorphology of Alluvial and Fluvial Fans: Terrestrial and Planetary Perspectives*, 215–243. *Geological Society, London, Special Publications 440*. https://doi.org/10.1144/SP440.11.

Müller, K. 2021: *Palaeoseismological Analyses of Northern and Central Germany*. Ph.D. thesis, Leibniz Universität Hannover, 212 pp. https://doi.org/10.15488/11972.

Nitychoruk, J., Zbucki, Ł., Rychel, J., Woronko, B. & Marks, L. 2018: Extent and dynamics of the Saalian ice-sheet margin in Neple, eastern Poland. *Bulletin of the Geological Society of Finland 90*, 185–198. https://doi.org/10.17741/bgsf/90.2.004.

Ono, K., Plink-Björklund, P., Eggenhuisen, J. T. & Cartigny, M. J. B. 2021: Froude supercritical flow processes and sedimentary structures: new insights from experiments with a wide range of grain sizes. *Sedimentology 68*, 1328–1357. https://doi.org/10.1111/sed.12682.

Passchier, S., Laban, C., Mesdag, C. S. & Rijsdijk, K. F. 2010: Subglacial bed conditions during Late Pleistocene glaciations and their impact on ice dynamics in the southern North Sea. *Boreas 39*, 633–647. https://doi.org/10.1111/j.1502-3885.2009.00138.x.

Pawley, S. M., Bailey, R. M., Rose, J., Moorlock, B. S. P., Hamblin, R. J. O., Booth, S. J. & Lee, J. R. 2008: Age limits on Middle Pleistocene glacial sediments from OSL dating, north Norfolk, UK. *Quaternary Science Reviews 27*, 1363–1377. https://doi.org/10.1016/j.quascirev.2008.02.013.

Peng, J. & Li, B. 2017: Single-aliquot regenerative-dose (SAR) and standardised growth curve (SGC) equivalent dose determination in a Batch model using the R package 'numOSL'. *Ancient TL 35*, 32–53. https://doi.org/10.26034/la.atl.2017.516.

Peng, B., Jin, Z., Wang, J., Chang, T., Zhu, X. & Gul, B. 2017: The significance and timing of sheetflood vs braided channel deposition on lacustrine fan deltas, Junggar Basin, NW China. *Australian Journal of Earth Sciences 64*, 919–930. https://doi.org/10.1080/08120099.2017.1379436.

Pisarska-Jamroży, M. 2008: Zonation of glaciomarginal environment inferred from Pleistocene deposits of Mysliborz Lakeland, NW Poland. *Geografiska Annaler 90A*, 237–249. https://doi.org/10.1111/j.1468-0459.2008.342.x.

Pisarska-Jamroży, M. & Zieliński, T. 2014: Pleistocene sandur rhythms, cycles and megacycles: interpretation of depositional scenarios and palaeoenvironmental conditions. *Boreas 43*, 330–348. https://doi.org/10.1111/bor.12041.

von Poblozki, B. 1973: *Lithofazieskarten Quartär, Blatt 1963 Klötze*. Zentrales Geologisches Institut, Berlin.

von Poblozki, B. 1981: *Lithofazieskarten Quartär, Blatt 1863 Salzwedel*. Zentrales Geologisches Institut, Berlin.

von Poblozki, B. 1995: Quaternary geology of the Altmark region. *In* Ehlers, J., Kozarski, S. & Gibbard, P. L. (eds.): *Glacial Deposits in North-East Europe*, 473–484. Balkema, Rotterdam.

von Poblozki, B. 2002: Stratigraphie des Quartärs und quartäre Bewegungen an Salzstrukturen in der nördlichen Altmark. *Hallesches Jahrbuch für Geowissenschaften 24*, 57–82.

Pohl, F., Eggenhuisen, J. T., De Leeuw, J., Cartigny, M. J. B., Brooks, H. L. & Spychala, Y. T. 2023: Reconstructing sedimentary processes in a Permian channel–lobe transition zone: an outcrop study in the Karoo Basin, South Africa. *Geological Magazine 160*, 107–126. https://doi.org/10.1017/S0016756822000693.

Pohl, F., Eggenhuisen, J. T., Tilston, M. & Cartigny, M. J. B. 2019: New flow relaxation mechanism explains scour fields at the end of submarine channels. *Nature Communications 10*, 4425. https://doi.org/10.1038/s41467-019-12389-x.

Prescott, J. R. & Hutton, J. T. 1994: Cosmic ray contribution to dose rates for luminescence and ESR dating: large depths and long-term time variations. *Radiation Measurements 23*, 497–500. https://doi.org/10.1016/1350-4487(94)90086-8.

Rahimzadeh, N., Hein, H., Urban, B., Weiss, M., Tanner, D. C., Khosravichenar, A., Tsukamoto, S. & Lauer, T. 2024: Dating the Neanderthal environment: detailed luminescence chronology of a palaeochannel sediment core at the Palaeolithic site of Lichtenberg in the Lower Saxony, northern Germany. *Geochronology 83*, 101564. https://doi.org/10.1016/j.quageo.2024.101564.

Rahimzadeh, N., von Soest, N., Tsukamoto, S. & Winsemann, J. 2026: Luminescence dating of glacigenic deposits from northern Germany: a comparison of multigrain aliquots and single grains K-feldspar methods. *Quaternary Geochronology 91*, 101711. https://doi.org/10.1016/j.quageo.2025.101711.

Railsback, L. B., Gibbard, P. L., Head, M. J., Voarintsoa, N. R. G. & Toucanne, S. 2015: An optimized scheme of lettered marine isotope substages for the last 1.0 million years, and the climatostratigraphic nature of isotope stages and substages. *Quaternary Science Reviews 111*, 94–106. https://doi.org/10.1016/j.quascirev.2015.01.012.

Rappol, M. 1984: Till in Southeast Drenthe and the origin of the Hondsrug Complex, the Netherlands. *E&G Quaternary Science Journal 34*, 7–28. https://doi.org/10.3285/eg.34.1.02.

Rattas, M., Kalm, V., Kihno, K., Liivrand, E., Tinn, O., Tänavsuu-Milkeviciene, K. & Sakson, M. 2010: Chronology of Late Saalian and Middle Weichselian episodes of ice-free lacustrine sedimentation recorded in the Arumetsa section, southwestern Estonia. *Estonian Journal of Earth Sciences 59*, 125–140. https://doi.org/10.3176/earth.2010.2.03.

Reimann, T., Thomsen, K. J., Jain, M., Murray, A. S. & Frechen, M. 2012: Single-grain dating of young sediments using the pIRIR signal from feldspar. *Quaternary Geochronology 11*, 28–41. https://doi.org/10.1016/j.quageo.2012.04.016.

Richter, K. 1956: Geschiebegrenzen und Eisrandlagen in Niedersachsen. *Geologisches Jahrbuch 76*, 223–234.

Roskosch, J., Winsemann, J., Polom, U., Brandes, C., Tsukamoto, S., Weitkamp, A., Bartholomäus, W. A., Henningsen, D. & Frechen, M. 2015: Luminescence dating of ice-marginal deposits in northern Germany: evidence for repeated glaciations during the Middle Pleistocene (MIS 12 to MIS 6). *Boreas 44*, 103–126. https://doi.org/10.1111/bor.12083.

Schmidt, C., Bösken, J. & Kolb, T. 2018: Is there a common alpha-efficiency in polymineral samples measured by various infrared stimulated luminescence protocols? *Geochronometria 45*, 160–172. https://doi.org/10.1515/geochr-2015-0095.

Schneekloth, H. & Sickenberg, O. 1968: Probleme der Interglazial-Forschung in Niedersachsen. *Zeitschrift der Deutschen Geologischen Gesellschaft 117*, 368–369.

Sindowski, K.-H. 1965: Die drenthestadiale Altenwalder Stauchmoräne südlich Cuxhaven. *Zeitschrift der Deutschen Geologischen Gesellschaft 1*, 158–162.

Sindowski, K.-H. 1969a: *Geologische Karte von Niedersachsen 1:25000. Erläuterungen zu Blatt Altenwalde Nr.2117*. 63 pp. Niedersächsisches Landesamt für Bodenforschung, Hannover.

Sindowski, K.-H. 1969b: *Geologische Karte von Niedersachsen 1:25000. Erläuterungen zu Blatt Cuxhaven Nr.2118*. 52 pp. Niedersächsisches Landesamt für Bodenforschung, Hannover.

Skupin, K. & Zandstra, J. G. 2010: *Gletscher der Saale-Kaltzeit am Niederrhein. Untersuchungen zur Petrographie und Leitgeschiebeführung der Stauchmoränen des Niederrheins und deren Anbindung an die Moränen des Münsterlandes*. 117 pp. Geologischer Dienst Nordrhein-Westfalen, Krefeld.

Slootman, A., Vellinga, A. J., Moscariello, A. & Cartigny, M. J. B. 2021: The depositional signature of high-aggradation chute-and-pool bedforms: the build-and-fill structure. *Sedimentology 68*, 1640–1673. https://doi.org/10.1111/sed.12843.

Sobczyk, A., Borówka, R. K., Badura, J., Stachowicz-Rybka, R., Tomkowiak, J., Hrynowiecka, A., Sławińska, J., Tomczak, M., Pitura, M., Lamentowicz, M., Kołaczek, P., Karpińska-Kołaczek, M., Tarnawski, D., Kadej, M., Moska, P., Krąpiec, M., Stachowicz, K., Bieniek, B., Siedlik, K., Bąk, M., van der Made, J., Kotowski, A. & Stefaniak, K. 2020: Geology, stratigraphy and palaeoenvironmental evolution of the *Stephanorhinus kirchbergensis*-bearing Quaternary palaeolake(s) of Gorzów Wielkopolski (NW Poland, Central

Europe). *Journal of Quaternary Science 35*, 539–558. https://doi.org/10.1002/jqs.3198.
Spychala, Y. T., Poyatos-Moré, M., Blumenberg, M., Scheeder, G. & Winsemann, J. 2025: Enrichment of organic carbon in a deep-water sand-prone turbidite system: a study from the Eocene Aínsa Basin (Spanish Pyrenees). *Sedimentology 72*, 2301–2322. https://doi.org/10.1111/sed.70041.
Stackebrandt, W. 2009: Subglacial channels of Northern Germany – a brief review. *Zeitschrift der Deutschen Gesellschaft für Geowissenschaften 160*, 203–210. https://doi.org/10.1127/1860-1804/2009/0160-0203.
Steinmetz, D., Winsemann, J., Brandes, C., Siemon, B., Ullmann, A., Wiederhold, H. & Meyer, U. 2015: Towards an improved geological interpretation of airborne electromagnetic data: a case study from the Cuxhaven tunnel valley and its Neogene host sediments (northwest Germany). *Netherlands Journal of Geosciences 94*, 201–227. https://doi.org/10.1017/njg.2014.39.
Stephan, H.-J. 2014: Climato-stratigraphic subdivision of the Pleistocene in Schleswig-Holstein, Germany and adjoining areas. *E&G Quaternary Science Journal 63*, 3–18. https://doi.org/10.3285/eg.63.1.01.
Stokes, C. R. 2018: Geomorphology under ice streams: moving from form to process. *Earth Surface Processes and Landforms 43*, 85–123. https://doi.org/10.1002/esp.4259.
Tan, C. & Plink-Björklund, P. 2021: Morphodynamics of supercritical flow in a linked river and delta system, Daihai Lake, Northern China. *Sedimentology 68*, 1606–1639. https://doi.org/10.1111/sed.12839.
Terpiłowski, S., Zieliński, T., Mroczek, P., Zieliński, P., Czubla, P. & Fedorowicz, S. 2021: New evidence for the rank of the Wartanian cold period (Pleistocene, MIS 6): a case study from E Poland. *Annales. Societatis Geologorum Poloniae 91*, 327–345. https://doi.org/10.14241/asgp.2021.20.
Thiel, C., Buylaert, J. P., Murray, A., Terhorst, B., Hofer, I., Tsukamoto, S. & Frechen, M. 2011: Luminescence dating of the Stratzing loess profile (Austria) – testing the potential of an elevated temperature post-IR IRSL protocol. *Quaternary International 234*, 23–31. https://doi.org/10.1016/j.quaint.2010.05.018.
Thrasher, I. M., Mauz, B., Chiverrell, R. C., Lang, A. & Thomas, G. S. P. 2009: Testing an approach to OSL dating of Late Devensian glaciofluvial sediments of the British Isles. *Journal of Quaternary Science 24*, 785–801. https://doi.org/10.1002/jqs.1253.
Toucanne, S., Zaragosi, S., Bourillet, J. F., Cremer, M., Eynaud, F., Van Vliet-Lanoë, B., Penaud, A., Fontanier, C., Turon, J. L., Cortijo, E. & Gibbard, P. L. 2009a: Timing of massive 'Fleuve Manche' discharges over the last 350 kyr: insights into the European ice-sheet oscillations and the European drainage network from MIS 10 to 2. *Quaternary Science Reviews 28*, 1238–1256. https://doi.org/10.1016/j.quascirev.2009.01.006.
Toucanne, S., Zaragosi, S., Bourillet, J. F., Gibbard, P. L., Eynaud, F., Giraudeau, J., Turon, T. L., Cremer, M., Cortijo, E., Martinez, P. & Rossignol, L. 2009b: A 1.2 Ma record of glaciation and fluvial discharge for the west European Atlantic margin. *Quaternary Science Reviews 28*, 2974–2981. https://doi.org/10.1016/j.quascirev.2009.08.003.
Tsukamoto, S., Kondo, R., Lauer, T. & Jain, M. 2017: Pulsed IRSL: a stable and fast bleaching luminescence signal from feldspar for dating Quaternary sediments. *Quaternary Geochronology 41*, 26–36. https://doi.org/10.1016/j.quageo.2017.05.004.
Tylmann, K., Wysota, W., Rinterknecht, V., Moska, P., Bielicka-Giełdoń, A. & ASTER Team 2024: Millennial-scale fluctuations of palaeo-ice margin at the southern fringe of the last Fennoscandian Ice Sheet. *The Cryosphere 18*, 1889–1909. https://doi.org/10.5194/tc-18-1889-2024.
Vaughan-Hirsch, D. P. & Phillips, E. R. 2017: Mid-Pleistocene thin-skinned glaciotectonic thrusting of the Aberdeen Ground Formation, Central Graben region, central North Sea. *Journal of Quaternary Science 32*, 196–212. https://doi.org/10.1002/jqs.2836.
Voss, H.-H. 1979: *Geologische Karte von Niedersachsen 1:25000. Erläuterungen zu Blatt Nr. 3522 Wunstorf*. 102 pp. Niedersächsisches Landesamt für Bodenforschung, Hannover.
Voss, H.-H. 1982: *Geologische Karte von Niedersachsen 1:25000. Erläuterungen zu Blatt Nr.3421 Husum*. 130 pp. Niedersächsisches Landesamt für Bodenforschung, Hannover.
Voss, H.-H. 1991: *Geologische Karte von Niedersachsen 1:25000. Erläuterungen zu Blatt Nr. 3321 Nienburg*. 104 pp. Niedersächsisches Landesamt für Bodenforschung, Hannover.
Waas, D., Kleinmann, A. & Lepper, J. 2011: Uranium-series dating of fen peat horizons from pit Nachtigall in northern Germany. *Quaternary International 241*, 111–124. https://doi.org/10.1016/j.quaint.2010.09.010.
Wainer, K., Genty, D., Blamart, D., Bar-Matthews, M., Quinif, Y. & Plagnes, V. 2013: Millennial climatic instability during penultimate glacial period recorded in a south-western France speleothem. *Palaeogeography, Palaeoclimatology, Palaeoecology 376*, 122–131. https://doi.org/10.1016/j.palaeo.2013.02.026.
van der Wateren, D. 1987: Structural geology and sedimentology of the Dammer Berge push moraine, Frg. *In* van der Meer, J. J. M. (ed.): *Tills and Glaciotectonics*, 157–182. Balkema, Rotterdam.
van der Wateren, F. M. 1994: Proglacial subaquatic outwash fan and delta sediments in push moraines – indicators of subglacial meltwater activity. *Sedimentary Geology 91*, 145–172. https://doi.org/10.1016/0037-0738(94)90127-9.
Weckwerth, P., Kalińska, E., Wysota, W., Krawiec, A., Alexanderson, H. & Chabowski, M. 2024: Evolutionary model for glacial lake-outburst fans at the ice-sheet front: development of meltwater outlets and origins of bedforms. *Geomorphology 453*, 109125. https://doi.org/10.1016/j.geomorph.2024.109125.
Weckwerth, P., Przegiętka, K. R., Chruścińska, A. & Pisarska-Jamroży, M. 2013: The relation between optical bleaching and sedimentological features of fluvial deposits in the Toruń basin (Poland). *Geological Quarterly 57*, 31–44. https://doi.org/10.7306/gq.1074.
Weissmann, G. S., Hartley, A. J., Nichols, G. J., Scuderi, L. A., Olson, M., Buehler, H. & Banteah, R. 2010: Fluvial form in modern continental sedimentary basins: distributive fluvial systems. *Geology 38*, 39–42. https://doi.org/10.1130/G30242.1.
Winsemann, J. & Lang, J. 2020: Flooding northern Germany: impacts and magnitudes of middle Pleistocene glacial lake-outburst floods. *In* Herget, J. & Fontana, A. (eds.): *Palaeohydrology. Geography of the Physical Environment*, 29–47. Springer, Cham. https://doi.org/10.1007/978-3-030-23315-0_2.
Winsemann, J., Alho, P., Laamanen, L., Goseberg, N., Lang, J. & Klostermann, J. 2016: Flow dynamics, sedimentation and erosion of glacial lake outburst floods along the Middle Pleistocene Scandinavian Ice Sheet (northern Central Europe). *Boreas 45*, 260–283. https://doi.org/10.1111/bor.12146.
Winsemann, J., Asprion, U. & Meyer, T. 2004: Sequence analysis of early Saalian glacial lake deposits (NW Germany): evidence of rapid ice margin retreat and associated calving processes. *Sedimentary Geology 165*, 223–251. https://doi.org/10.1016/j.sedgeo.2003.11.010.
Winsemann, J., Asprion, U., Meyer, T., Schultz, H. & Victor, P. 2003: Evidence of iceberg- ploughing in a subaqueous ice-contact fan, glacial Lake Rinteln, NW Germany. *Boreas 32*, 386–398. https://doi.org/10.1111/j.1502-3885.2003.tb01092.x.
Winsemann, J., Brandes, C. & Polom, U. 2011: Response of a proglacial delta to rapid high-amplitude lake level change: an integration of outcrop data and high-resolution shear wave seismics. *Basin Research 23*, 22–52. https://doi.org/10.1111/j.1365-2117.2010.00465.x.
Winsemann, J., Hartmann, T., Fälber, R. & Lauer, T. 2022: Depositional architecture and aggradation rates of sand-rich, supercritical alluvial fans: control by autogenic processes or high-frequency climatic oscillations? *Sedimentary Geology 440*, 106238. https://doi.org/10.1016/j.sedgeo.2022.106238.
Winsemann, J., Hornung, J. J., Meinsen, J., Asprion, U., Polom, U., Brandes, C., Bußmann, M. & Weber, C. 2009: Anatomy of a subaqueous ice-contact fan and delta complex, Middle Pleistocene, NW Germany. *Sedimentology 36*, 1041–1076. https://doi.org/10.1111/j.1365-3091.2008.01018.x.
Winsemann, J., Koopmann, H., Tanner, D. C., Lutz, R., Lang, J., Brandes, C. & Gaedicke, C. 2020: Seismic interpretation and structural restoration of the Heligoland glaciotectonic thrust-fault complex: implications for multiple deformation during (pre-)Elsterian to Warthian ice advances into the southern North Sea Basin. *Quaternary Science Reviews 227*, 106068. https://doi.org/10.1016/j.quascirev.2019.106068.

Winsemann, J., Lang, J., Fedele, J. J., Zavala, C. & Hoyal, D. C. J. D. 2021: Re-examining models of shallow-water deltas: insights from tank experiments and field examples. *Sedimentary Geology 421*, 105962. https://doi.org/10.1016/j.sedgeo.2021.105962.

Winsemann, J., Lang, J., Polom, U., Loewer, M., Igel, J., Pollok, L. & Brandes, C. 2018: Ice-marginal forced regressive deltas in glacial lake basins: geomorphology, facies variability and large-scale depositional architecture. *Boreas 47*, 973–1002. https://doi.org/10.1111/bor.12317.

Winsemann, J., Lang, J., Roskosch, J., Polom, U., Böhner, U., Brandes, C., Glotzbach, C. & Frechen, M. 2015: Terrace styles and timing of terrace formation in the Weser and Leine valleys, northern Germany: response of a fluvial system to climate change and glaciation. *Quaternary Science Reviews 123*, 31–57. https://doi.org/10.1016/j.quascirev.2015.06.005.

Wiśniewski, A., Bobak, D., Połtowicz-Bobak, M. & Moska, P. 2024: Late Middle Palaeolithic and Early Upper Palaeolithic in Poland in the light of new numerical dating. *Geographia Polonica 97*, 295–325. https://doi.org/10.7163/GPol.0281.

Zieliński, T. & van Loon, A. J. 2000: Subaerial terminoglacial fans III: overview of sedimentary characteristics and depositional model. *Netherlands Journal of Geosciences 79*, 93–107. https://doi.org/10.1017/S0016774600021600.

Zieliński, T. & van Loon, A. J. 2003: Pleistocene sandur deposits represent braidplains, not alluvial fans. *Boreas 32*, 590–611. https://doi.org/10.1111/j.1502-3885.2003.tb01238.x.

Supporting Information

Additional Supporting Information to this article is available at http://www.boreas.dk.

Data S1. Measurements of small aliquots of Saalian and Elsterian ice-marginal deposits and references used in the Supporting Information.

Fig. S1. A and C. Single grain Lx/Tx ratios (before LS-normalization) used to construct the SGC for samples L-EVA 1549 (A) and LUM 5031 (C). B and D. SGC constructed from the Lx/Tx ratios in panels (A and C) after LS-normalization.

Table S1. Overview of sand and gravel pits shown on figures of the main text.

Table S2. Measurement protocols for multi-grain measurements.

Table S3. Summary of equivalent doses and ages from multigrain measurement.

Table S4. Summary of K-feldspar single grains measured, rejected and accepted for D_e estimation, including reasons for rejection.